The Influence of Internal Tyre Pressure on Road Friction

Michael Selig

A thesis submitted to the University of Huddersfield in partial fulfilment of the requirements for the degree Doctor of Philosophy

The University of Huddersfield, UK in collaboration with Frankfurt University of Applied Sciences, Germany

February 2014

Declaration

No portion of the work presented in this thesis has been submitted in support of an application for another degree or qualification of this or any other university or other institute of learning.

Copyright statement

Abstract

Road safety is a very important topic for research and development divisions in the automotive industry. As the tyre is the only link between road surface and vehicle, it plays a very significant role in accident mitigation and prevention.

This thesis investigates the influence of internal tyre pressure on the brake distance both experimentally and theoretically. Brake tests were performed using a robotic system and a winch was used to pull a car with locked wheels. For both experiments, the tyre pressures were changed.

A rubber friction law is presented which can be used for tyre and vehicle dynamics calculations. The friction law was tested by comparing numerical results to the full rubber friction theory of Persson and to experimental data. A two-dimensional (2D) tyre model is introduced that combines the rubber friction law with a simple mass-spring description of the tyre body. The tyre model is very flexible and can be applied to different manoeuvres. It can be used to calculate μ-slip curves, self aligning-torque, braking, and cornering, or combined motion (e.g. braking during cornering). The theoretical predictions have been compared to measured data from indoor tyre testing on sandpaper substrate. Additionally simulations of anti-lock braking system (ABS) using two different control algorithms are presented.

In addition a method for rapidly changing the tyre inflation pressure while a vehicle is in motion is presented. This method can be used for novel safety system approaches.

Dedicated to my dad

Acknowledgements

While researching this thesis, I was supported by many people, institutions and companies. Therefore I would like to express my deep and sincere gratitude to:

- The University of Huddersfield and Frankfurt University of Applied Sciences for giving me the opportunity to undertake this research project and for their financial support.
- My supervision team, Prof. Andrew Ball and Prof. Karsten Schmidt who have constantly guided, helped and supported me over the past few years.
- The Peter Grünberg Institut (PGI-1) of Forschungszentrum Jülich, in form of Dr. Bo Persson and Dr. Boris Lorenz for the great support and help.
- Anthony Best Dynamics, Bradford on Avon, in form of Jeremy Ash, Senior Engineer, for the support and help with the brake robot tests.
- The Instiut für Kraftfahrzeuge (ika) of RWTH University Aachen, in form of Dipl.-Ing. Dirk Henrichmöller for providing experimental tyre data.
- Hankook Tire Co. Ltd., in form of Dr. Yumrak Oh and Nam Seung Kuk for providing brake test data.
- All my colleagues and staff at the institutions where I have worked.
- Last but not least, my family and friends.

Thank you!

List of contents

Wordcount: 39141

Chapter ONE

Chapter one discusses the motivation for this research. It also provides an overview of the history of automotive safety systems and the state-of-the-art technology. Finally, the content and structure of the thesis is outlined and presented along the aims and objectives.

1. Introduction

1.1 Background

The thesis presented here aims to improve road safety in general and investigates options to mitigate the effects of accidents.

A central research and development topic in the automotive industry is the area of active and passive safety of motorcars. The term “active safety” summarizes mechatronic systems which are triggered autonomously to mitigate a hazardous situations. The primary concern of all active safety systems is the avoidance of a possible collision. The electronic stability control (ESC), which has become mandatory for all cars developed since 2011, is a representative example of this category [1]. Passive safety systems, on the other hand, try to reduce the impact of a collision. Seat belt tensioners and side impact bars are some examples of passive safety systems. The circumstances of a particular collision significantly determine the success of all passive safety systems. The vehicle's speed at the moment of impact is an essential criterion that determines the severity of the crash for the people who are involved. For this reason, a number of brake applications have been implemented in the electronic controlled brake systems in order to initiate braking at an early stage and to assist the driver during emergency braking.

The basic goal of the present research project is to increase the frictional force in the contact area between tyre and road surface. An electronic control unit detects a crash situation by monitoring in-vehicle sensor messages. Once a crash situation has been established, the control unit initiates a decrease of the tyre inflation pressure via a wireless interface. The guiding idea is that by increasing the tyre contact pattern, the braking distance of a vehicle and hence the vehicle's speed at a collision can be reduced.

However, initial studies of braking distance using various tyre inflation pressures yielded contradictory results. This called for a detailed study of rubber friction. To understand the phenomena in more detail, Persson's contact mechanics and rubber friction model approach was applied [2].

1.2 State-of-the-art

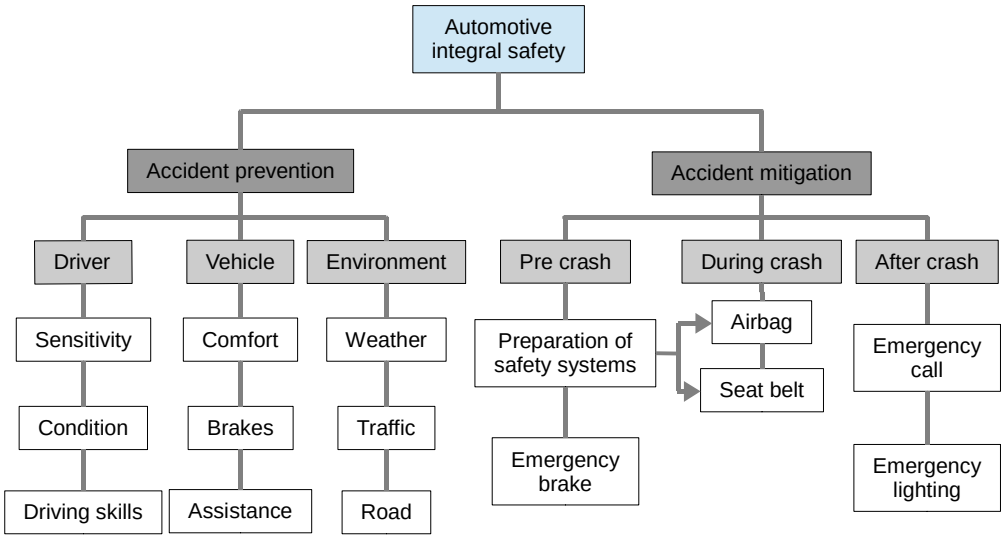

Figure 1.1: Areas of automotive integral safety [3]

Figure 1.1 classifies the automotive safety systems. Wilfert and Seiffert were the first to define automotive safety [4, 5]. Automotive integral safety is an up-to-date term that encompasses accident prevention and accident mitigation. Accident prevention covers all actions and influences needed to prevent an accident. Distinctions are made between the influence of the driver, the vehicle and the environment. Impaired vision, the driver's physical and mental constitution and his or her driving skills are all factors that influences the impact of the driver. The vehicle can be designed to prevent accidents by increasing the driver's comfort. Air-conditioning, comfort seats, or increased visibility as a result of advanced light systems are some examples of such design mechanism. The current weather, traffic and road conditions are all factors that determine the influence of the environment. Furthermore, state-of-the-art brake systems and advanced driver

assistance systems (ADAS) can help prevent accidents.

Accident mitigation reduces the impact of a crash with systems triggered before, during and after an accident. When an accident is inevitable, pre-crash systems are triggered. Some examples of pre-crash systems include the automatic emergency braking and the preparation of systems like the airbags or seat belt tensioners that are activated during the crash. After the crash, the automatic emergency call system and emergency lights can be activated.

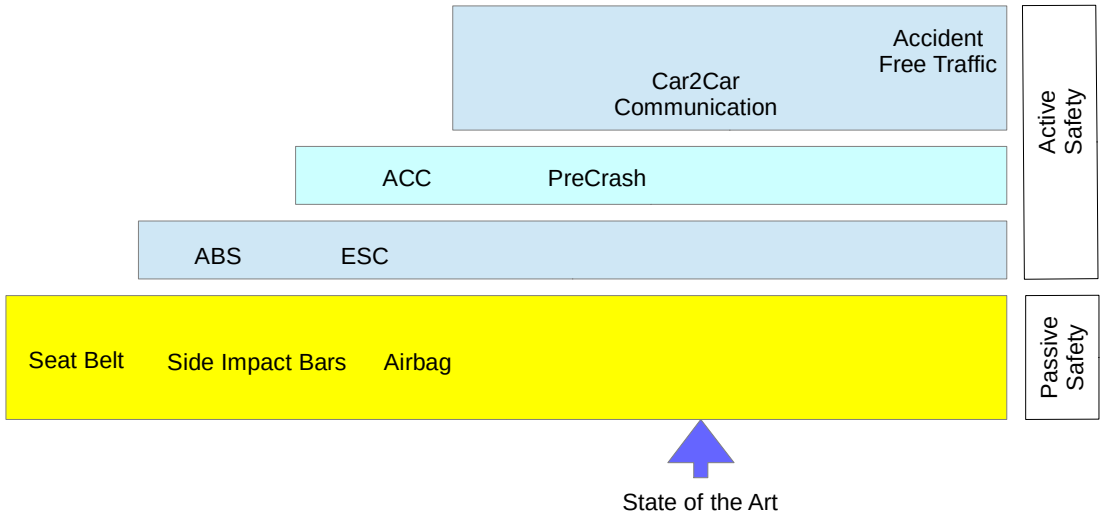

Figure 1.2: Protection potential of automotive integral safety [6]

Other definitions of automotive safety differentiate between active safety systems that prevent accidents and passive safety systems that reduce the impact of a crash as Figure 1.2 shows. The autonomous brake assistant is an example of an active system, while the airbag belongs to the group of passive systems. In the past, both areas were successfully developed separately. Current developments in the automotive industry strive to link active and passive system components to achieve integral safety. Thus, more advanced safety systems can be realised. The cross-linking of various sensors in different systems enables new safety approaches in an economical context.

The aim of advanced safety systems is to use visual, haptic or acoustic warnings to help the driver avoid an accident. Because of his or her experience, vision, and interpretation of critical situations, the driver is the ultimate control system in most situations and thus superior to mechatronic solutions. Faulty operations of the system and a possible liability for the manufacturer can be prevented if the driver can maintain overall control of the vehicle. If the driver does not react within a suitable period of time, the vehicle can intervene autonomously by applying brake force and/or steering torque. Within the period of time just before a crash becomes inevitable, additional pre-crash mechanisms are started [7, 8, 9].

Figure 1.3 shows different systems that have been integrated into a complete system with different triggering levels. A holistic approach to safety functions over the entire crash scenario is necessary to integrate all functions into a combined control system in the future.

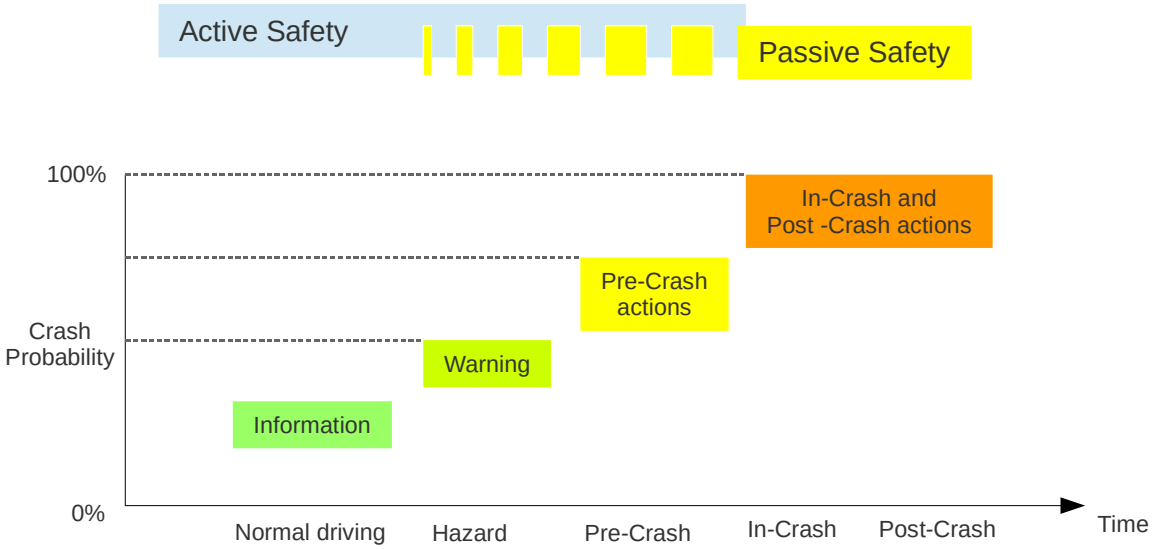

Figure 1.3: The time sequence of possible events

Due to technical reasons such as the resolution of distance sensors, current safety systems do not have access to every piece of information relevant for any given time. Therefore, an intervention only can be started when an imminent collision has been positively identified. During this period of time, the so-called pre-crash phase, the collision is independent of the driving situation and the driver's behaviour which is called the pre-crash phase. Evaluations of the sequence of events in accidents show that avoiding in terms of vehicle dynamics is reached just before a collision. Therefore, only a few hundred milliseconds remain in which the vehicle's speed upon impact can be reduced via brake intervention or by adapting restraint systems. By gathering additional information, for example through advanced sensors, future pre-crash systems will be able to intervene earlier, without influencing the overall safety. The sensors would have to demonstrate a high precision in object identification at an early point in time. In order to ensure the best protection for the vehicle's passengers, the time needed for the actuator to operate the pre-crash systems would need to be less than the remaining time to the collision impact.

Present-day systems are characterized by high complexity. Great effort is still required to link active and passive safety systems. Such a linkage would ensure that sensor information distributed over the whole vehicle could be used for different approaches.

By monitoring and analysing the data flow in a vehicle, it is possible to implement new safety functions based on the existing information. This approach forms the basis of this research project.

1.3 Motivation for the research

According to data collected by Germany's Federal Statistics Office [10], 3600 people died in accidents on German roads in 2012. Compared to the numbers from 2011, 10.2% less people were involved in a fatal accident. This statistics represents the lowest number since starting the record-keeping began in 1953. By comparison, there were 16477 road deaths and 4.5 million cars registered in West Germany in 1960. The number of traffic deaths and registered cars increased over the following years constantly and peaked in 1970 with 21322 traffic deaths and 13.9 million

registered cars. After this point in time the number of traffic deaths decreased continuously, yet the number of registered cars had reached almost 43 million by 2012. A change made in statistical record-keeping in 2008 explains the edge in the curve. Temporarily registered vehicles without a valid license have been left out of the data. Figure 1.4 gives an overview of the development of registered cars and road deaths in Germany over the years.

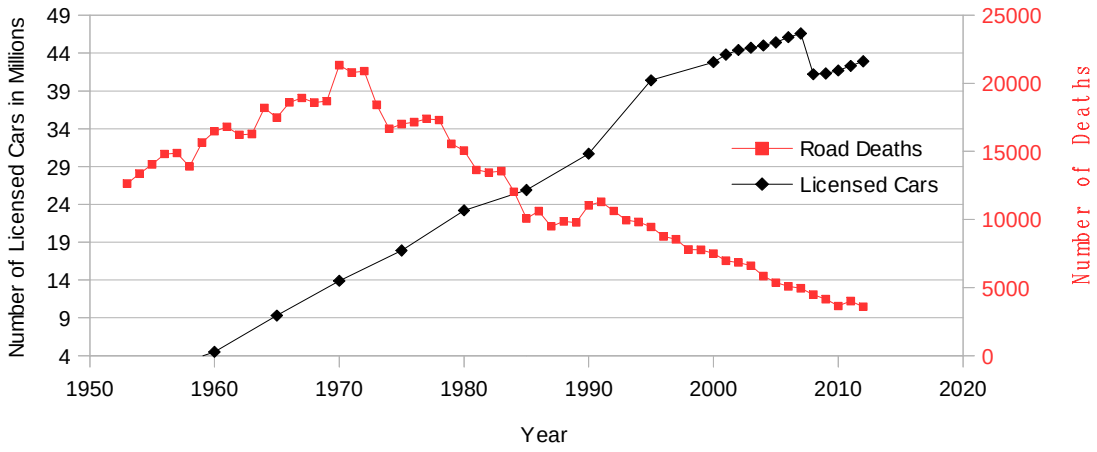

Figure 1.4: Number of registered cars and road deaths over the years

The dip in the road deaths curve reflects legislation passed in 1976 that made the wearing of safety belts compulsory for drivers and passengers. The short rise between 1989 and 1991 is due to the reunion of West and East Germany and the increased number of drivers and registered cars as a result. Thus, the statistics on road kilometres travelled, represented in Figure 1.5 has a step in the mentioned time period. The number of road deaths has decreased steadily since 1991.

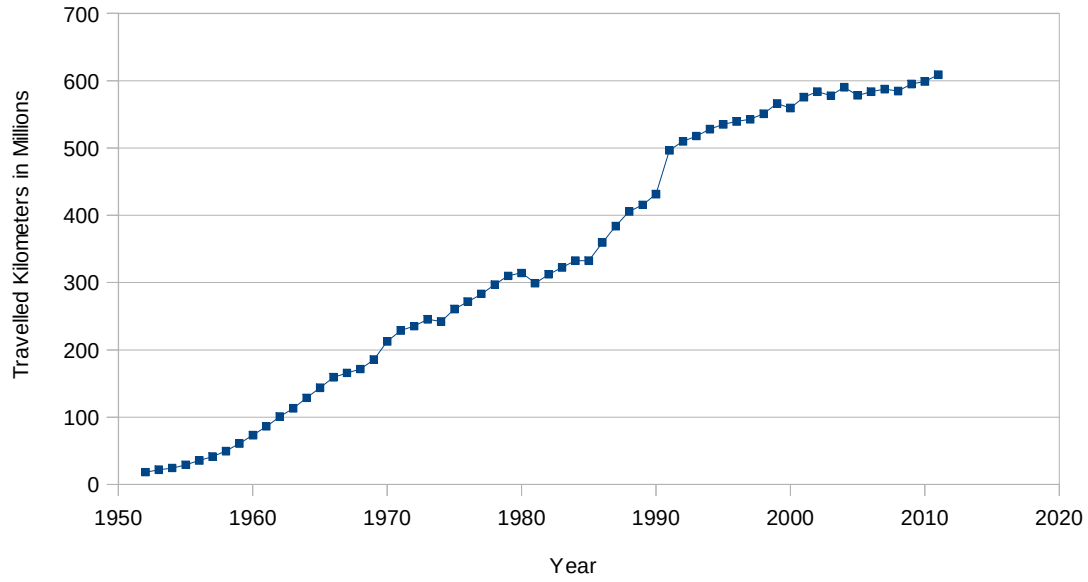

Figure 1.5: Kilometres travelled in Germany for cars over the years [11, 12]

Figure 1.6 distinguishes between the number of serious and slight injuries that have occurred on German roads since 1991. Prior to 1991, only the total number of injuries was recorded. A positive trend can be detected at the turn of the century.

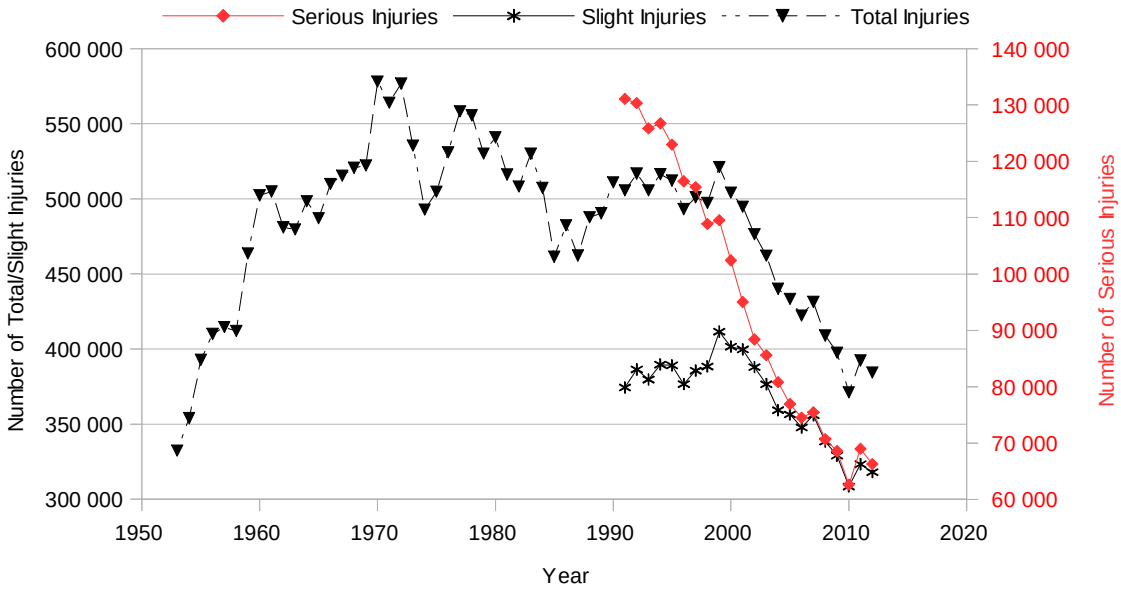

Figure 1.6: Number of total, slight and serious injuries on German roads over the years

The risk of death or injury in a vehicle accident decreased in Germany because of an increase in kilometres travelled. Risk is defined as the number of adverse events in relation to a reference parameter. In this case, the number of road deaths is divided by kilometres travelled. In the EU, the risk (of death or injury in a road accident) differs from country to country, with, very low risk, for example, in Great Britain and Sweden and extremely high in Greece and Spain. Risk reduction can be attributed to improved road systems, rescue services and emergency medical aid, but also to vehicle manufacturers' efforts to increase the road safety. The continuing development of occupant restraint systems from simple seat belts to complex multi-component systems using pretensioners, load limiters and multi-airbag systems are examples of these efforts. The development was triggered by scientific findings in accident research. Accident research has confirmed significant achievements in terms of road safety and has identified more potential areas in which the number of road deaths and injuries can be further reduced. The Federal Statistics Office in Germany keeps records on road accidents which have been reported by the police. The police officers note the location, the circumstances of the accident and the people who were involved. Therefore, a large amount of data is available. However, not all road accidents are reported. Thus, the estimated number of unreported traffic accidents, especially in misdemeanour cases is high. Furthermore, accuracy is limited. At a crash site, additional information on the use of seat belts, seating position or vehicle deformation is not recorded in detail.

After the third road safety program to reduce the total number of road deaths to 20000 in Europe by 2010 [13], many governments, like those of the USA and Japan have also intensified their efforts to increase road safety, because the number of 1.4 million people who lost their lives in 2009 world wide in road traffic [14, 15]. The European Commission set a goal to reduce the number of road deaths halving by 2020 [16]. The development of active and passive safety systems is one potential way to reach the goal. The ability of the vehicle to recognise and interpret its environment, identify dangerous situations ahead and assist the driver as best as possible is essential to the development of active and passive driver assistant systems.

1.4 Aims and objectives

The aim of the project is to investigate the influence of internal tyre pressure on tyre friction. The reduction of collision speed and therefore a further reduction in the severity of an accident and resulting injuries is one possible outcome.

The state-of-the-art systems on the market show that the braking force's real contact point the area of contact between tyre and road surface, is not considered. The physical behaviour of the tyre at the contact area is extremely complicated. The contact area is referred to as tyre contact patch and is described by the physical phenomena of rubber friction. Rubber friction can be described as a combination of adhesive, cohesive and viscous friction as well as hysteresis. Adhesive friction is dominant on dry road surfaces and depends mainly on the rubber material, but also on the real contact area. Rubber friction differs significantly from the friction between two solid objects, in which friction is independent of the contact area. The characteristics of the adhesive friction imply that increasing the tyre contact patch could reduce the braking distance. By decreasing the internal tyre pressure, the tyre contact patch can be enlarged.

An aim of this project is to conceptionally describe a system that, by analysing the in-vehicle bus communication of the car, can immediately detect an emergency braking situation and initiate an autonomous systematic decrease in internal tyre pressure.

To realise such a system, the following components are required:

- An electronic interface to the in-vehicle CAN bus network which the author designed as part of his Master thesis [17]. This interface can be used to trigger the actuator.
- A wheel rim that allows a dynamic decrease in tyre pressure in case of an emergency braking situation.
- A wireless communication interface between the electronic control unit and actuator in the rim.

The main objectives of the present research are:

Objective 1: To conduct a literature review of current research in the areas of rubber friction, tyres and automotive safety.

Objective 2: To identify potential novel automotive safety systems.

Objective 3: To demonstrate the concept of a potential safety system application.

Objective 4: To investigate the influence of internal tyre pressure on vehicles' braking distance of vehicles.

Objective 5: To identify a theoretical approach for explaining the experimental results.

Objective 6: To validate Persson's novel rubber friction law and tyre model by comparing them to experimental results.

1.5 Thesis structure

The thesis is outlined as follows:

Chapter Two

This chapter gives an overview of the history of brake systems, physical principles and describes state-of-the-art predictive safety systems. Additional calculations for triggering an autonomous emergency brake are presented.

Chapter Three

This chapter presents the basics of friction, provides a literature review of previously conducted research on the phenomena of rubber friction, models the linear and viscoelastic deformation of rubber and discusses the development of tyres. The final section of this chapter discusses two recent research projects funded by the European Commission that have investigated options for an intelligent tyre that can predict available friction.

Chapter Four

Chapter four describes the concept of a novel safety system based on a double chamber rim. Thus, the history of rim development is described alongside different production methods to show the feasibility of the system. Additionally, the wireless communication between the sensor system which is fitted to the car and the actuator in the rim is exemplified.

Chapter Five

This chapter presents the experiments that were conducted to investigate the influence of tyre inflation pressure on friction. In the beginning, brake test results are shown using a robot system. The chapter then introduces experimental data, performing extensive brake tests using different car models, provided by Hankook tyres. The chapter concludes with a description of pull tests that were performed using a winch to investigate rubber friction.

Chapter Six

Chapter six gives an introduction to Hertz', Greenwood-Williamson's, Bush's et al. and Persson's theories on contact mechanics. The fact that most real surfaces exhibit surface roughness across many decades of length scales, contact formation between two solids is still not understood very well. Then a rubber friction law is introduced which can be used to calculate tyre and vehicle dynamics.

Chapter Seven

Chapter seven compares the friction law to experimental data. A one- and two-dimensional tyre model is introduced which combines the rubber friction law with a mass-spring description of the tyre body. The tyre model is very flexible and can be applied to different manoeuvres. It can be used for calculating μ-slip curves, self aligning-torque, braking and cornering or combined motion (e.g. braking during cornering). The theory predictions are compared to measured data from indoor tyre testing on sandpaper substrate.

Chapter Eight

This chapter presents simulations of anti-lock braking using two different control algorithms. For the calculations, the 2D tyre model presented in chapter seven is used, and the model includes the phenomenological rubber friction law introduced in chapter six.

Chapter Nine

This chapter summarises the research findings. The achievements are compared to the objectives defined in chapter one. The author's conclusions are presented and the contribution to the field's knowledge is outlined. Finally, areas for future research are addressed.

Chapter TWO

This chapter gives an overview of the history of brake systems, physical principles and describes state-of-the-art predictive safety systems. Additional calculations for triggering an autonomous emergency brake are presented.

2. Basics of brake systems, physical principles and predictive safety

2.1 Brake systems

Brake systems are part of the relevant safety applications for vehicles. In every traffic situation, the safety of a vehicle's occupant and other road users depends on the functional efficiency of the brake system. The original function is the deceleration of a vehicle according to the driver's input independent of the vehicle velocity. Over the last decade, a number of electronically controlled functions have extended the brake systems. Increasing demands for comfort in modern automobiles, the vehicle's increased weight and a greater range in speed have lead to enhanced performance requirements for brake systems.

Some of the most important breakthroughs in the development of automotive brake systems are listed below:

- Till 1925: Mechanically operated drum brakes
- 1925: Invention of hydraulic drum brakes
- 1950: Introduction of vacuum-assisted brake boosters
- 1957: Hydraulic disc brake designed as fixed-calliper
- 1965: First one-channel ABS
- 1987: Traction Control System (TCS)
- 1994: Electronic Brake Force Distribution (EBD)
- 1995: ESC
- 1996: Brake Assist (BA)

- 2001: Electro Hydraulic Brake (EHB)
- 2003: Vehicles with brake energy recuperation

The following parameters determine the basic physical design of a conventional brake system:

- Performance requirements for vehicle and brake system
- The vehicle's empty and gross weight
- Vehicle's load distribution on front and rear axle when empty and loaded
- Maximum speed and acceleration ability
- Wheel base
- The centre of mass and loading of the vehicle
- Wheel and rim size
- Type of tyre
- Developments in the brake system's power supply for example by using vacuums from the combustion engine for the brake boosters [18]

2.2 Physical principles

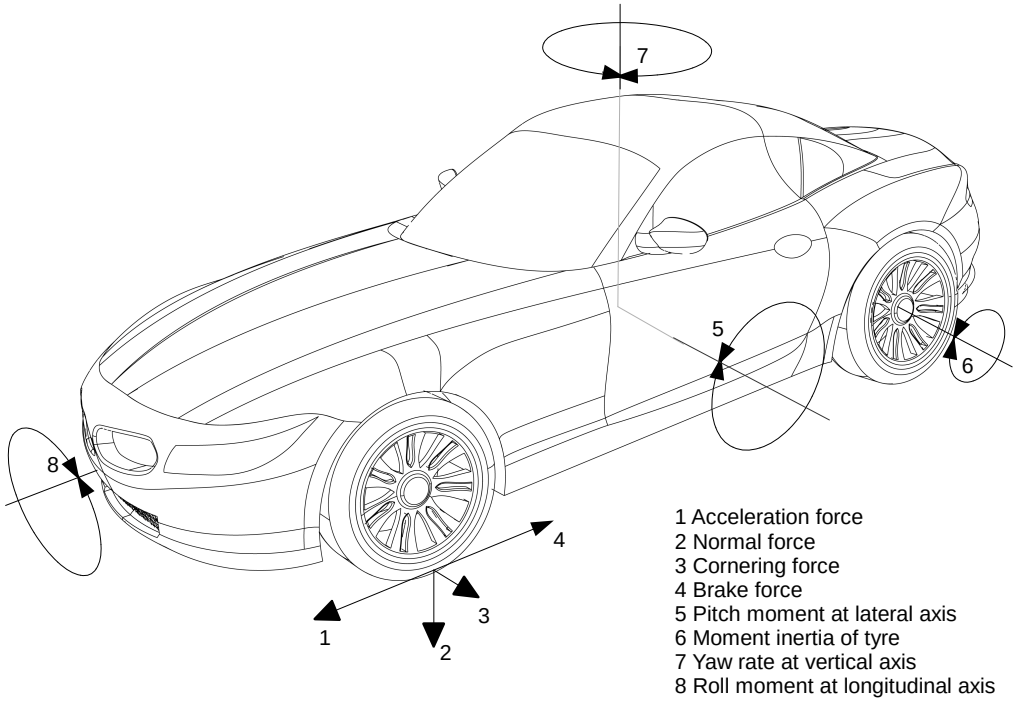

Figure 2.1: Forces and moments acting on the vehicle

Changes in a vehicle's movement (accelerating, braking and steering) are caused by forces. Applied forces, which are directly controlled by the driver, change a vehicle's movement. Friction between the tyres and the road cause these forces. The maximum force of friction depends on the normal load on the tyre, or the so-called wheel load, which is determined by the vehicle's normal load. For this statical component, dynamic parts like the aerodynamic boosts to the normal load are added to the transient driving mode. Axle load shifting during accelerating and braking or cornering, due to the position of centre or bumps in the road, causes dynamic wheel loads that superpose the static proportion. The forces transmitted also vary according to changes in the load during driving.

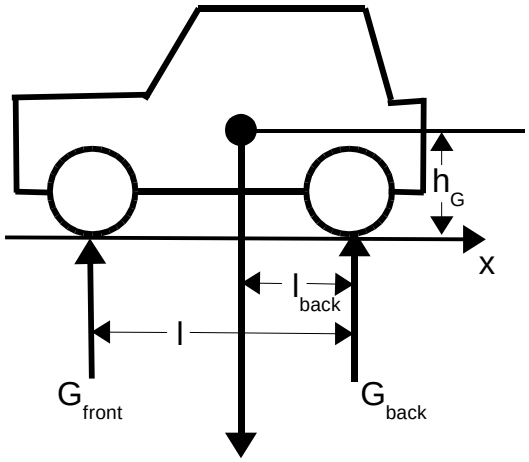

$$G = G_{front} + G_{back} = mg$$

Figure 2.2: Drawing centre of mass

In today's vehicles, brake systems are designed to supply a much higher deceleration than required by law. The braking force transmitted has a physical limit and is restricted by the maximum friction between tyre and road surface. Considering the tyre road friction μ, the gravity g, the vehicle mass m, the aerodynamic up and down force F_{aero} and the delay due to aerodynamic resistance and friction F_{delay}, the maximum possible deceleration can be expressed as follows:

$$\ddot{x} = \mu \cdot g + \frac{\mu \cdot F_{aero}}{m} + \frac{F_{delay}}{m} \qquad \text{(Equation 2.1)}$$

Thus, the maximum brake force on the front axle can be calculated approximately, using the dynamic axle load shift:

$$F_{max,\,front} = \mu \left(m \cdot g \cdot \frac{l_{back}}{l} + F_{aero,\,front} + m \cdot \ddot{x} \cdot \frac{h_G}{l} \right) \qquad \text{(Equation 2.2)}$$

This forms the design background for the wheel brakes. The braking force on the wheels is generated by the actuating force which is created by the pressure of the driver's foot on the brake pedal and the brake booster support. The actuating force is converted into hydraulic pressure in the master cylinder. Somewhat crudely, the following equation can be formulated:

Hydraulic brake pressure p is calculated using the force of the driver's foot F_{driver}, the pedal ratio i, brake booster support V, the area of the master cylinder A_{MC} and the actuation efficiency $\eta_{actuation}$ as variables:

$$p = \frac{F}{A} = \frac{F_{driver}\, i_{pedal}\, V}{A_{MC}} \eta_{actuation} \qquad \text{(Equation 2.3)}$$

Hydraulic pressure acting on the wheel brake cylinders generates a clamping force on the brakes' friction surface. This clamping force generates braking torque on the wheel acting as a braking force on the tyre. This braking force on the wheel F_B is calculated using the hydraulic pressure p, wheel cylinder area A_{WC}, efficiency η_{WC}, internal ratio C, effective friction radius r and the dynamic tyre rolling radius R as variables:

$$F_B = p \cdot A_{WC} \cdot \eta_{WC} \cdot C \frac{r}{R} \qquad \text{(Equation 2.4)}$$

The inner ratio C is also referred to as a brake characteristic value. It describes the ratio of the tangential force and friction force of the brake pads to the clamping force of the wheel cylinder.

$$C = \frac{F_{tangential}}{F_{clamping}} \qquad \text{(Equation 2.5)}$$

The relationship between the tension on the wheel cylinder and the actuating force on the brake pedal is expressed as an external ratio $i_{ä}$. It is also possible to express this ratio by taking the efficiency into account as a relationship between the pedal travel and the clamping travel that also includes the loss of travel on the number of brakes n:

$$i_{ä} = \frac{F_{tension}}{F_{actuation}} = \eta_{actuating} \frac{S_{pedal}}{(n \cdot S_{clamping})} \qquad \text{(Equation 2.6)}$$

To obtain the braking force as a function of foot force applied, the equations above have to be combined. Braking force depends on three sub-systems, the mechanical operation, the hydraulic system and the wheel brakes. However, this only holds in a very simplified form and in a limited scope:

$$F_B = i_{pedal} \cdot V \cdot \eta_{actuation} \cdot \frac{A_{WC}}{A_{MC}} \cdot \eta_{WC} \cdot C \cdot \frac{r}{R} \cdot F_{driver} \qquad \text{(Equation 2.7)}$$

When a driver applies the brakes, the dynamic axle load displacement causes an increase in load on the front axle and a decrease in the load on the rear axle. Therefore, the optimal braking force has to be determined separately for each axle by using the geometrical data of the vehicle and the axle load distribution. These is referred to as the ideal brake force distribution. In the following the dimensionless quantities braking z as a ratio of the vehicle's deceleration to the gravity, the quantity ψ as the ratio between the distance in longitudinal direction l_{front} and the wheelbase l and X as the ratio between the vertical distance h_G and the wheelbase l are introduced:

$$z=\frac{b}{g};\quad \psi=\frac{l_{front}}{l};\quad \mathrm{X}=\frac{h_G}{l} \qquad \text{(Equation 2.8)}$$

Thus, the ideal braking forces for the front (F_{BF}) and rear axle (F_{BB}) can be expressed as a ratio to the vehicle's weight:

$$\frac{F_{BF}}{mg}=[1-\Psi+z\,\mathrm{X}]\,z \qquad \text{(Equation 2.9)}$$

$$\frac{F_{BB}}{mg}=[\Psi-z\,\mathrm{X}]\,z \qquad \text{(Equation 2.10)}$$

Using these equations, the ideal brake force distribution can be deduced as a non-linear function.

$$\frac{F_{BB}}{mg}=\sqrt{\frac{(1-\Psi^2)}{4\,\mathrm{X}^2}+\frac{F_{BF}}{\mathrm{X}\,mg}}-\frac{1-\Psi}{2\mathrm{X}}-\frac{F_{BF}}{mg} \qquad \text{(Equation 2.11)}$$

2.3 Predictive safety systems

Predictive safety systems utilize sensors and the control units of passive and active safety systems to recognize hazardous driving situations. Such systems aim to prevent or mitigate potential accidents.

2.3.1 Origins of the problem

In hazardous driving situations, milliseconds often decide whether an accident happens or not. Earlier studies have shown that about 65% of rear-end collisions, one-third of frontal collisions and about half of crossing accidents could have been prevented if the driver had reacted half a second earlier. In order to set focal points for the development of safety systems that have the highest potential for preventing accidents, accident statistics for Germany are shown in Figure 2.3 using data from the Federal Statistics Office. The second most common type of accidents is rear-end collision, which account 23% of all accident types that have occurred on German roads. Thus there is a high potential for the application of emergency brake systems.

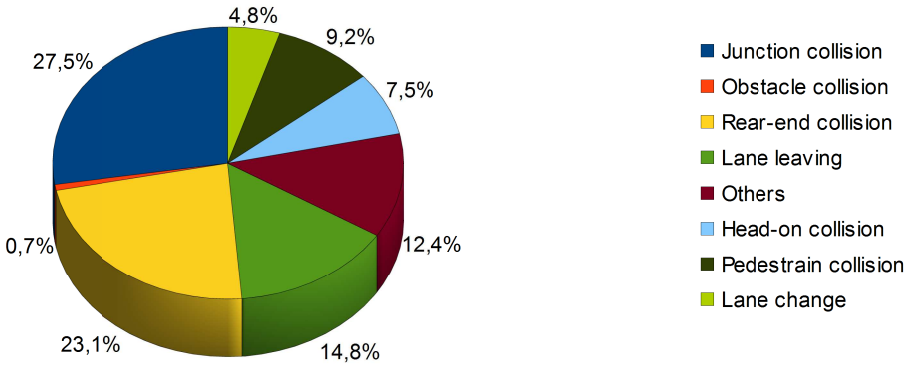

Figure 2.3: Causes of accidents

Figure 2.4 shows the distribution of collision types in Germany between January and August in 2013, with deaths separated from injuries.

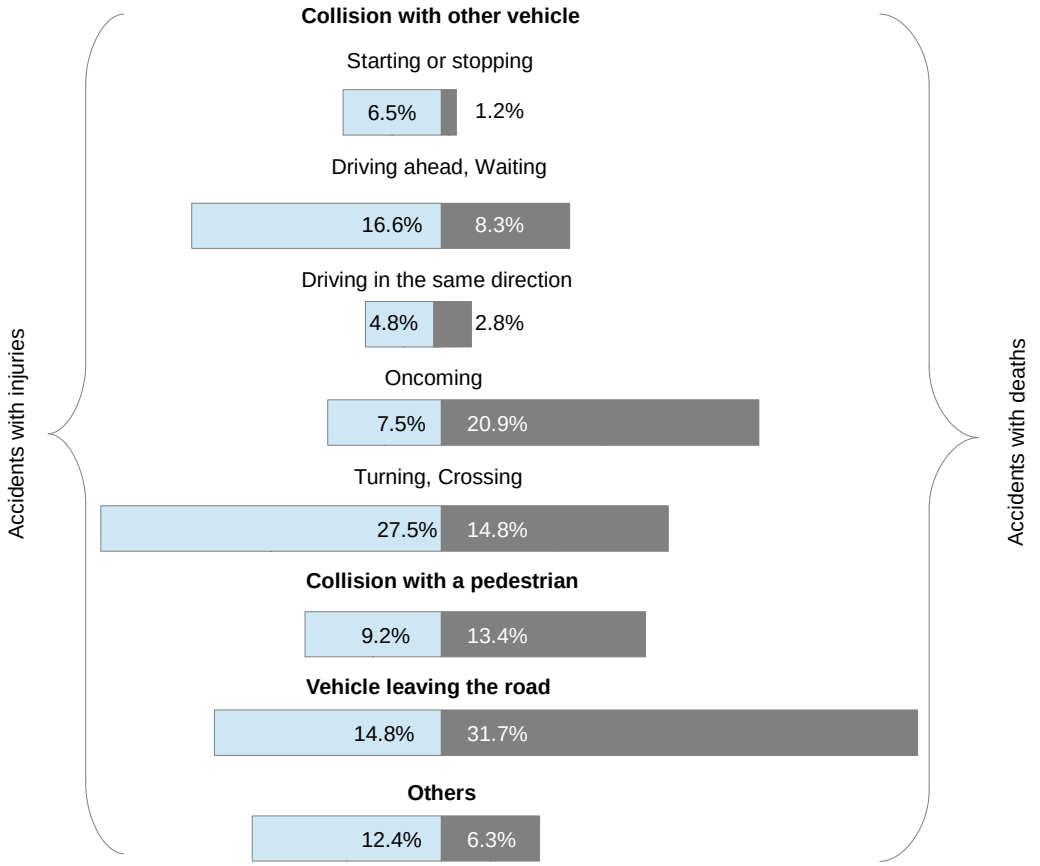

Figure 2.4: Types of accidents

According to the statistics in Figure 2.4, accidents in longitudinal direction account for the type of accident with the most serious injuries and fatalities. Therefore, safety systems engineered to prevent this type of accident must have a high potential for reducing the impact of a crash on a vehicle's occupant.

95% of all accidents on roads can be ascribed, at least in part, to human error. Furthermore, erratic behaviour is the single cause of 75% of accidents. As 68% of all rear-end collisions are caused by inattentiveness, predictive safety systems have a high potential for reducing the number of rear-end collisions. Furthermore, 11% of rear-end collisions are caused by a combination of tailgating and inattentiveness, while in 9% of rear-end collisions are caused by tailgating only.

Figure 2.5 shows an analysis driver's braking behaviours in accidents. True emergency braking is performed in only 2% of all collisions with other vehicles. In 45% of the cases, the brakes were used too tentatively. This trend is shown by the deceleration between 2 and 8 m/s². In over 50% of all collisions, the brakes were either only slightly used, or not used at all. The data confirm that predictive safety systems have a high potential for mitigating or even preventing accidents [19, 20, 21].

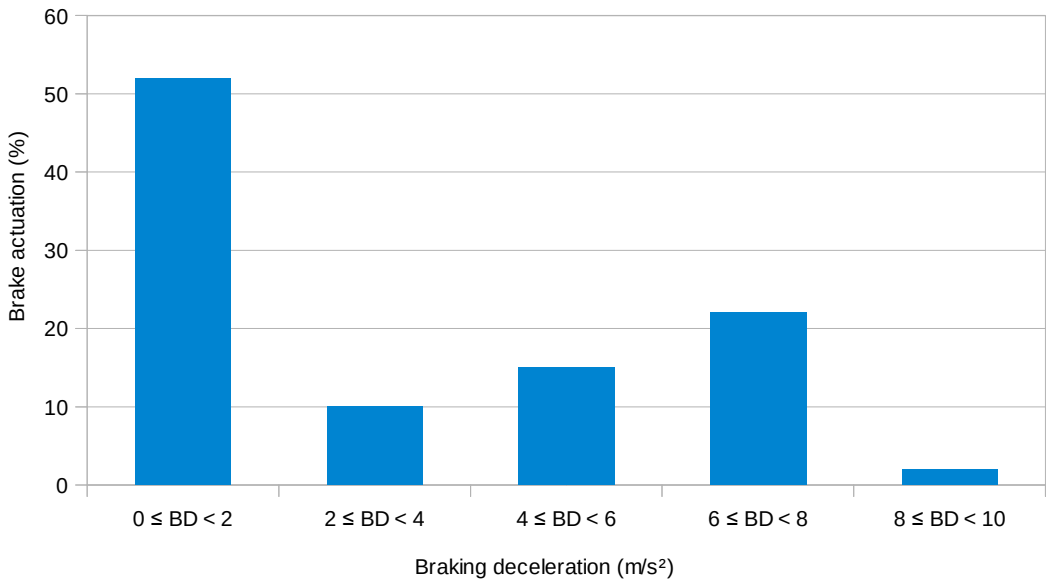

Figure 2.5: Braking behaviour at accidents [22, 23]

Figure 2.6 shows how countermeasures can be deduced. Initially, there is no direct connection between the accident and the incident that might have caused it. Starting from a previous latent danger level, the incident increases this level. However, a high buffer to an actual road accident still exists. Only with increasing time and without an interaction of the driver, the disturbance leads to a crash. An incorrect response has the same effect. An intervention in time from the driver can defuse the critical situation to a near crash event. Structuring the process gives three strategies to protect from accidents which are briefly outlined below. In addition, the implementation of the front collision protection is explained in more detail.

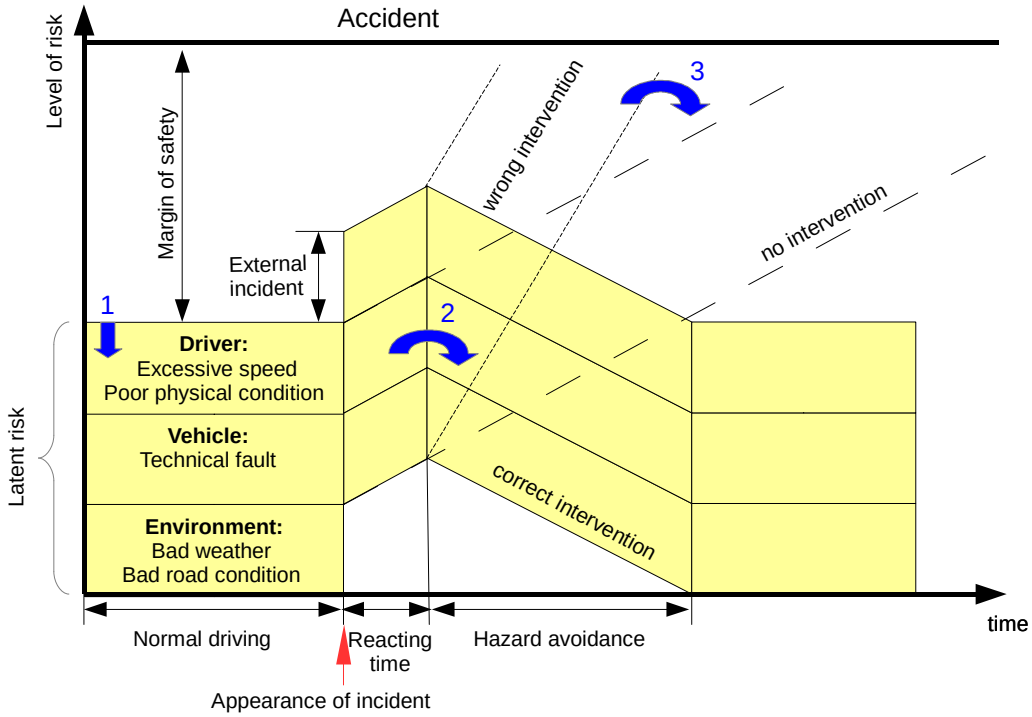

Figure 2.6: Sequence of events in a hazardous traffic situation [24]

1. Preventive assistant:

Accident prevention is reducing the latent level of risk and thus decreasing the risk of getting into a hazardous situation. In the event of a potentially hazardous situation, the system can increase the effective range of action.

2. Response support:

Response support aims to prevent accidents by assisting the driver in hazardous situations. It enables the driver to react properly and in time. Braking or avoiding are the only two viable strategies for preventing accidents in longitudinal traffic. Drivers have become accustomed to assistance provided by autonomously triggered systems such as ABS or ESC. Critical vehicle dynamic situations, especially skidding can be prevented and the driver can go up to the physical limits from the beginning. Nevertheless, accident analysis and experiments with test persons have shown that this option is either used insufficiently or not at all [25, 26].

3. Emergency manoeuvres:

When a driver's reactions are not quick enough to avoid a collision, automatic emergency manoeuvres can intervene at the last second and prevent an accident. Restrictions on the use of autonomous safety systems on public roads that were imposed by the Vienna Convention [27] in 1968 are currently being discussed among EU members. The aim is to allow automated systems to override the driver's actions, when he or she cannot react in time to avoid an accident [28].

2.3.2 Frontal crash protection through prevention assistance

Increasing the driver's ability to handle dangerous situations and increasing the vehicle's dynamic scope of action are two main approaches that can help to reduce the latent risk of an accident. The first approach is limited by the driver's skill and his or her physical and mental condition. Driving skills cannot be improved by assistance systems, but through training and experience. However, assistance systems can simplify the task of driving. Active cruise control (ACC) is one example of such assistance. The psychological and physiological effects of driver assistance systems may contribute to an improvement for the driver's condition. ACC is a very adequate instrument for increasing the available scope of action [29].

The following step-by-step procedure has been used to develop predictive safety systems:

Phase one: Preventive acting occupant protection

Reversible restraint systems are triggered before a collision to give a vehicle's occupants the best possible protection from a potential collision. Preventive occupant protection systems further expand the already high level of passive protection. When the system detects a potential accident situation, seat belts are tightened electrically. By fastening the driver and the passengers to their seats, seat belt restraints maximize the protection potential of the airbags. Additionally at a high transverse momentum, the windows and the sunroof are closed automatically. By closing the windows, the front and side airbags can optimally stabilize the body. Also the passengers are protected from entering objects and the out swing of body parts. The combination of active and

passive safety elements is an essential feature of the occupant protection system. Technical development is based on sensors in vehicle dynamic control systems like brake assist and ESC. These help to identify and mitigate hazardous situations early with an increased protection potential. The activation of the system is started at an emergency or dangerous situation with a quick brake pedal apply. This usually goes hand-in-hand with the activation of the braking assistant or with an ESC intervention in severe over- or understeering situations. In keeping with an integral safety approach, the preventive occupant protection system acts together with environmental sensors from the automatic distance control (ADC). Using systems like radar sensors and camera technology that monitor the road ahead, the vehicle's environment can be analysed and the driver can be warned of an impending collision. Braking interventions up to autonomous emergency braking can also assist the driver. In particular the connection between the emergency braking system and the reversible seat belt pretensioners effectively reduces the occupants' forward displacement.

Phase two: Support for optimal braking

In the first stage, the brake system is prepared for a possible emergency brake situation. In hazardous situations, the brake assistant calculates the optimal braking pressure required for an upcoming vehicle braking to stop the vehicle as quickly as possible. Therefore, the brake system's accumulator is appropriately filled. As soon as an emergency braking is performed, the driver gains the optimal deceleration and therefore the shortest braking distance. In the event of an accident, the system can mitigate the consequences and thereby also save lives. As mentioned before, in about half of all collisions, a vehicle collides with an obstacle without the driver's having applied the brakes. For this type of accident, two advanced generations of autonomous brake systems have been developed. The series was introduced in 2005. In addition, this series was the first to take the safety of other traffic participants into consideration. One example of this is the automatic lifting of the engine bonnet in collisions between cars and pedestrians.

Phase three: Warning of potential collisions

Second generation predictive safety system not only prepare the brake system for an emergency braking situation, but also optically and acoustically warn the driver about hazardous traffic situations in time. Thus, many accidents can be prevented. When the driver does not react to the warnings, a short, but forceful brake impulse will also be triggered. Another way to warn the driver about a dangerous situation is to tighten the seat belt for a short period of time. Studies have shown that kinaesthetic warnings help to bring the driver's attention back to driving the car. This kind of system helps to handle the risk of reckless or inattentive driving. The series was introduced in 2006.

Phase four: Emergency actions

If the driver still does not respond to the warnings, the system can intervene at the very last second in order to avoid or to reduce the impact of a collision. Autonomous avoidance manoeuvres are only more effective than braking manoeuvres at high velocities when the avoidance manoeuvre does not lead to a second collision for example with on-coming traffic. The project PRORETA [30] investigates the realization of avoidance applications. To manoeuvre a vehicle around an obstacle an autonomous steering impulse is added to the current steering angle. State-of-the-art systems for analysing the environment are not good enough for triggering autonomous avoidance manoeuvres.

However, the autonomous emergency brake is already on the market. The system initially applies a moderate force to the brakes. If there is still no reaction from the driver, the system increases the braking force. The automatic emergency brake only is triggered when the system detects that a collision cannot be avoided any longer. The system then uses the maximum available vehicle deceleration to reduce the impact of the collision. Using a technical system to automatically control a vehicle requires a very high level of security to detect objects and very accurate estimates of the risk of an accident. To support the classification of objects, for example, radar sensor signals are combined with video signals [31].

2.3.3 Moments of warnings and interventions

The following section discusses warning and intervention times based on vehicle dynamics and driving behaviour which can be useful in frontal crash situations. There are basically two possible approaches for interventions:

- Acceleration criteria: Acceleration criteria is needed to avoid collisions and includes the required longitudinal deceleration and lateral acceleration, respectively.
- Time criteria: Time criteria includes time threshold evasion, time to stop, time threshold brake and time to collision. A time reserve is needed to avoid collisions.

For the time criteria current distance, acceleration and speed values are used and compared with time thresholds. Assumptions are made about the maximum possible deceleration and lateral acceleration. Warnings can increase the assumed response time. However, to determine the acceleration criteria, the vehicle dynamic approach is easy. It is sufficient to compare the current values with the assumed maximum values for acceleration. The advantage disappears when the reaction time, like for warning strategies, or the system's downtime need to be considered in the calculations. The relevant equations and threshold values for both criteria are presented below. Both have pros and cons. Calculations for avoidance manoeuvres are more easily represented using the time criteria, while for braking situations the accelerating criteria is more convenient.

The least complex situation, referred as case 1, is an unaccelerated obstacle, therefore it is moving with a constant speed or is in a stationary position. Case 2 presents the derivations of the criteria for an obstacle moving with a constant relative acceleration. In case 3 the deceleration of an obstacle leads to a stop before the vehicle reaches the obstacle.

Case 1:

If an obstacle is moving at a constant speed, it is still possible to calculate all parameters relative to this object. Thus, all results correspond to the case of a stationary obstacle. The negative relative velocity $-v_{rel}$ replaces the absolute velocity v_x as the differential velocity v_{diff}. The distance d replaces the absolute position s. Hence the stopping position $s_B(v_{xv,0})$ from the initial velocity $v_{xv,0}$ can be equated with the braking distance $d_B(v_{diff})$. For today's brake systems, the braking distance can be calculated in good approximation using:

$$d_B(v_{diff,0}) = v_{diff,0} \cdot \tau_B + \frac{v_{diff}^2}{2D_{max}} \qquad \text{(Equation 2.12)}$$

The loss of braking time τ_B takes the delay caused by the build-up into account. With an assumed linear increase of the deceleration to maximum deceleration D_{max} in time s, the loss of braking time can be converged with $\tau_s/2$. In this calculation, the error in the braking distance will be in the area of centimetres. The time needed for the brakes to react is around 50 ms. The driver reaction time τ_R consists of detection time, reacting time and implementation time. Common values are between 0.5 and 1.5 sec. Example calculations use the value τ_R = 1 sec which in normal driving conditions is significantly too high [32].

To inform the driver in time of an emergency braking situation the warning distance d_{warn} adds to the braking loss time, shown in Equation 2.12, the reaction time τ_R of the driver:

$$d_{warn}(v_{diff}) = v_{diff} \cdot (\tau_B + \tau_R) + \frac{v_{diff}^2}{2D_{max}} \qquad \text{(Equation 2.13)}$$

To gain the dimension of time to collision t_{tC}, the current distance d needs to be set into relation with the differential speed v_{diff}:

$$t_{tC} = \frac{d}{v_{diff}}; d, v_{diff} > 0 \qquad \text{(Equation 2.14)}$$

The Equations 2.12 and 2.13 can be simplified to:

$$t_{tB}(v_{diff,0}) = \tau_B + \frac{t_{ts}(v_{diff}, D_{max})}{2}$$ (Equation 2.15)

with a time threshold brake t_{tB} and time to stop t_{tS}:

$$t_{tS}(v, D_{max}) = \frac{v_{diff}}{D_{max}}$$ (Equation 2.16)

and correspondingly:

$$t_{tc,warn}(v_{diff}) = \tau_R + t_{tC,B}(v_{diff})$$ (Equation 2.17)

The duration for full braking t_{tS} is twice as t_{tC} at the beginning of braking. As long as a constant and positive relative delay is given, the principle can be applied to the following approach. In addition to the time and distance description, the current required deceleration D_{req} can be determined. The simplest case with an obstacle at a constant velocity can be expressed as follows:

$$D_{req} = \frac{v_{diff}^2}{2\mathrm{d}}$$ (Equation 2.18)

Case 2:

For an obstacle moving at a constant acceleration a_{obs}, the respectively delay -D_{obs}, t_{tC} depends on the relative delay between obstacle and the vehicle, which is defined as ego vehicle.

$$D_{rel} = D_{obs} - D_{ego}$$

$$t_{tC}(D_{rel}) = \frac{\sqrt{v_{diff}^2 + 2\mathrm{D}_{rel}\, d} - v_{diff}}{D_{rel}}$$ (Equation 2.19)

$$v_{diff}^2 > 2\mathrm{D}_{rel}\, d$$

$t_{tC}(D_{rel})$ stands also for enhanced time to collision (ETTC). For negligible relative acceleration Equation 2.19 goes over in limit value consideration shown in Equation 2.14.

To express braking in time behind a decelerating obstacle, $D_{obs} > 0$, the required ETTC is calculated from the maximum relative deceleration as follows:

$$D_{max,rel} = D_{max} - D_{obs}$$ (Equation 2.20)

$$t_{tB}(v_{diff}, D_{rel}) = \tau_B + \frac{t_{tS}(v_{diff} + D_{rel} \cdot \tau_B, D_{max,rel})}{2}$$ (Equation 2.21)

$$t_{warn}(v_{diff}, D_{rel}) = \tau_R + t_{tB}(v_{diff}, D_{rel})$$ (Equation 2.22)

$$d_B(v_{diff}, a_{rel}) = (v_{diff} + D_{rel}\frac{\tau_B}{2}) \cdot \tau_B + \frac{(v_{diff} + D_{rel} \cdot \tau_B)^2}{(2D_{max,rel})}$$ (Equation 2.23)

$$d_{warn}(v_{diff}, a_{rel}) = (v_{diff} + D_{rel}\tau_B + \frac{\tau_R}{2}) \cdot (\tau_B + \tau_R) + \frac{(v_{diff} + D_{rel} \cdot (\tau_B + \tau_R))^2}{(2D_{max,rel})}$$ (Equation 2.24)

The obstacle's deceleration reduces the vehicle's maximum deceleration and results in a greater braking distance. For the warning threshold, the relative velocity is increased significantly in the reaction time τ_R and D_{rel}. The criteria of the required delay D_{req}, does not apply the relative delay, but instead additionally Equation 2.18 for the absolute obstacle delay D_{obs}:

$$D_{req} = D_{obs} + \frac{v_{diff}^2}{2d}$$ (Equation 2.25)

Compared to v_{obs} = constant in the previous case, the brake application must be initiated earlier, therefore at larger distances for a decelerating obstacle. The reason is the deceleration decreases the relative deceleration ability as Equation 2.20 has shown.

Case 3:

This case is between the previous shown situations. t_{tC} increases, when the obstacle with the absolute velocity v_{obs} reaches standstill before the vehicle arrives. So, when:

$$\frac{v_{obs}}{D_{obs}} < t_B(v_{diff}, a_{rel}) \quad \text{or:} \quad \frac{v_{obs}}{D_{obs}} < t_{warn}(v_{diff}, a_{rel})$$

The required distances for stopping and avoiding are decreasing compared with the Equations 2.19 to 2.25:

$$t_{tC}(v_{obs}, D_{obs}) = \frac{v_{\text{sub}} - \sqrt{v_{\text{sub}}^2 - 2\text{D}_{\text{sub}} \cdot d - v_{obs}^2 \frac{D_{\text{sub}}}{D_{obs}}}}{D_{\text{sub}}}$$

with

$$\left(v_{\text{sub}}^2 - 2\text{D}_{\text{sub}} \cdot d - v_{obs}^2 \frac{D_{\text{sub}}}{D_{obs}}\right) > 0 \qquad \text{(Equation 2.26)}$$

Hence, there is a braking distance required which the braking distance of the vehicle minus the obstacle plus the loss of braking time results to:

$$d_B(v_{obs}, D_{obs}) = \frac{v_{\text{sub}}^2}{2\text{D}_{max}} - \frac{v_{obs}^2}{2\text{D}_{obs}} + v_{\text{sub}} \cdot \tau_B \qquad \text{(Equation 2.27)}$$

For this case the time criteria t_{tB} is not simplifying Equation 2.27 which can be seen in Equation 2.26. For the warning distance Equation 2.16 is multiplied with the reaction time and the average differential velocity to get the warning distance:

$$d_{warn}(v_{obs}, D_{obs}) = \frac{v_{\text{sub}}^2}{2\text{D}_{mas}} - \frac{v_{obs}^2}{2\text{D}_{obs}} + v_{\text{sub}} \cdot \tau_B + \left(v_{diff} + \frac{D_{rel} \cdot \tau_R}{2}\right) \cdot \tau_R \qquad \text{(Equation 2.28)}$$

The required delay $D_{req}(v_{obs}, D_{obs})$ is calculated with a summation of the current distance d and the braking distance $v^2_{obs}/2D_{obs}$ of the vehicle in front which is the obstacle:

$$D_{req}(v_{obs}, D_{obs}) = \frac{v_{\text{sub}}^2}{2\left(d + \frac{v_{\text{sub}}^2}{2\text{D}_{obs}}\right)} \qquad \text{(Equation 2.29)}$$

The result is near the values for an unaccelerated obstacle, when v_{obs}/D_{obs} is small (Equation 2.18) and when v_{obs}/D_{obs} is big (Equation 2.25) with a permanent decelerating obstacle. In all three cases, unaccelerated, constant accelerated and the obstacle is braking until stop can be determined by:

$$D_{req}(v_{obs}, D_{obs}) = \text{MIN}\left(\frac{v_{\text{sub}}^2}{2\left(d + \frac{v_{obs}^2}{2\text{D}_{obs}}\right)}; D_{obs} + \frac{v_{\text{sub}}^2}{2\text{d}}\right) \qquad \text{(Equation 2.30)}$$

2.3.4 Frontal collision countermeasures

To avoid collisions and increase crashworthiness, notifying and autonomous actions can be applied. Notifying systems aim to avoid a collision, while interacting systems additionally try to reduce the impact of a collision. In the following the presented measures are implemented partly or as a whole package. A measure that is initiated at a later stage, should principally lead to a stronger braking intervention. The measures are standardized in ISO 15623:2013 “Intelligent transport system – Forward vehicle collision warning system – Performance requirements and test procedures” for warning systems and in ISO 22839:2013 “Intelligent transport systems – Forward vehicle collision mitigation systems – Operation, performance, and verification requirements” for intervention systems.

Collision warning:

Especially widely used are auditive warnings with mostly short warning sounds which are complemented by a flashing visual warning sign. A reversible seat belt tensioner may also be used as an alert method. Example vehicles are the Lexus LS, the Mercedes Benz S-Class or the Honda Legend. An active accelerator pedal, developed by Continental, can also be used as haptic warning method. The pedal gives pulsed jerks to the driver's foot. However, it is necessary for the cognition, that the acceleration pedal is applied which is not the case in all critical situations.

Weak braking initiation:

It is possible to apply autonomous vehicle dynamic countermeasures with two options:

1. Warning brake:

The main effect is a haptic alarm with an explicit braking request for the driver. An exemplar pulse with a typical deceleration amplitude of 2 m/s² with a duration of 0.3 sec causes a speed reduction of 2 m/s. Thus for a differential speed of 20 m/s the reduction of the kinetic energy, respectively the braking distance is 20%.

2. Speed reduction braking (SRB):

With a partial braking of 30 - 40% of the maximum deceleration, a big warning effect with a significant reduction of kinetic energy can be achieved. Beginning at t_{tC} of 1.5 sec and a deceleration of 4 m/s², the driving velocity can be reduced by 12 m/s to an obstacle which is not decelerating. However, at such an early triggering it has to be ensured that the driver can still override the system. If a possible avoidance is detected, the braking intervention has to be released as the pedal application is indicating a different driver input. Also it needs to be excluded, that the pedal application is not due to the autonomous pedal pulse. A further method to reduce potential damage of an error intervention is the limitation of the interference time. Controlled road tests have shown, that an autonomous braking accelerates the reaction of the driver. The driver is not reacting later than 1.3 sec, as long as a hazardous situation is present.

Mitigation braking:

A strong braking intervention, defined as at least 50% of the maximum deceleration ability, can be applied when no avoidance is imposed. In current vehicle applications at t_{tC} of 1 sec, a strong braking with a deceleration of 6 m/s² is executed. A reduction between 6 and 12 m/s can be achieved. Basically an even stronger braking intervention has a bigger effect. However, this can have a negative effect, because the brake impulse may shift the body and head of the vehicle occupant to an unsafe position for triggering airbag or the seat belt tensioner. When the seat belt tensioner is applied simultaneous to the brake impulse, this effect can be reduced significantly.

2.3.5 Potential of collision countermeasures

The benefit of frontal collision countermeasures is the avoidance of head on collisions and the reduction of the damage, when a collision is inevitable. The previously presented calculations have already shown, that the effect depends mainly on the initial situation whether a collision is avoidable or not and how strong the reduction of stress can be. To determine the benefit independently of the initial situation, the effectively decreased velocity is specified. However, even for an idealised system, the effectively decreased velocity depends on the initial velocity. The following example for the stationary obstacle will illustrate the context. It is an idealized emergency brake assumed. The emergency brake is triggered at t_{tB} and causes a deceleration of D_0. With an initial velocity of $v_0 = 2t_{tB} \cdot D_0$ a collision can just be avoided. Thus, the speed can be reduced to $\Delta v = v_0 = 2t_{tB} \cdot D_0$. In contrast, when the initial velocity is very high, $v_1 >> 2t_{tB} \cdot D_0$, the speed is only reduced by half. To gain a comparable parameter, only the difference to the initial velocity is considered, when t_i is t_{tC}. Thus, the collision mitigation velocity $\Delta v_{CM} = v_{sub}(t_i) - v_{sub}(t_i + t_{tB})$. The definition of effectiveness allows both, the simple estimation of idealized collision countermeasures as well as a solution independently objective of an evaluation of the action. Even a comparative evaluation of an autonomous intervention system and driver assistant systems are possible.

Chapter THREE

This chapter presents the basics of friction, provides a literature review of previously conducted research on the phenomena of rubber friction, models the linear and viscoelastic deformation of rubber and discusses the development of tyres. The final section of this chapter discusses two recent research projects funded by the European Commission that have investigated options for an intelligent tyre that can predict available friction.

3. Literature review of rubber friction and tyres

3.1 Fundamentals of friction

The coefficient of friction describes the ratio between the frictional force and the force which is pressing two bodies together. It is symbolized by μ with a dimensionless scalar value and depends on the materials which are in contact. The coefficient of friction needs to be differentiated between static, also called stiction, and sliding friction.

To enable relative motion of stationary objects which are in contact with each other, the stiction needs to be overcome. This means the stiction is the maximum and occurs between two or more physical solid objects not moving relatively to each other [33].

The static and sliding friction can be calculated by using the coefficient of friction times the normal force expressed with the formula:

$$f = \mu \cdot F_N \qquad \text{(Equation 3.1)}$$

The maximum frictional force that can be produced between surfaces without slipping is called traction.

Traction is only possible if a relative motion between the frictional partner exists. This means, according to the operating mode (e.g. braking or accelerating), the circumferential speed v_t of the wheel is bigger or smaller than the driving velocity. This process is called slip and is expressed as:

$$s = \frac{v_t - v}{v} \qquad \text{(Equation 3.2)}$$

using:

$$v_t = \omega \cdot r_{dyn} \qquad \text{(Equation 3.3)}$$

The relation of the friction and slip is illustrated using μ–slip curves, shown by example for braking in Figure 3.1.

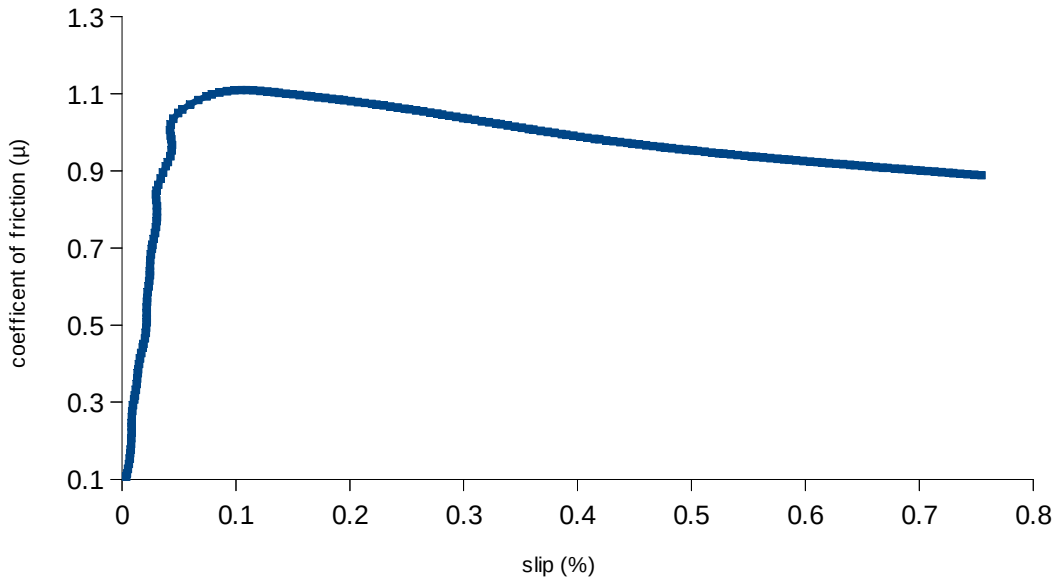

Figure 3.1: The coefficient of friction in relation to the braking slip

The friction of the objects in contact depends on different criteria:

- The material of the frictional partners.
- The surface.
- The load distribution in the contact area.
- If existing, on an intermediary layer, e.g. water, dust.

3.1.1 Historical Review

The friction between two objects is independent of the contact pattern and proportional to the applied weight which was discovered by Da Vinci in 1500. These findings were lost and later rediscovered by Amontons in 1699. Further, Amontons [34] noticed that the friction depends on the material of the related objects. Together with 'de la Hire', he described the friction as a mechanic form closure between the coarseness of the contact pattern. Sliding friction is the demanded force to lift the peaks of the top object surface over the surface peaks of the bottom object. This theory can be refuted, because most of the energy for the lifting can be regained by the draw off.

The physicist Charles Coulomb [35] confirmed Amontons results and determined in 1785 that stiction is bigger than sliding friction. He defined the necessary force to bring an object into motion on a clean surface. In many cases the stiction is twice as high as the sliding friction. The forces neither depend on the contact pattern of the object nor its velocity, but only on its weight. Just about that time Euler introduced the friction coefficient μ.

Ewing (1892), Tomlinson (1929) [36] and Hardy (1936) assumed, that a molecular attraction between the frictional partners exists. In their theory the friction is attributed to the energy dissipation at the pull out of the atoms in the contact pattern.

Bowden and Tabor (1954) developed a theory of bonding, shearing and grooving [37]. In accordance with that, friction is caused on metallic surfaces through a local bonding. In case of a load, the bonding is sheared and the structure which is indurated by the bonding, is grooving through the softer surface of the contact partner. This local limited effect is often repeated. This theory is not explaining the origin of the bonding.

Schnurman (1961) assumed that electrostatic effects are responsible for the slip-stick phenomenon. But this assumption was vitiated by Kummer in 1966 experimentally [38].

Beside the theoretical investigations, research of the frictional coefficient is a special discipline of automotive engineering. The importance of traction as a condition of safe transportation was perceived relatively early. This is the reason why the research of friction is part of road safety and the development of vehicles.

Historical data are listed in the following:

- 1900: With the appearance of the rubber tyre, the problem of vehicle sliding was identified. In 1895, “The Automobile” started to discuss the difficulty of traction at cornering and braking [39].
- 1920: Sliding friction measurements of tyres on different road surfaces was necessary to satisfy the increasing traffic [40].
- 1930: Statements about sliding friction can be used for vehicle dynamic purposes. First laboratory test rigs and measurement trailers are developed to investigate the fundamental tyre and road properties in more detail. These efforts are shown in the multiplicity of international research activities.

For Germany the following studies are mentioned:

- Brix: Experiments of safe driving on tar and asphalt [41].
- Schenk: Friction and slipperiness of the road surface [42].
- Weil: About the frictional coefficient between tyre and road.
- Gölz: Road coating and vehicle [43, 44, 45].

Similar investigations in the USA were:

- Stinson, Roberts: Coefficients of friction between tires and road surfaces [46].
- Moyer: Skidding characteristics of road surfaces [47].

Further research around 1930 from England, Sweden and Switzerland:

- Bird, Scott: Studies in road friction [48].
- Andersen, Lundeberg: Notification 35 of the Swedish road institution.
- Schindler: The static and dynamic road friction and instruments for determination [49].

Comparatively many articles are from the early 1940's. After the second world war investigations in the area of friction were continued. The key data of the post war development are:

- 1954, Riekert: Development of a one wheeled measurement trailer with parallelogram system, named “Stuttgarter Reibungsmesser” (SRM). This device is used up to now for grip measurement at road constructions.
- 1959: First International Skid Prevention Conference, Charlottesville, Virginia [50].
- 1966, Kummer: Unified theory of rubber and tire friction.
- 1968: International Colloquium of road traction and traffic safety in wet conditions, Berlin, Germany.
- 1977: Second International Skid Prevention Conference Columbus, Ohio [51].
- 1981: Frictional Interaction of Tire and Pavement; Conference Akron-Fairlawn, Ohio [52].
- 1992: First International Experiment to compare and harmonize texture and skid resistance measurements; World Road Association PIARC [53].

3.1.2 Rubber friction

Bowden and Tabor developed the theory, that the frictional force between two components is a mixture of the adhesion component and the deformation component. This theory was modified by Kragelski, Dobycin and Kambalov [54, 55].

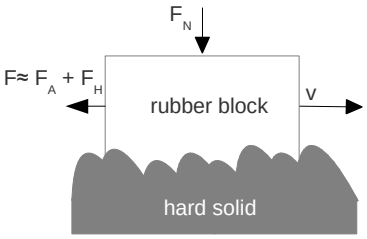

Figure 3.2: Fundamental process of rubber friction

Using this approach, Kummer sub-classifies the sliding friction in interface losses and bulk losses near the surface of the solid body, shown in Figure 3.3. The bulk loss has effects of deformation and cohesion. The deformation losses can be split into separate components again. For stiction, mechanical interlocking and adhesion occurs which is illustrated in Figure 3.3.

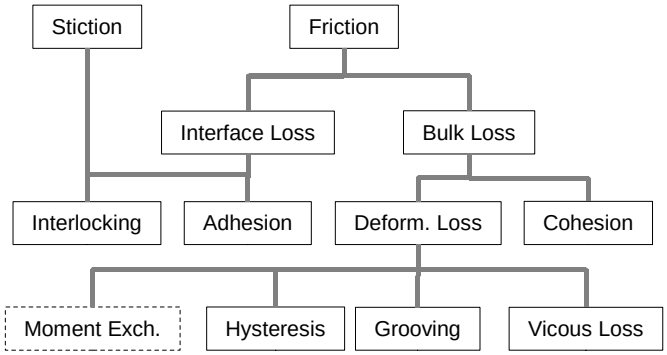

Figure 3.3: Outline of rubber friction terms by Kummer

Together with Meyer, Kummer discovered the dependency of rubber friction on the normal load, the sliding velocity and the temperature. This is contrary to the Coulomb friction theory.

Rieger and Geyer expanded the approach theoretically and experimentally [56]. In addition, Rieger investigated friction on wet road surfaces. Fink, Weber and Wilkinson analysed experimentally the friction of rubber on ice. Schallamach worked on the ration of friction, especially in the change between stand still and sliding.

However, including the book “Mechanics of Pneumatic Tires” by Clark [57], there is no satisfying theory which describes the friction of polymers.

Fundamental principle of rubber friction:

The basics of rubber friction are the mechanical properties of the rubber compound. The chemical structure of the filiform rubber molecule chains gives a fundamental explanation. These chains are statically entangled and in larger segments flexible. Mainly responsible for the rubber properties are the shape and the crosslinking density of the molecules. Rubber is characterised by its temperature dependency, the extraordinary variation capability and belongs to the group of elastomers.

Viscoelastic properties:

Pure elastic behaviour is described by the Hooke's law, where a linear relation between strain and stress exists. In contrast, for materials with viscoelastic behaviour, the generalized Newtonian fluid gives the relation between the shear stress and the gradient of velocity.

$$\tau = \dot{\gamma} \cdot \eta \qquad \text{(Equation 3.4)}$$

Viscoelastic materials show both, elastic and viscous behaviour. For ideal elastic bodies, the deformation energy is stored in the object and recovered when the strain is relieved. For ideal fluids, however, all the energy is transformed into heat. If external forces are applied on a viscoelastic object, the object reacts with a partial transformation in heating and storing the energy in deformation. The properties depend on the time period of the stress and are difficult to express in mathematical equations. A simplification is the limitation to linear viscoelastic behaviour which can be easily illustrated in models. For simplifying, the validity of the Boltzmann superposition principle is required [58]:

1. The sum of two time independent deformations $\varepsilon_1(t) + \varepsilon_2(t)$ causes the stress $\sigma_1(t) + \sigma_2(t)$.
2. The sum of two stresses $\sigma_1(t) + \sigma_2(t)$ causes the deformation $\varepsilon_1(t) + \varepsilon_2(t)$, if $\sigma_1(t)$ induces $\varepsilon_1(t)$ and accordingly $\sigma_2(t)$ the deformation $\varepsilon_2(t)$.

The mathematical description is challenging, as the rubber is behaving non-linearly and changes its behaviour over the time. To model the characteristics, great effort is necessary for the simulation. Reproducing the behaviour can be achieved by using springs, damping or friction elements which describe the rubber behaviour at different strain velocities.

The elastic behaviour determines the rubber characteristic in general. This is often described by a non-linear spring. The spring represents both, the non-linearity of the strain stress curve and considers the incompressibility.

The viscous part describes the frequency dependent rigidity of the rubber material and the temperature sensitivity. For high frequencies or for low temperatures, the rubber is stiffer for strain and stress.

For creating general models ideal elastic and viscous shears are used. They are represented with mechanical spring and damping elements. When they are connected parallel, it is called a Voigt-Kelvin model, while a series connection named as the Maxwell model. The deformation is superposing and the relaxation test is simulated with the Maxwell model, while the Voigt-Kelvin model is superposing the stress and approximates the creep test. For real materials an infinity parallel connection of Maxwell models or a series connection of Voigt-Kelvin models are a good approximation.

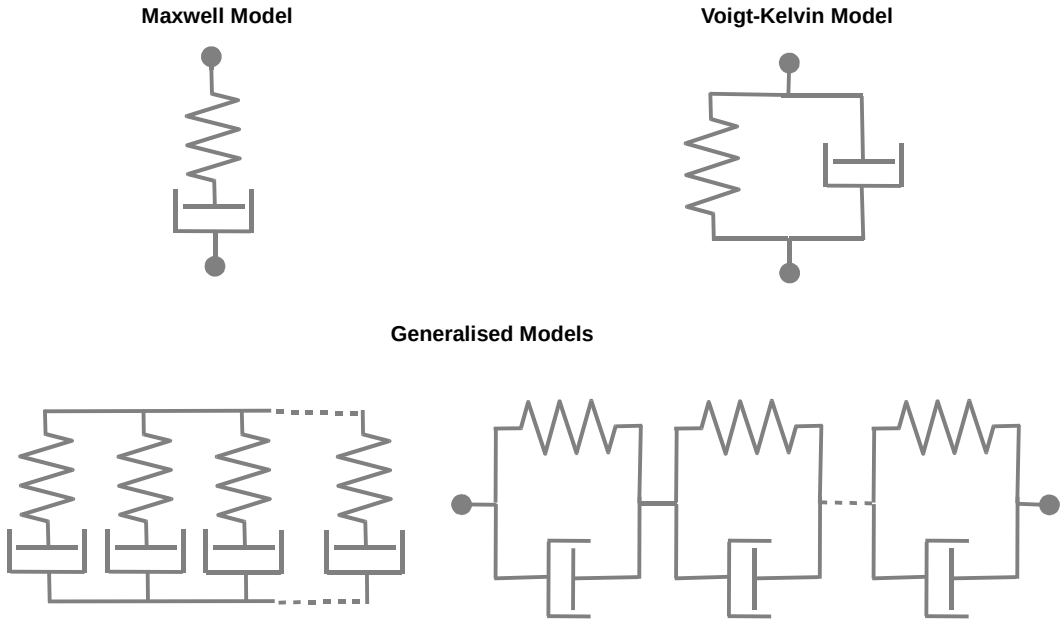

Figure 3.4: Models to describe the linear and viscoelastic deformation by Fink

The introduction of an advanced rubber description allows a variety of predictions of the tyre characteristics.

When viscoelastic materials are deformed periodically, a displacement between stress and strain occurs. The reason is the inner damping of rubber. Determining the modules from the frequency depending quantities, details about the stored respective loss of energy, can be stated. The frequency depending complex elastic modules E can be presented in the complex plane:

$$\underline{E} = E' + i \cdot E''$$ (Equation 3.5)

with: E = complex modulus of elasticity.

E' = dynamic modulus, also called storage modulus. This quantity shows the recoverable energy for vibration processes.

E'' = modulus of loss which gives information of the not recoverable energy.

Corresponding to the elastic modulus, the complex shear modulus is:

$$\underline{G} = G' + i \cdot G''$$ (Equation 3.6)

To evaluate the loss in energy for vibration processes, the dissipation factor tanδ can be defined:

$$\tan\delta = \frac{E''}{E'} \qquad \text{(Equation 3.7)}$$

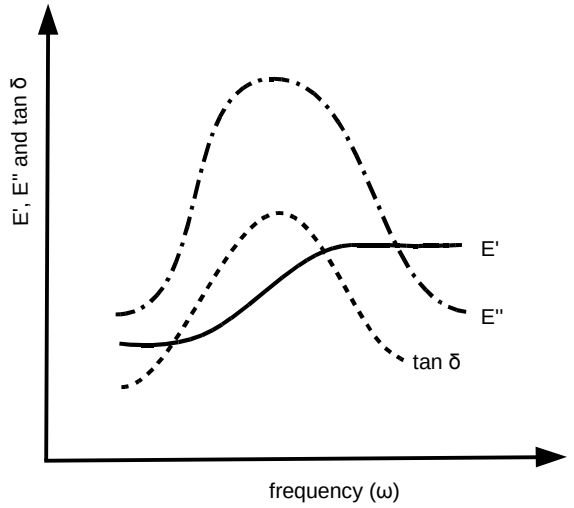

Figure 3.5: The dynamic modulus E', the modulus of loss E'' and the dissipation factor tanδ as a function of the frequency ω [59]

Then for the frequency-dependent strain curve following context results:

$$\sigma(t) = \varepsilon_{max} \cdot (E' \cdot \sin(\omega t) + E'' \cdot \cos(\omega t)) \qquad \text{(Equation 3.8)}$$

The first part of the equation is the elastic restoring force after Fink, while the second part is the phase shifted inner hysteresis. The phase shift is π/2. The shown relationship for the time and frequency response is only valid for constant temperatures. An equal formula expression for the temperature and frequency of viscoelastic materials is made by Williams, Landel and Ferry (WLF) [60]:

$$\log a_T = \frac{-8.86 \cdot (T - T_S)}{(101.6 + (T - T_s))} \qquad \text{(Equation 3.9)}$$

using: $\log a_T$ = Shifting factor

T_S = Reference temperature, usually adding 50°C to the glass-liquid transition

This equation quotes the shifting value for the measured curves at constant temperature along the logarithmic frequency axis, when the experimental temperature is changed.

Components of rubber friction:

The frictional force of rubber is the sum of single components which do not have to appear at the same time. In general it is expressed as:

$$F = F_{Adhesion} + F_{Hysteresis} + F_{Cohesion} + F_{Viscous} \quad \text{(Equation 3.10)}$$

The interrelation of the single components is described as follows:

- The molecular force of attraction ascribes the adhesion component which is in most cases the main portion of the frictional force. The appearance of liquid decreases the ratio.
- For rough surfaces, inner damping losses arise because of the deformation. This is the hysteresis component. The amount depends on the geometry of the surface, the viscoelastic properties of the rubber and the velocity. The ratio is the same for dry and wet surfaces.
- The viscous ratio occurs only for wet surfaces. It is caused by the shearing of a closed viscous liquid layer which is between the surface and the rubber. If the rubber floats, e.g. aqua planing, only viscous friction exists.
- Cohesion is the energy for creating new surfaces, e.g. cracks and wear. The amount of cohesion depends on the temperature and surface characteristic of the frictional partners. In most cases cohesion is negligible.

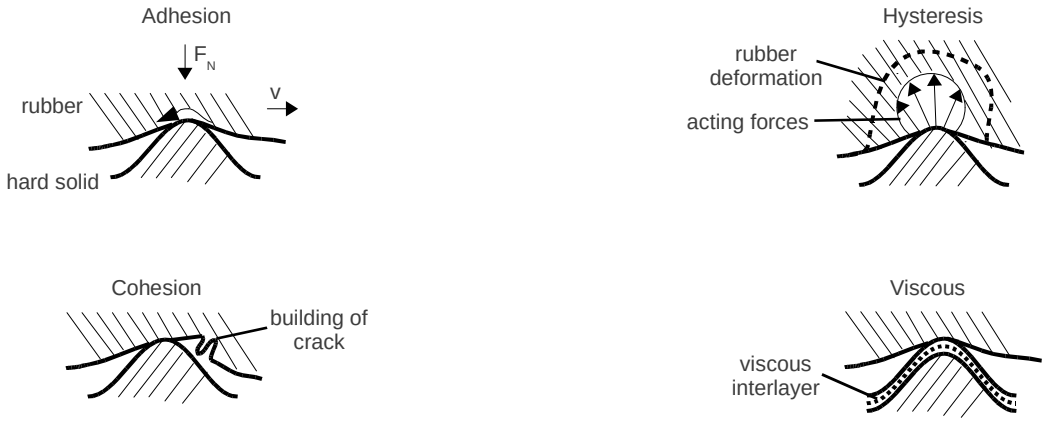

Figure 3.6: Components of rubber friction [61]

Fundamental for the friction between tyre and road are adhesion and hysteresis which are explained in more detail below.

Adhesion:

Adhesion is the connection of the molecular chain of the rubber with the atoms of the friction surface. If the rubber is moving, the chain is stretched and some of the existing connections are torn apart. After tearing the connection, the molecular chain is pulled until the process is repeated by building a new connection. Whenever the molecular chain is moved, energy is needed and the periodical strain and stress leads to damping losses.

The following quantitative statements can be made:

The adhesion coefficient is inversely proportional to the stress.

The adhesion coefficient is proportional to:

- The number of molecular connections.
- The force which is needed to tear a connection.
- The damping characteristic of the rubber, expressed by the complex modulus of loss.

The adhesion depends on the velocity and temperature. This can be explained with the modulus of loss. The coefficient of adhesion is small for low sliding velocities, because the modulus of loss is also small in this case. The adhesion maximum correlates with the frequency, where the modulus of loss has its maximum. The behaviour of the adhesion connection is represented in mechanical models using spring/damper systems.

Hysteresis:

Hysteresis is the deformation of the rubber element caused by sliding the rubber block over a rough surface. The viscous component of the rubber material transfers the deformation energy into heating. For low velocities, the pressure distribution is symmetric while it is asymmetric for higher velocities. This means the relaxation of rubber depends on the velocity and therefore, also on the pressure distribution. The hysteresis coefficient is proportional to:

- The number of obstacles.
- The stress.
- The geometrical roughness of the surface or slope of roughness to the frequency.
- The modulus of loss for the rubber.

For low velocities the hysteresis coefficient is constant. The maximum is reached for high velocities over 160 km/h. The hysteresis coefficient depends on the velocity in the same way as the loss of energy tanδ to the frequency and temperature.

3.1.3 Tyres

In 1845 Robert William Thomson was awarded the British patent on an elastic pneumatic tyre made of rubber texture and leather. The patent was forgotten and in 1888 John Boyd Dunlop got a patent on a pneumatic tyre only in England, as the idea was previously known. At this time, the bicycle was developed using iron wheels in the beginning. The iron wheels were changed to more comfortable solid rubber tyres which frequently came off the rim. The pneumatic tyre was a significant development in comfort and reduced the rolling resistance. Based on the experience

gained with the pneumatic tyre for bicycles, tyre manufacturers developed tyres with significantly higher demands for automobiles. Thereby, Dunlop and Thomson were benefiting from the American chemist Charles Goodyear's invention of the vulcanisation of caoutchouc using sulphur in 1839.

The development of the pneumatic tyre to the state-of-the-art was influenced by the material, structure and the diameter. The essential step in the development was the introduction of the radial tyre in 1948 by Michelin with following advantages:

- Extended durability
- Reduced rolling resistance
- Increased traction
- Improved handling

Nowadays the radial tyre is standard for passenger cars, while the use for lorries is progressing quickly. Presently the bias ply tyre is rarely used any more in industrial nations. This is also the reason why the bias ply tyre is not explained in this dissertation.

Tyre design:

Figure 3.7 shows schematically the cross section of a radial tyre.

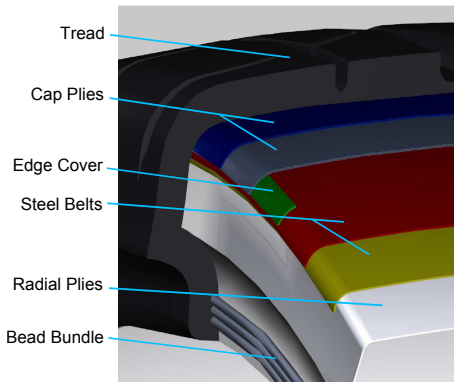

Figure 3.7: Radial tyre cross-section

The tyre is a complex composite body made of materials with different physical properties. The radial tyre consists of the following main components:

- Tyre bead
- Carcass
- Tyre belt
- Tread

The tyre bead ensures a tight fit of the tyre on the rim. This is achieved by individual bronze plated bead wires which are rubber coated and then wound into a bundle. Also the tyre bead ensures the sealing of the entrapped air from the environment for tubeless tyres.

The reinforcement material for the tyre is called carcass. It consists of one or more fabric layers which are hooked at the core and is the predominant load composite. The materials provide the strength and stability to the sidewall and tread.

The cords of the two steel belts are applied at opposite angles to stabilize the tread area and provide impact resistance. The vehicle handling characteristics is affected by the belt width and angle.

The cap plies are used for higher speed rated tyres, consisting of nylon, to restrict expansion from centrifugal forces during high speed operation.

The radial plies, also called body plies, consisting of cord and rubber skim is wrapped around the bead wire bundle, passed radially across the tire and wrapped around the bead bundle on the opposite side. It provides the strength to contain the air pressure and sidewall impact resistance.

The tread surrounds the carcass and transmits the forces between the vehicle and the road. The rubber mixture and the profile of the tread are designed to provide a balance between wear, traction, handling and rolling resistance. The profile can be designed very differently and depends mainly on the intended use. The pattern is molded into the tread during vulcanization or curing and is designed to provide uniform wear, minimize pattern noise on different road surfaces, and to

channel water out of the footprint.

The sidewalls are abrasion resistant, protect the fabric layers from external influences like impacts and flex fatigue. The rubber compound resists cracking due to environmental hazards such as oxygen, UV radiation, ozone and heat [62].

Tyre requirements:

As the tyre is the only link between the road and the vehicle, it transfers all the forces and moments. The transfer behaviour influences the handling, comfort and safety. Thus, the dynamic characteristics of a vehicle are strongly influenced by the tyre behaviour. Therefore, the following parameters have a major impact on the design:

- Wheel load
- Damping
- Suspension
- Axle kinematics
- Engine power
- Maximum speed
- Type of application

A gas or gas mixture is entrapped under high pressure in the pneumatic tyre. The casing determines by the shape, the structural design and the used materials the performance characteristic of the tyre. The requirements of the automotive industry, the consumer and the legislative authority are usually not in context. This leads to conflicting development aims for the tyre manufacturers which need to be solved. Therefore, tyres on the market are a balanced compromise which is reasonable in all aspects of driving safety, driving comfort, handling and efficiency with an increased demand for environmental protection. The development is influenced by the increasing requirements. The increase of the requirements can be demonstrated by the

criteria which need to be fulfilled for the technical approval. In 1960 there were 10 criteria which were tested on a vehicle or a test rig. Today, the guidelines have over 40 criteria. An overview is shown in Table 3.1.

Travelling Comfort	**Transmission of power**	**Durability**
Suspension quality	Traction	Puncture strength
Noise quality	Braking distance	High speed ability
Smoothness of running	Aquaplaning	Structural durability
Stability	**Steering behaviour**	**Efficiency/Environment**
Cornering stability	Steering precision	Rolling resistance
Braking during cornering	for 0°	Pass by noise
Straight ahead stability	at the limit	Retread capability

Table 3.1: Overview of tyre evaluation criteria.

The economic efficiency is more characterised when the tyre is operating on the vehicle than by the production. The rolling resistance of the tyre needs to be overcome by the engine work. Less rolling resistance of the tyre, means lower fuel consumption. Reducing the rolling resistance by 30% means a decrease of the fuel consumption by 4.8%. This correlates up to 60 litres of savings for each tyre during the tyre life time. For Germany, a reduction of the rolling resistance by 30% would save up to 2.5 billion litre of petrol.

Retreaded tyres have a 10% higher rolling resistance compared to new tyres. Therefore, the energy balance for retreaded tyres needs to be discussed.

Legal requirements:

The legal requirements for tyres are marks and the approval number. The tyres have a circled 'E' and the number of the legalizing country. The 'E' indicates that the tyre is certified by the requirements of United Nations Economic Commission for Europe (UNECE) regulation 30 A. The standardization is done by the European Tyre and Rim Technical Organisation (ETRTO) [63].

The mark for example 205/65 R20 90H means:

- 205 Tyre width in millimetre in unloaded condition.
- 65 The ratio between tyre wall and tyre width in percent. In this example, the tyre wall is 133 mm (= 205 x 65%).
- R Indicates the radial design. D is the indication for the bias ply tyre.
- 20 The required rim diameter. In this case 20 inch.
- 90 Is the maximum standard load. In this example 600 kg.
- H Is the speed rating. In this example the maximum speed is 210 km/h.

Further marks are 'TUBELESS' and 'DOT' with the production code. The number 1605 is indicating, that the tyre was produced in the 16th week of 2005.

In the European Union, tyres have to be sold with a label since November 2012. The label is used to increase the safety, economic and environmental efficiency of road transport. Specified are the tyre properties rolling resistance, wet grip and the noise classification. For the first two properties the classes A to G are existing. The noise is categorised into three classes sound wave symbols with the absolute value in decibel. It is defined by the by pass noise at 80 km/h. The rolling resistance has a direct influence on the fuel consumption of a vehicle. A set of class 'A' tyres compared to class 'G' can reduce the fuel consumption by 7.5%. The wet grip is defined by the absolute stopping distance [64].

Force transmission between tyre and road:

The tyre has to ensure the transmission of all forces on different road surfaces, e.g. asphalt, concrete or cobblestones in all weather conditions and velocities of the car. This means the force transmission is a key aspect for the tyre development. The force transmission is influenced by the tyre type, the tyre condition, the road type and the road condition.

The structural behaviour of an ideal membrane is described by the internal pressure p times the contact area A. Due to the stiff shell structure of the tyre, a structural portion k of 10 – 15% is added. For the chassis design the vertical and radial stiffness is an important parameter. The stiffness is increasing with increasing tyre width and decreasing aspect ratio.

The traction of tyres is mainly determined by the frictional partners rubber and road surface, but the coefficient of friction is not constant. It depends on following properties:

- The tread compound.
- The road surface roughness.
- The contact pressure.
- The sliding velocity.
- The temperature.

In general, a lower contact pressure and a homogeneous pressure distribution in the tread area, means a higher traction of longitudinal and transverse force. For higher slip and sliding velocities, the traction decreases.

Depending on the application of the tyre, the rubber compound develops the highest friction at different temperatures. Operating the tyre not in the intended temperature range results in lower friction. Thus, winter tyres usually have a temperature range between -20 and 10°C, while summer tyres are designed for temperatures between 5 and 40°C. In this range, the tyres can achieve the maximum traction. The adhesion is dominant for low sliding and the hysteresis for high sliding velocities. High sliding velocities occur during locked braking.

As explained before, rubber is a viscoelastic material and is characterised using the complex modulus with the dissipation factor tanδ. In tyre development, the temperature-frequency dependence after WLF is used to characterise a tyre. Low fuel consumption requires small rolling resistance and therefore a small tanδ. But having short brake distances, tanδ needs to be big. To achieve this, a mixture of silicate is used.

Tyre models:

Tyre models are used to represent qualitatively or quantitatively the tyre performance. Depending on the requirements, they have different complexity, starting with simple mathematical expressions to detailed dynamic finite element models (FEM). An example is a simple multi body system, consisting of springs, dampers and masses. In Figure 3.8 the FTire model is shown schematically. The required tyre parameters can be gained using extra experimental data. The tyre models can give the information to an attached vehicle model. The linking of tyre models to a complete system has benefits in the development in terms of a better matching to ABS and ESC braking systems. Thus, shorter braking distances are possible.

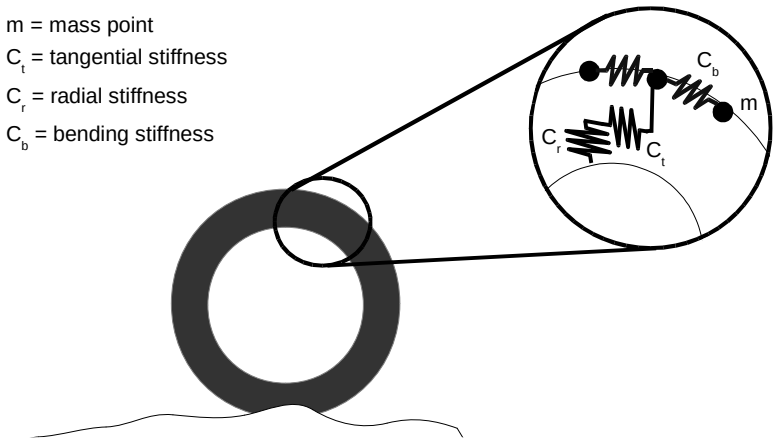

Figure 3.8: A simple multi body tyre model [65]

3.2 Current research projects

3.2.1 The APOLLO project

To develop a tyre of the future for intelligent vehicle technology, driver support and external users, a project called APOLLO, funded by the European Commission was launched in 2002. The consortium consisted of the RWTH University Aachen, Helsinki University of Technology and Technical Research Centre of Finland (VTT), the tyre manufacturers Nokian Tyres plc and Pirelli, the vehicle manufacturer Daimler Chrysler AG and the vehicle electronics manufacturer Magneti Marelli.

The aim of the APOLLO project was the development of an intelligent tyre for improving road traffic safety. The objectives were:

Designing a prototype of a mechatronic tyre system, called 'Intelligent Tyre'.

Building a demonstrator of the system which is capable of providing the required signals, e.g. tyre-road contact. This information can be used to improve automotive safety systems.

A system for the communication between the tyre to the vehicle was realised, the power generation and a sensor to monitor the tyre-road contact. The objective of the mechatronic tyre prototype are the provision of various parameter information for the tyre-road contact as:

- Exerted forces on the tyre.
- Present slip information.
- The available friction potential.
- Tread wear.
- The road surface roughness.
- Prediction of potential tyre damage.

The power supply can be achieved using two different methods. The inductive generation is found as feasible. Using piezo effects, only a little amount of power can be generated. The area of contact is detected using acceleration sensors. For the data transmission short range devices with a frequency of about 433 MHz were used [66].

3.2.2 The FRICTION project

A further program called FRICTION was lunched under the Sixth Framework Programme of the European Union to continue the APOLLO project. The project finished in 2009 with following points from the final report:

The road conditions are detected by the driver and she/he learns the estimation of the maximum tyre-road friction. Most state-of-the-art vehicle systems cannot detect the maximum of the available friction till the vehicle begins to slip. Friction has an important part during driving, because all forces which are acting on the vehicle are transferred via the friction forces between the tyre and the road surface. Drivers often fail to estimate the available friction correctly and perform not possible manoeuvres in terms of vehicle dynamics. The result is losing the control over the vehicle. The percentage of speed-related accidents was 31% which are caused by misjudgement in 64% of all cases. The numbers are for London women in 2007 [67]. The driver behaviour, the alertness and the friction are the remaining unknown key parameters of future ADAS for calculating the risk of a collision, or a safe cruising speed. As an example, the collision mitigation system assumes the availability of high friction, so it will have poor performance on snow, since the brakes are triggered too late.

During the project the main tasks were the development, demonstration and verification of a system to provide continuous information of the available friction for vehicle manoeuvres. The goal is to offer new information for vehicle safety systems to enable a more accurate, especially in unusual road conditions operation. The main focus was the detection of the available friction on paved roads, e.g. asphalt and concrete conditions. The conditions are studied for dry, wet, snowy and icy surfaces.

The sensor information is crucial for the friction estimation. Due to cost reasons the project emphases the utilisation of existing or planned sensors in a novel way. The utilised sensors can be of the following type:

chassis: wheel velocities, xyz acceleration, yaw rate, pitch, roll, steering wheel angle and steering torque.

environmental: xy ground velocity, laser spectroscopy, laser scanner, air and road temperature, radar, camera.

tyre: From the previous APOLLO project, a tyre deformation sensor.

The system can also handle missing, e.g. defect or not existing sensors. In the case of a sensor getting damaged, the whole FRICTION system does not stop working. Hence, the friction estimation accuracy will decrease. If the vehicle is equipped with only one subset of possible sensors, e.g. implementing a low cost system, the accuracy is decreasing.

The objectives of FRICTION project are shown in the following:

- The creation of a model for on-board tyre-road friction estimation.
- Design of a prototype system using a minimum number of sensors.
- Verification of the system advantages in selected vehicles.

The FRICTION system offers two values: called 'Friction Used' and 'Friction Potential'. 'Friction Used' gives the information how much friction a driving manoeuvre requires. While 'Friction Potential' gives the maximum available friction which the tyres can achieve on the present road pavement. These information are equipped with an error estimation.

The FRICTION system also provides an estimation of wheel slip, as well as road and weather condition: dry, wet, snowy and icy. When tyre sensors are available, additional information about the tyre forces are provided. The detection of aquaplaning is possible at early stages as well.

The main results of FRICTION were:

- The friction potential is estimated for changing road conditions, using sensor clusters and learning features. The data are checked on plausibility in different conditions.
- During the project new sensing technology for classification of road conditions, especially for detecting ice, snow and water was developed. The sensor system includes a polarization camera system, new features for radar devises, a laser-scanner to detect weather, and improvements for road eye sensors.
- The benefit of friction estimation was demonstrated on collision mitigation systems and driver warning including human machine interface (HMI) considerations.
- The state-of-the-art tyre sensor from APOLLO project was further developed.
- The benefits of the friction estimation were tested using a collision mitigation system prototype from the PreVENT IP - APALACI subproject. Thereby, the period between the driver warning and brake activation were compared with and without friction information. The tests confirmed a further reduction of the crash impact.
- For collision mitigation manoeuvres, the FRICTION system can provide an initial estimation of the current friction potential. This can be applied for ABS and TCS to improve the system.
- Finally, it is stated that the full FRICTION system can detect friction during the studied conditions as well as an alert human driver [68].

Chapter FOUR

Chapter four describes the concept of a novel safety system based on a double chamber rim. Thus, the history of rim development is described alongside different production methods to show the feasibility of the system. Additionally, the wireless communication between the sensor system which is fitted to the car and the actuator in the rim is exemplified.

4. Design of the novel safety system

4.1 Concept of the safety system

The aim of the safety system is to reduce the collision speed and therefore to reduce the crash impact. As shown in the previous chapter, a relatively small reduction of the vehicle speed before a collision can greatly reduce the number and the extent of the passenger injuries and also of other motorists and pedestrians. The underlying idea is an increase of the contact area between tyre and road surface in order to increase friction. A higher friction helps to decelerate the vehicle. The present system refers to cars, but can be applied to other vehicles such as trucks, buses, or aeroplanes. The control concept is shown in Figure 4.1. An optical sensor monitors continuously the vehicle environment in the direction of travel. If a potential obstacle is detected, a signal is transmitted to the electronic control unit. Based on the vehicle speed and the measured distance to the obstacle, the control algorithm decides whether a collision is inevitable. In case of an inevitable collision situation, a radio signal is generated to open the low pressure chamber of the wheel. The low pressure chamber is located in the rim of the vehicle. Opening the low pressure chamber lowers the inflation pressure of the wheel as both chambers are linked. Therefore, the tyre footprint is increased.

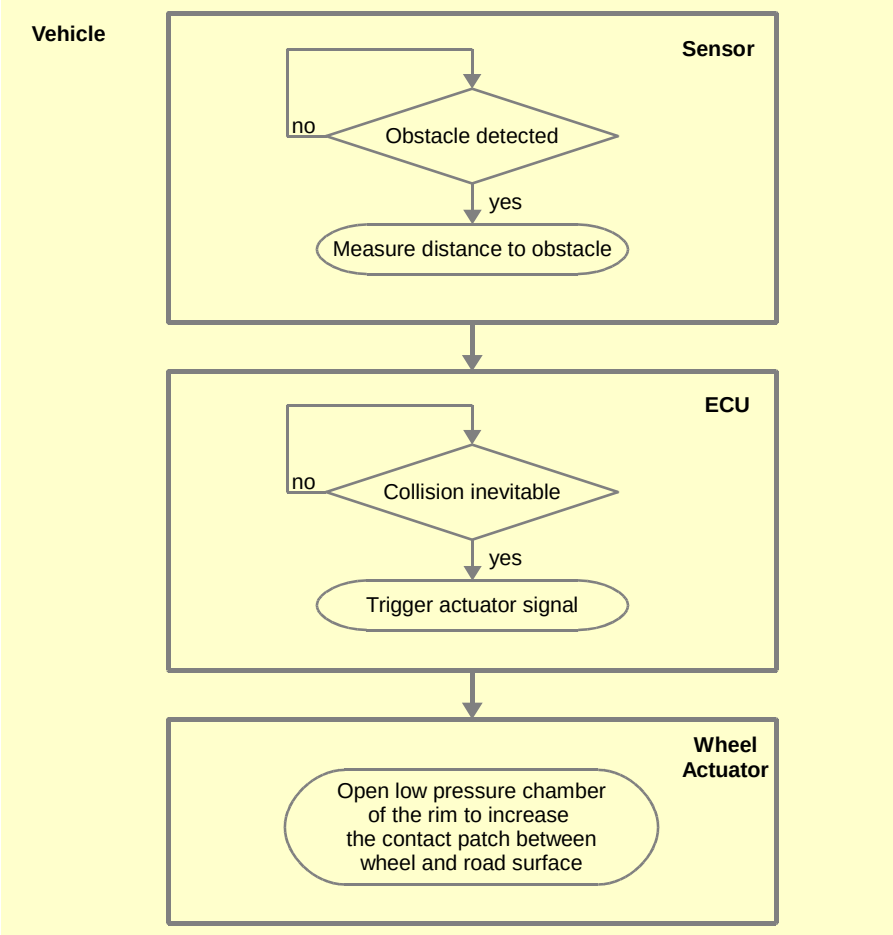

Figure 4.1: Functional diagram of the control system

4.2 Feasibility of the system

The wheel is one of the most important inventions in the history of humankind. In nature, no examples are existing. It is the result of drums to move heavy goods for the construction of exceptional buildings, e.g. the pyramids. Around 4000 BC, the connection of wooden circular discs with an axis is confirmed. Around 3000 BC, the first advanced civilization, the Sumerian, had vehicles with four wheels in operation. First wheels with spokes are dated to 2000 BC. The spoked wheel was in use without major modification until the pneumatic tyre was officially invented in 1888. Today, wheels are mainly produced from steel and aluminium. The design is finally determined by the load, the vehicle dynamics, the aesthetic and the costs. The demand to reduce

environmental pollution leads to light weight constructions. The European standard of wheels is regulated in the ETRTO, defining size and the rim profile. Depending on the tyre in use, different profiles are applied. The interface to the vehicle is designed very independently and is specified by the car manufacturer like the:

- Clearance of the brakes
- Wheel offset
- Bolt circle
- Hub bore hole

All other aspects are designed according stylistic guidelines:

- The wheel disc
- The outside of the rim
- The rim contour

The manufacturing process is classified in three main groups:

- Casting
  - Aluminium and magnesium wheel
    - Low pressure casting

      This process uses a steel die, arranged above the crucible and filled with molten magnesium. Usually, the crucible is sealed against the die. To force the molten metal into the die, pressurized air is used. Low pressure casting wheels have a high ductility.

- High pressure die casting

  For this process, machines with a high closing force are used to clamp the die. The molten magnesium is poured in a shot sleeve. The metal is pushed into the die with high speed and pressure by the push of a piston. The magnesium solidifies and the die can be opened. Wheels manufactured with this method are low-priced and have a high corrosion resistance. Disadvantages are a reduced ductility and a lower strength.

- Gravity casting

  Since the early 1920s, gravity cast magnesium wheels have been produced. The advantage of this method is a good ductility and the cost of the required tools is low. This allows a flexibility in design and a short development time with the option of small batch production.

- Drop forging
  - Aluminium and magnesium wheel

    In this process, the workpiece is placed into the forge. The material is heated to make it malleable with the impact of a forming force.

- Metal forming, embossing and milling
  - Steel wheel, aluminium alloy wheel

To design a wheel, CAD tools are used to create the 3D geometry, the 2D drawing, the surface and the solids. This information is needed for the material strength analysis, test protocols, programming of the production machines, forming and casting simulations. It is also used for manufacturing the lasting mould, the forging mould and clamping devices.

FEM offers the simulation of multi axial loads on the wheel. This allows reasonable predictions of failure probability. Required is an extensive data base and the deduced material fatigue curves for the used material and the manufacturing process. Thus, the maximum allowed (equivalent) stresses can be determined. Different standardized tests help to prove the durability and crash safety.

The rotating bending test allows to check the operating stability of wheels. The outside wheel experiences a higher load, due to the lateral force during cornering. The force generates two bending moments in the wheel which are determined by the dynamic radius r_{dyn} and the offset e as crank of lever. The test load is twice the maximum wheel load which means a lifting of the inside wheel. The gained bending moment is used to prove the endurance strength for the rotating bending test.

The dynamic radial load testing is like the rotating bending test used to check the fatigue strength. Usually this test is performed under constant radial load. The load is the maximum wheel load times 2.5. However, some automotive manufacturers require an additional lateral force component which is generated by a steering angle.

As the rotating bending test and the peel test cannot reproduce all stresses of the wheel during operation completely. Cracks cannot be precluded as it happened in the past after long time of use. Therefore, the biaxial wheel test bench was invented to confirm the operating stability of new wheels. The performance of new materials and new production processes is tested. The load conditions for the wheel contact and the lateral forces are recorded on road tests, and then adapted to the test bench. The wheel is fitted with tyres and is stressed with continuous changing dynamic loads. The control algorithm is simulating the load characteristic of the recorded track realistically.

The impact test according to SAE J175 [69] is simulating a side impact of a kerb. In the test the tyred wheel is exposed with a high dynamic load caused by a falling weight. The impact should not lead to fractures or a sudden loss of air.

The corrosion test in artificial atmospheres is specified in the ISO 9227 [70]. It is also called the salt spray test to prove the corrosion resistance of metallic materials. The surface is partly damaged and sprayed with a saline solution.

Hence, the required parameters for the tests are:

- Vehicle mass and the resulting wheel load
- Dynamic rolling diameter
- Cornering forces
- Accelerating and braking torque
- Coefficient of impact, caused by potholes, bumps or kerbs
- Surface requirements
- Thermal stress
- Material properties

The steel disk wheel is still the standard equipment for low class vehicles and almost exclusive for lorries. The main advantage of the steel disc wheel is the low manufacturing costs, but only when it is produced in mass production. This is due to the high initial investment for the production facilities and the required tools. Currently, it is manufactured from high tensile steel. It consists of two parts, the rim and the wheel disc which are welded. Recent developments allow for a variable distribution of the used material related to the occurring stress. This helps to save weight. The parts of the rim shoulder are thinned due to the applied lower load. The face of the disc wheel is improved because of the aesthetic appeal and to enhance the brake cooling, so the classic spoke approach was applied. But the production process is difficult, due to the complex shape.

The aluminium alloy wheel has a higher load capacity with a reduced weight. As material, refined hypoeutectic $AlSi_7Mg$ or near-eutectic $AlSi_{11}Mg$ is used. The unsprung mass, the inertia and the stiffness have a significant influence on the dynamic behaviour of the vehicle in terms of steering force, steering accuracy and wheel load fluctuation as well as for accelerating and braking. As the the wheel counts to the unsprung masses, a weight reduction has a multiple impact.

The development was originally from very large and slim to wider and smaller wheels. That was caused by improved road surfaces and higher cornering velocities. In the 1970s the trend changed again to bigger wheels for cars, because of aesthetics, vehicle dynamics and bigger brakes.

The combination wheel/tyre has special aspects e.g.:

- Powerful cars can cause a slipping of the tyre on the rim, when a high braking or accelerating torque is applied. To avoid this effect, the surface of the tyre seat is modified, e.g. using a special anti slip coating.
- Road and tyre are initiating high frequency oscillation. This causes a higher wear of the rim flange. Again, this effect can be reduced by using special anti slip coating.
- Low profile tyres causing a higher stress in the rim when potholes, bumps or kerbs are passed. The rim flange can be deformed or get damaged. Buffers made of stainless steel or composite material can help to reduce the damage.
- As the suspension is sensitive, low tolerances for concentric and axial run-out is required. Uneven weight distributions in radial and axial direction are mostly caused by clamping errors or density fluctuations and are the reason for imbalances. Imbalances are more difficult to control for increasing wheel diameters and wheel weights.

To produce one ton of aluminium, about 13 to 18 MWh are needed. This energy is stored in the material and can be recovered to a larger extent. When aluminium is recycled, only 5% of the initial energy is needed, due to the low melting point of 660°C. There are no losses in quality. By recycling, the energy balance can be improved significantly over several cycles.

For producing one ton of steel, approximately 6 – 8 MWh are required. However, steel has a higher energy consumption for recycling due to the high melting point of 1500°C.

4.3 Double chamber rim design

The double chamber rim was designed in a Bachelor project under the supervision of the author [71]. In the project, the wheel size was chosen with a diameter of 18". Due to the double chamber design, the inside of the rim contour is equivalent to a 16" wheel. The shape of the rim contour is defined in the specification DIN 7817 [72]. Only the base of the rim needs to be modified to get a larger volume in the second chamber. The second chamber is designed below this base and the bigger part of the chamber is near the rim outside. The reason is to get a larger rim diameter in the inside to create space for the brake disc. Figure 4.2 shows the cross-section of the rim and Appendix A the design drawing.

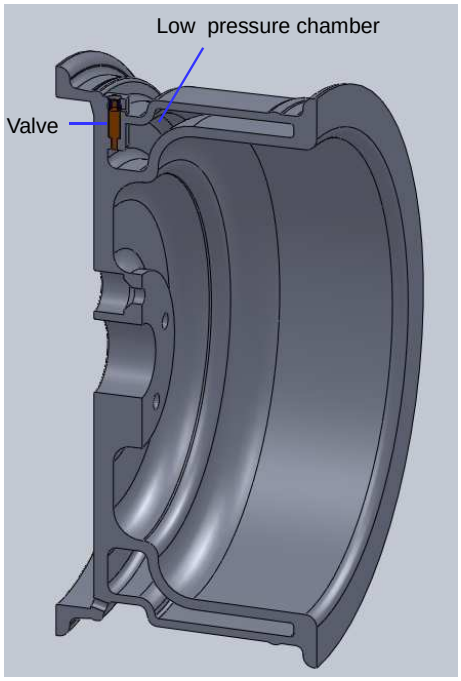

Figure 4.2: Profile of double chamber rim

To use the low pressure in the second chamber, a link to the first chamber is needed. If a larger contact patch is required, the two chambers must be connected quickly and reliably. A possible actuator is a pyrotechnical system, with a predetermined breaking point triggered by a current pulse. Another option is the use of valves. But here, the weight is important, as the actuator is placed in the wheel and an unsymmetrical weight distribution of the wheel can cause imbalances.

Both options have advantages and disadvantages:

- The advantage of the valve is a controllable pressure exchange, with the disadvantages of the valve weight which can cause imbalances and the pressure exchange is limited in time by the diameter of the valve.
- The pressure exchange is not controllable for a pyrotechnical system which is a disadvantage. But therefore, it is not restricted by a diameter.

To illustrate and test the concept, a demonstration system was built. On top of the rim base, an iron sheet was welded using a steel wheel. An electric low pressure valve was used as link between the two chambers, with a switching time of < 10 ms and a mass of 12.5 gram. The flow rate is 90 litres/minute for 8 bar [73].

Pressure exchange between the two chambers:

Using the ideal gas law by Clapeyron [74]:

$$p \cdot V = n \cdot R \cdot T \qquad \text{(Equation 4.1)}$$

with:

- p is the absolute pressure of the gas.
- V is the volume of the gas.
- n is the amount of substances of the gas in mol.
- R is the gas constant.
- T is the absolute temperature of the gas.

The two chambers have the volume V_1 and V_2 with the pressure p_1 and p_2 and the amount of substances n_1 and n_2. The volumes and the pressures are known. The amount of substances can be calculated using Equation 4.1:

$$n_1 = \frac{p_1 \cdot V_1}{R \cdot T} \quad \text{and} \quad n_2 = \frac{p_2 \cdot V_2}{R \cdot T} \qquad \text{(Equation 4.2)}$$

When the actuator is triggered both chambers are linked, the remaining pressure can be calculated:

$$p \cdot (V_1 + V_2) = (n_1 + n_2) \cdot R \cdot T \qquad \text{(Equation 4.3)}$$

Using Equation 4.2 in 4.3:

$$p = \frac{(p_1 \cdot V_1 + p_2 \cdot V_2)}{V_1 + V_2} \qquad \text{(Equation 4.4)}$$

A common gas volume of a tyre is about 11 litre with a normal inflation pressure of 2.2 bar. Assuming the second chamber has a volume of 3 litre with a low pressure of 0.6 bar, the total pressure can be changed from 2.2 bar to 1.7 bar.

Communication between the in-vehicle bus system and the actuator:

To establish a radio connection between the in-vehicle bus system and the actuator of the double chamber wheel, a student project was supervised by the author [75].

The CAN bus is the industrial standard for the cross linking of control systems in vehicles. To activate the valve or the blow out disc, a wireless interface is needed as the wheel is rotating and a wire would tear. As an interface, the ZigBee standard is an option. ZigBee is mainly used in industrial applications and is defined in IEEE 802.15.4 [76]. The standard covers the layers 1 and 2 in the ISO/OSI model [77]. The data rate is up to 250 kbit/s and the frequency is 2.4 GHz. Other frequencies, e.g. 800 MHz, are also possible. The main benefits of the standard are the cost effectiveness compared to others, the short latency period, the increased data integrity and a low current consumption due to a required low data rate and the option of sleep mode operation.

The objective of the student project was the implementation of a sensor/actor network with microcontrollers. To trigger the actuator inside the wheel in an emergency situation, a CAN message is generated which will be processed by a microcontroller. A second controller transmits a wireless ZigBee message to a third controller which is then fitted on the rim. The algorithms are implemented on the Atmega128RFA1 [78] for the ZigBee transmission and to process the CAN message, the AT90CAN128 [79] is used.

For demonstration purposes a model car was controlled by a joystick. The x and y position of the joystick are read by a personal computer. The computer generates a CAN signal using the Vector software tool CANoe which is processed by the AT90CAN128. The AT90CAN128 sends a SPI signal to the ZigBee transmitter, while the ZigBee receiver is mounted on the model car controlling the DC motors for the powertrain and steering, shown in the signal flow chart in Figure 4.3.

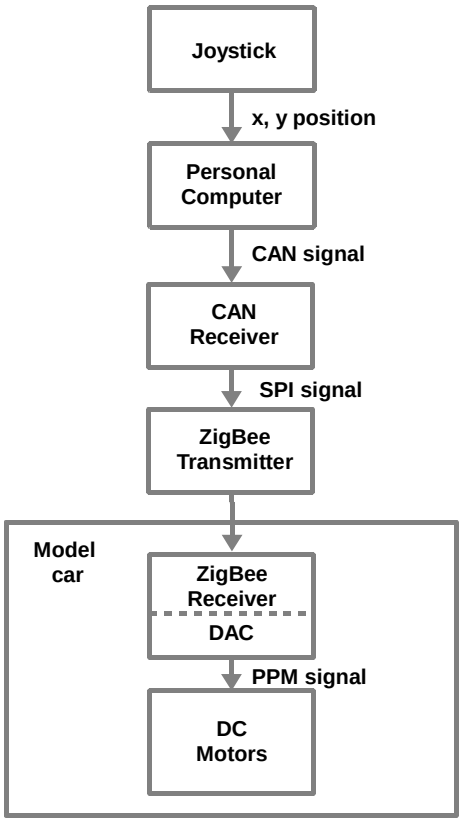

Figure 4.3: Functional diagram of ZigBee project

Chapter FIVE

This chapter presents the experiments that were conducted to investigate the influence of tyre inflation pressure on friction. In the beginning, brake test results are shown using a robot system. The chapter then introduces experimental data, performing extensive brake tests using different car models, provided by Hankook tyres. The chapter concludes with a description of pull tests that were performed using a winch to investigate rubber friction.

5. Experimental results

5.1 Performing brake tests using a robotic approach

In order to investigate the influence of tyre pressure on the braking distance, road tests are carried out. A brake robot is used to achieve scientific test results. The system is designed by Anthony Best Dynamics Ltd. [80] and has a considerably better accuracy and repeatability compared to the results of experienced test drivers. While the system is fitted to the car, the system design allows people to drive the vehicle safely in normal road traffic. The brake robot system can be operated in different control modes:

- Force control: A load cell is measuring the applied pedal force and gives a feedback to the brake robot system.
- Position control: The feedback is either taken from the actuator or from a transducer which is directly connected to the pedal.
- Deceleration control: An accelerometer is measuring the deceleration of the vehicle which is used as the feedback for the control system.

Brake robot hardware and installation

The robot system consists of an electrically driven ball screw actuator. It is positioned in front of the driver's seat between the legs of the driver, as shown in Figure 5.1, as well as in Appendix B. The maximum brake pedal force is 1400 N driven with a maximum velocity of 1600 mm/s, when no load is applied. The velocity depends, for example, on the pedal stiffness, when the brake pedal force is controlled. A dual lever-arm mechanism allows to override the robot system by the driver.

Figure 5.1: Brake robot

Controller inputs and outputs

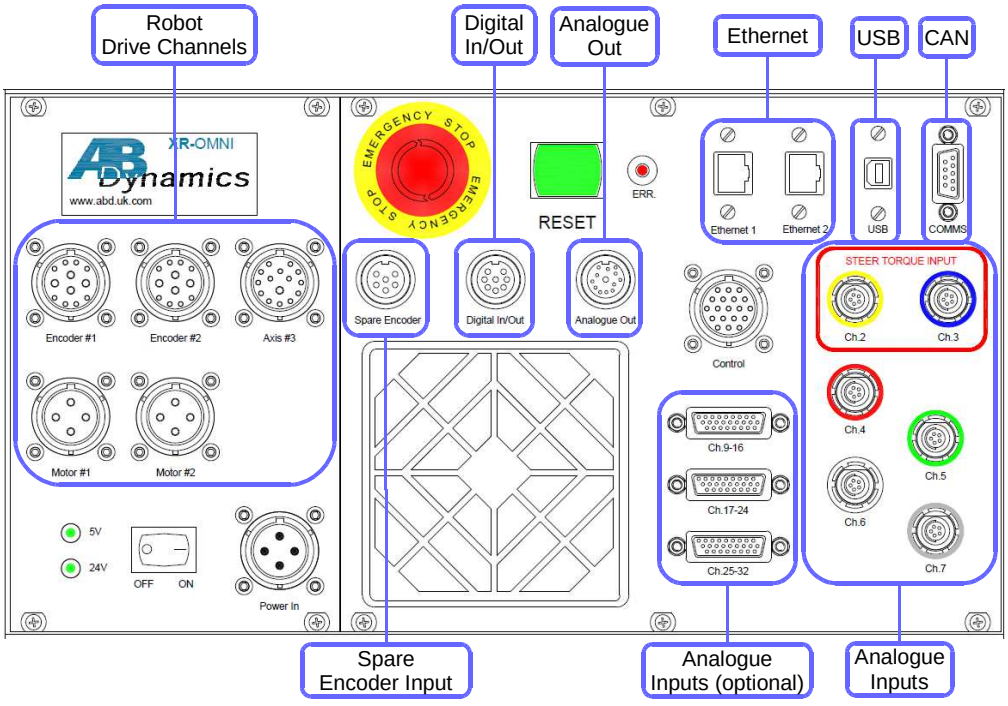

Figure 5.2: Brake robot controller

Analogue outputs:

The controller includes analogue outputs (± 10V, 16 bit). The update frequency for the signals is approximately 1.1 kHz. The brake pedal force is controlled by this output channel.

Digital I/O:

The digital output can be used to start and stop external data acquisition systems.

Analogue inputs:

The controller includes ± 10V analogue inputs. They can be used for data capture, e.g. vehicle speed signal, yaw, or roll rate signal. Optional analogue inputs can be added if required.

Spare encoder input:

The spare encoder-style input can be used for position measurement, e.g. pedal position.

Ethernet connection:

To transfer data from motion measurement packs, e.g. Genesys ADMA [81] or iMar iTrace [82], the ethernet interface can be used.

USB connection:

The measured data are transferred to user interface PC using the USB connection.

Power supply unit:

A photograph of the power supply is shown in Appendix B. The drive voltage of the robot is about 65V in order to produce the full performance. The power supply unit transforms the vehicle's supply voltage of 12V to the required level via DC/DC converter.

Motion measurement

To measure the actual braking distance, the motion measurement system RT3000 from Oxford Technical Solutions has been used. It is an advanced GPS navigation system for measuring motion, position and orientation. It uses an inertial navigation system technology and is combined with survey grade GPS receivers. The position accuracy is up to 2.0 cm and velocity accuracy up to 0.05 km/h [83].

Description of the experiment

For each tyre pressure, at least three test runs are performed. The inflation pressure of all four tyres is changed in steps of 0.2 bar from 2.4 bar to 1.0 bar and the brake pedal force is set to 100 N to avoid triggering the ABS. The tyre surface temperature and inflation pressure is recorded before and after a test run. The car is accelerated up to 100 kph on the runway of the airfield. Now, the system is triggered and the acceleration is stopped. As soon as the car is decelerated to 100 kph because of air resistance and rolling resistance, the brake pedal is pushed by the robot. The brake force is delayed by 0.5 sec after starting the recording.

Evaluation of the experiment

To evaluate the data in Matlab, an m-file is written. Figure 5.3 shows the data for the test run of one typical tyre pressure, in this case 1.4 bar. All results are presented in a bigger format in Appendix C. The three test runs are distinguished by the colours blue, red, and black. The sub-figure top left 'xPostion vs Time' is used to calculate the actual braking distance. The sub-figure top right 'Speed vs Time' shows the decreasing vehicle speed and the slope is for all three test runs almost the same. The sub-figure bottom left 'Acceleration vs Time' illustrates the deceleration of the car and in all three cases the car was braking with 7 m/s^2. The sub-figure bottom right 'Robot Load vs Time' shows the applied load on the brake pedal which was set to 100 N. The brake robot starts to apply the load after 0.5 seconds and it takes an additional second until the full load is reached. The total time until the car velocity is 0 kph is in this case 5.2 seconds.

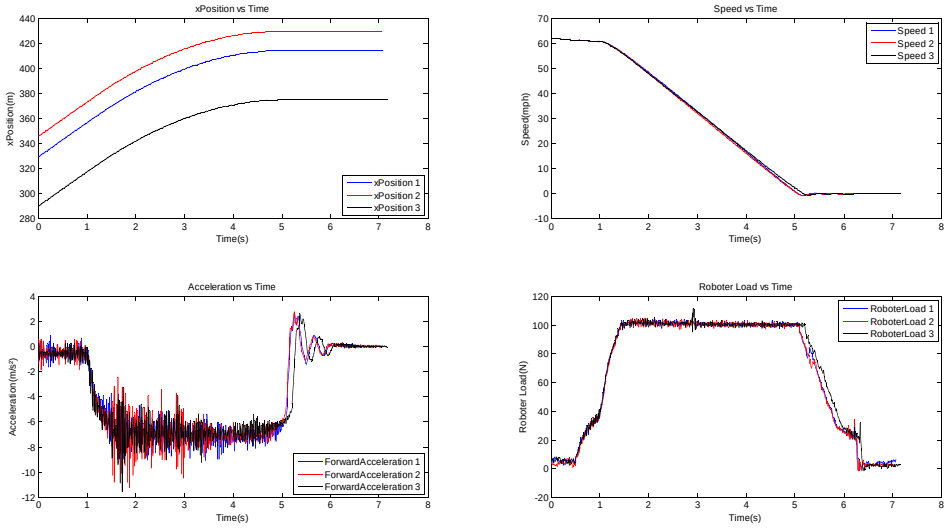

Figure 5.3: Evaluation plot of brake tests also presented in a bigger format in Appendix C

Table 5.1 shows the braking distance depending upon the tyre inflation pressure. Figure 5.4 shows the braking distances gained at different tyre inflation pressures including the corresponding error bars. The standard deviation is largest for the highest inflation pressure. This is maybe due to run in effects of the tyres and the brakes as the experiment started with using an inflation pressure of 2.4 bar.

Number of Run	**1.0 bar**	**1.2 bar**	**1.4 bar**	**1.6 bar**	**1.8 bar**	**2.0 bar**	**2.2 bar**	**2.4 bar**
1	84.4 m	85.7 m	84.9 m	86.7 m	84.1 m	83.4 m	83.6 m	86.9 m
2	82.7 m	85.3 m	84.0 m	86.1 m	83.2 m	83.2 m	82.7 m	85.1 m
3	82.6 m	87.1 m	85.1 m	87.1 m	83.9 m	85.4 m	85.5 m	88.2 m
Average	83.2 m	86.0 m	84.7 m	86.6 m	83.7 m	84.0 m	83.9 m	86.7 m
Standard Deviation	0.8 m	0.8 m	0.5 m	0.4 m	0.4 m	1.0 m	1.2 m	1.3 m

Table 5.1: The braking distance for different the tyre inflation pressures.

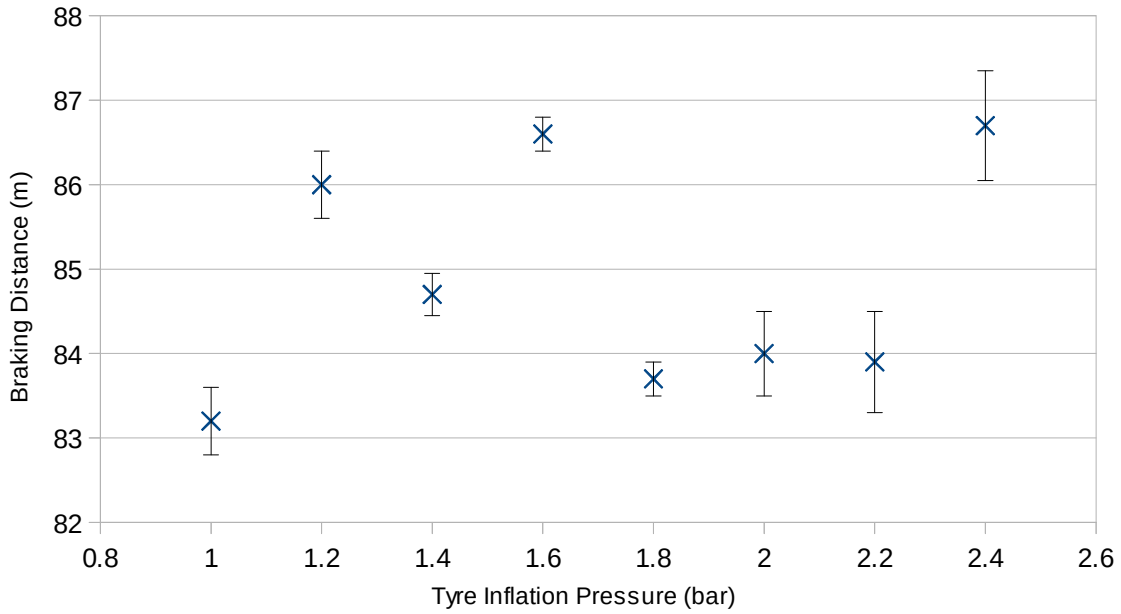

Figure 5.4: The braking distances for different tyre inflation pressures

Measurement of the tyre contact patch

To measure the contact patch of the tyre, a Prescale Film of Fujiflim [84] is used. The Prescale Film can precisely indicate pressure, pressure distribution and pressure balance. The film is capable of measuring extremely low pressures in a range of 0.05 - 0.2 Nmm^{-2} and a resolution of 0.1 mm. The accuracy is between ±10% when measured with densitometer at 23°C at 65% relative humidity. The film consists of two foils. One foil is coated with a layer of micro-encapsulated colour forming material, the second one with a layer of the colour developing material. Figure 5.4 shows the working principle of the Prescale Films. An example of the measurement is presented in Appendix F.

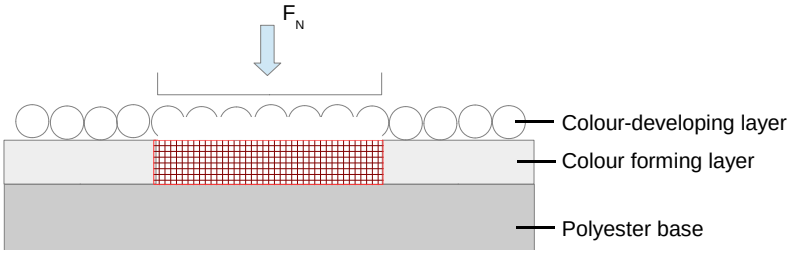

Figure 5.5: Functional principle of Prescale Film

The records of the footprint are analysed with the software tool Pixcavator [85]. The size is defined in pixel. Figure 5.5 displays the growth of the footprint with decreasing tyre pressure. The contact patch size is roughly constant between 1.8 and 2.2 bar which is also the recommended tyre inflation pressure. Otherwise, the graph is approximately linear.

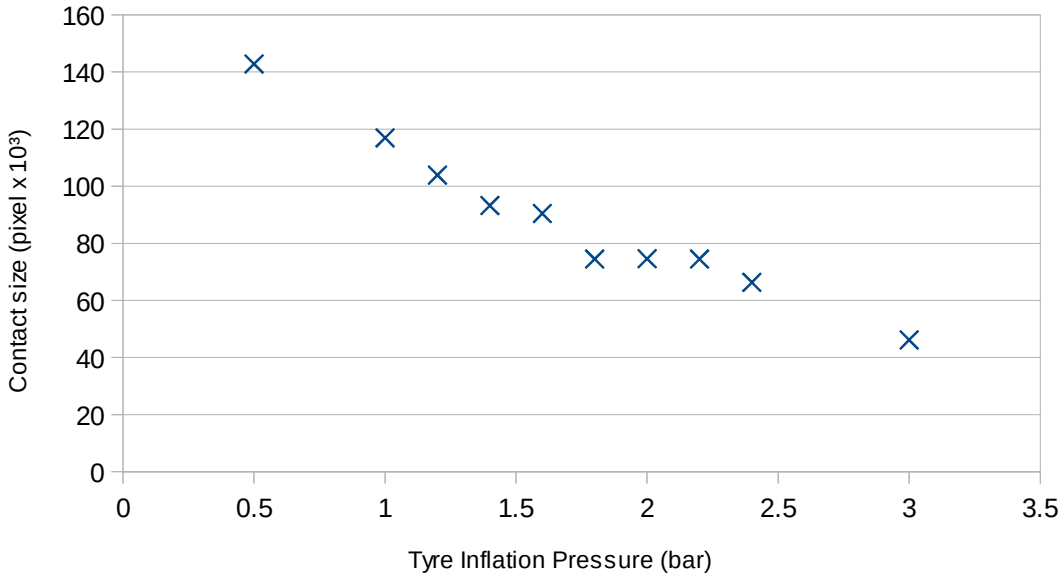

Figure 5.6: The tyre tread pattern according to the inflation pressure

5.2 Hankook's brake test results

Hankook used three different cars for the tests, a KIA Lotze, a Hyundai Avante HD and a Volkswagen Golf [86]. The tyre inflation pressure was set to 2.2 bar and 1.5 bar using winter and summer tyres. To avoid run-in effects, for each tyre pressure new, identical tyres with the same compound, produced by the same operator were used. So, in total, 12 sets of new tyres were used for the tests. The vehicles were operated by experienced test drivers and accelerated to 100 kph. In these tests, ABS was triggered. The results for the braking distances are presented in Table 5.2, 5.3 and 5.4 as well as in Figure 5.7, 5.8 and 5.9.

Number of Braking	Summer Tyres (2.2 bar)	Summer Tyres (1.5 bar)	Winter Tyres (2.2 bar)	Winter Tyres (1.5 bar)
1	39.9 m	39.0 m	44.7 m	44.8 m
2	39.9 m	38.7 m	44.9 m	44.2 m
3	40.6 m	39.0 m	45.2 m	44.0 m
4	39.5 m	38.6 m	46.6 m	43.2 m
5	39.5 m	38.6 m	45.3 m	43.3 m
6	39.8 m	38.1 m	45.0 m	42.8 m
Average	39.9 m	38.7 m	45.3 m	43.7 m
Standard Deviation	0.4 m	0.3 m	0.6 m	0.7 m

Table 5.2: The braking distance for different tyre inflation pressures using KIA Lotze.

Number of Braking	Summer Tyres (2.2 bar)	Summer Tyres (1.5 bar)	Winter Tyres (2.2 bar)	Winter Tyres (1.5 bar)
1	40.3 m	40.8 m	47.1 m	47.6 m
2	41.5 m	40.6 m	46.2 m	47.0 m
3	40.8 m	39.4 m	47.2 m	46.1 m
4	40.7 m	39.5 m	46.5 m	45.6 m
5	41.5 m	40.2 m	46.3 m	45.0 m
6	40.4 m	39.8 m	46.1 m	44.5 m
Average	40.9 m	40.1 m	46.6 m	46.0 m
Standard Deviation	0.5 m	0.5 m	0.4 m	1.1 m

Table 5.3: The braking distance for different tyre inflation pressures using Hyundai Avante HD.

Number of Braking	Summer Tyres (2.2 bar)	Summer Tyres (1.5 bar)	Winter Tyres (2.2 bar)	Winter Tyres (1.5 bar)
1	39.7 m	39.3 m	46.2 m	44.0 m
2	39.9 m	38.7 m	46.5 m	44.2 m
3	40.1 m	38.9 m	46.1 m	43.1 m
4	39.4 m	39.1 m	45.8 m	43.1 m
5	39.7 m	38.9 m	44.5 m	42.9 m
6	39.8 m	39.5 m	44.2 m	42.9 m
Average	39.8 m	39.1 m	45.6 m	43.4 m
Standard Deviation	0.2 m	0.3 m	0.9 m	0.5 m

Table 5.4: The braking distance for different tyre inflation pressures using Volkswagen Golf.

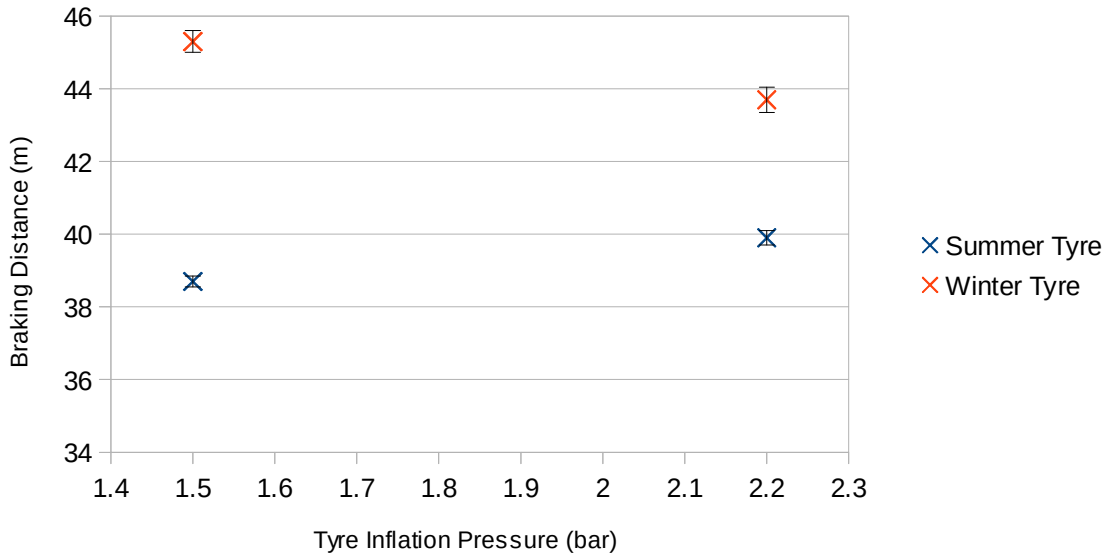

Figure 5.7: Braking distance for different tyre inflation pressures using KIA Lotze

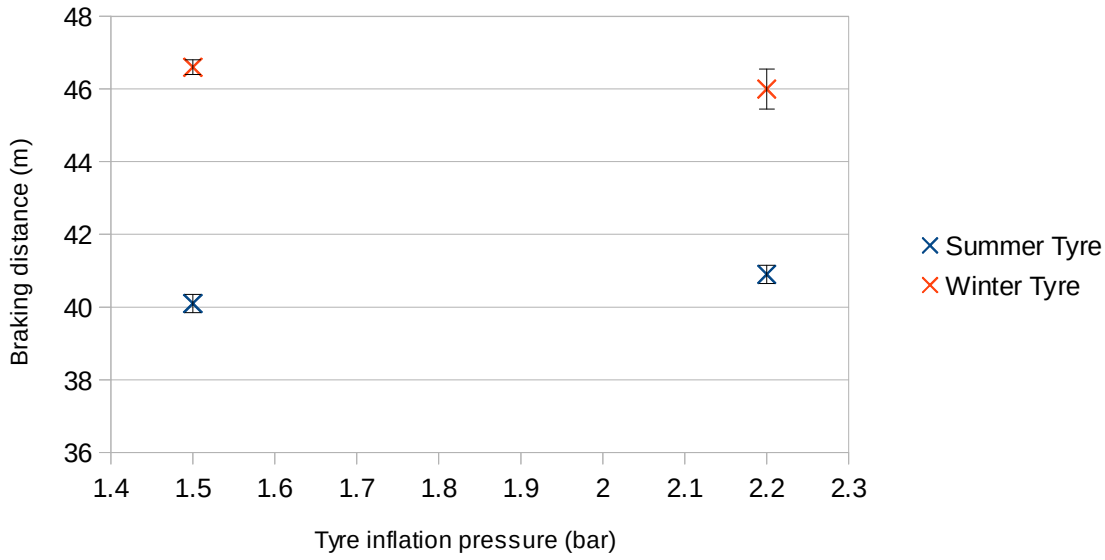

Figure 5.8: Braking distance for different tyre inflation pressures using Hyundai Avante HD

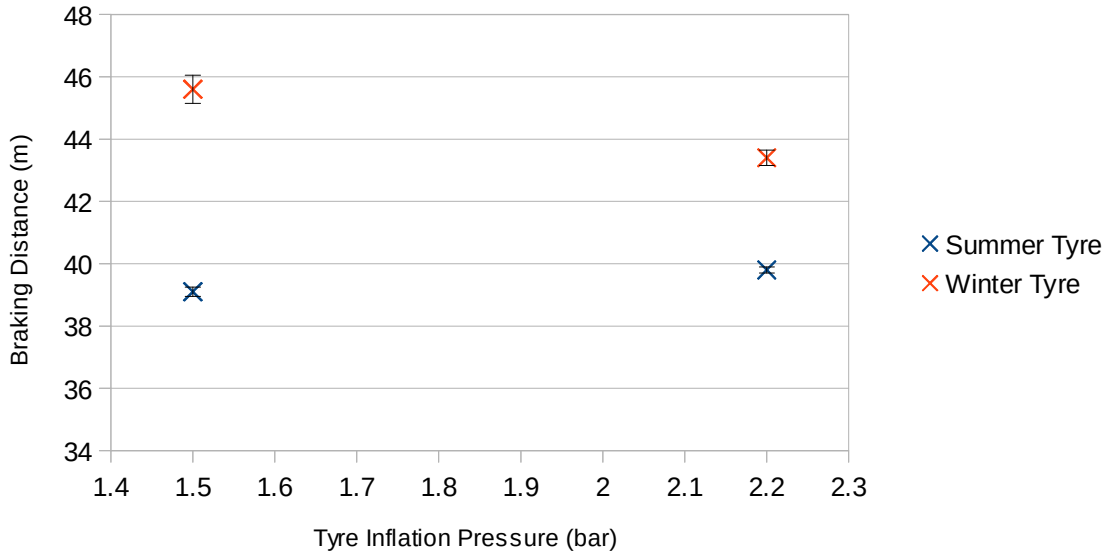

Figure 5.9: Braking distance for different tyre inflation pressures using Volkswagen Golf

The tests were performed under dry weather condition between February and March 2013. The winter tyres have a remarkably poorer performance on the brake distance compared to the summer tyres. This is due to the higher flexibility in the tread area of winter tyres to generate a high friction for snowy and icy conditions which is negative for braking on dry surfaces.

5.3 Performing a locked wheel pull test using a winch

In order to investigate the influence of the tyre pressure on the friction coefficient, winch tests were carried out. To this end, a winch was mounted on a tractor to pull a car with a constant velocity. Between the rope and the car, a load cell was placed as shown in Figure 5.10 and Appendix D.

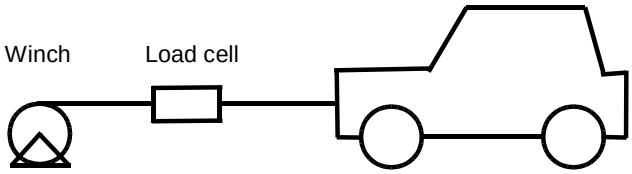

Figure 5.10: Experimental composition for pull tests

The load cell is produced by Wolpert and calibrated after ISO 7500 [87] with an uncertainty of 0.25% for the testing equipment.

Test load indicator	**Measurement series**				**Assessment**		
F_i (kN)	**F_1 (kN)**	**F_2 (kN)**	**F_3 (kN)**	**Mean $\bar{F}$ (kN)**	**q**	**b**	**U for k =2**
10	10.0439	10.0428	10.0435	10.0434	-0.43%	0.01%	0.50%
15	15.0941	15.0467	15.0739	15.0716	-0.48%	0.32%	0.50%
20	20.0746	20.0744	20.0745	20.0745	-0.37%	0.00%	0.50%

Table 5.5: Calibration sheet of load cell

The relative accuracy error q is expressed as percentage of the mean true force $\bar{F}$, given by the equation:

$$q = \frac{F_i - \bar{F}}{\bar{F}} \times 100 \qquad \text{(Equation 5.1)}$$

The relative repeatability error b is the difference between the highest and lowest measured values with respect to the average:

$$b = \frac{F_{max} - F_{min}}{\bar{F}} \times 100 \qquad \text{(Equation 5.2)}$$

The expanded uncertainty U is given by:

$$U = k \times u_c = k \times \sqrt{\sum_{i=1}^{n} u_i^2} \qquad \text{(Equation 5.3)}$$

where k is the coverage factor, u_c the combined uncertainty and u_1 to u_n the relevant standard uncertainties. For k = 2, the level of confidence for the expanded uncertainty is approximately 95 percent. The standard uncertainty can be calculated using the estimated standard deviation s [88]:

$$u = \frac{s}{\sqrt{n}} \qquad \text{(Equation 5.4)}$$

The measurement principle of the load cell is based on the inductive half bridge. The brakes of the car were locked. The tyre pressure was set to 1 bar, 2 bar, and 3 bar respectively. An example plot for pulling the car with the tyre inflation pressure of 3 bar is shown in Figure 5.11. The other results are presented in Appendix F. For each inflation pressure, three runs were performed.

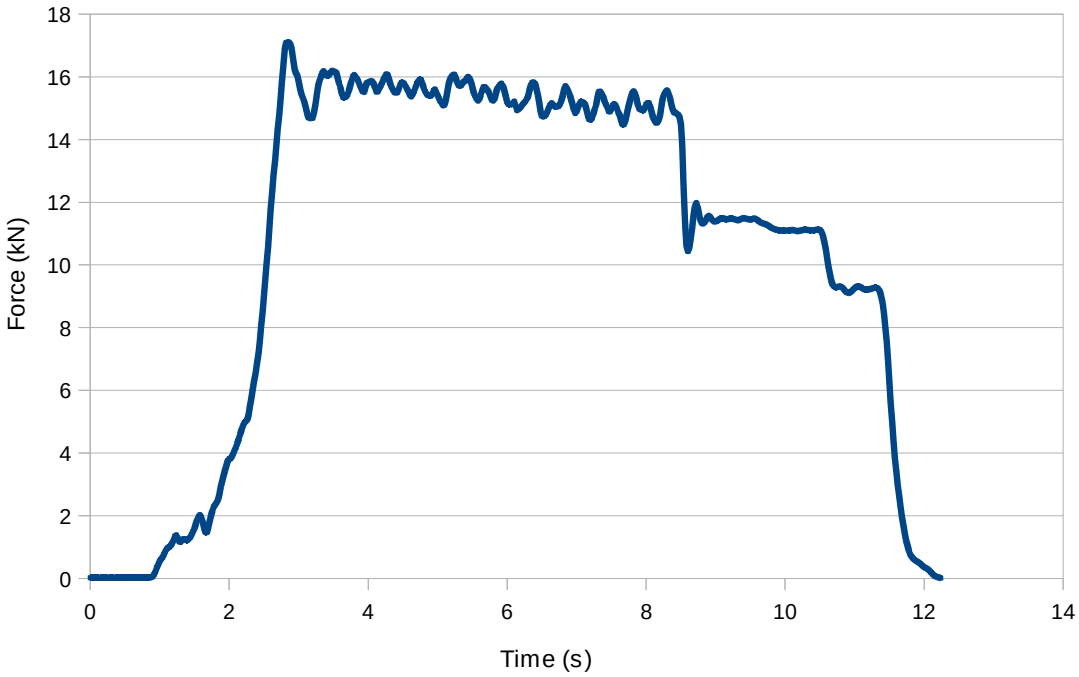

Figure 5.11: Evaluating plot for the first pull experiment at 3 bar

Evaluating the data shows only little difference in the pull force as can be seen in the following Table 5.5:

Number of pulls	1.0 bar	2.0 bar	3.0 bar
1	16.5 kN	17.7 kN	17.1 kN
2	16.6 kN	17.8 kN	17.6 kN
3	16.5 kN	16.5 kN	16.2 kN
Average	16.5 kN	17.3 kN	17.0 kN
Standard Deviation	0.1 kN	0.6 kN	0.6 kN

Table 5.6: The maximum pull force for different tyre inflation pressures.

Table 5.6 shows the average force to pull the car (sliding friction), which is the mean in Figure 5.11 between 2.8 and 8.5 sec.

Number of pulls	1.0 bar	2.0 bar	3.0 bar
1	15.6 kN	15.0 kN	15.7 kN
2	14.5 kN	15.8 kN	15.1 kN
3	15.0 kN	14.9 kN	14.1 kN
Average	15.0 kN	15.2 kN	15.0 kN
Standard Deviation	0.5 kN	0.4 kN	0.7 kN

Table 5.7: The average pull force for different tyre inflation pressures.

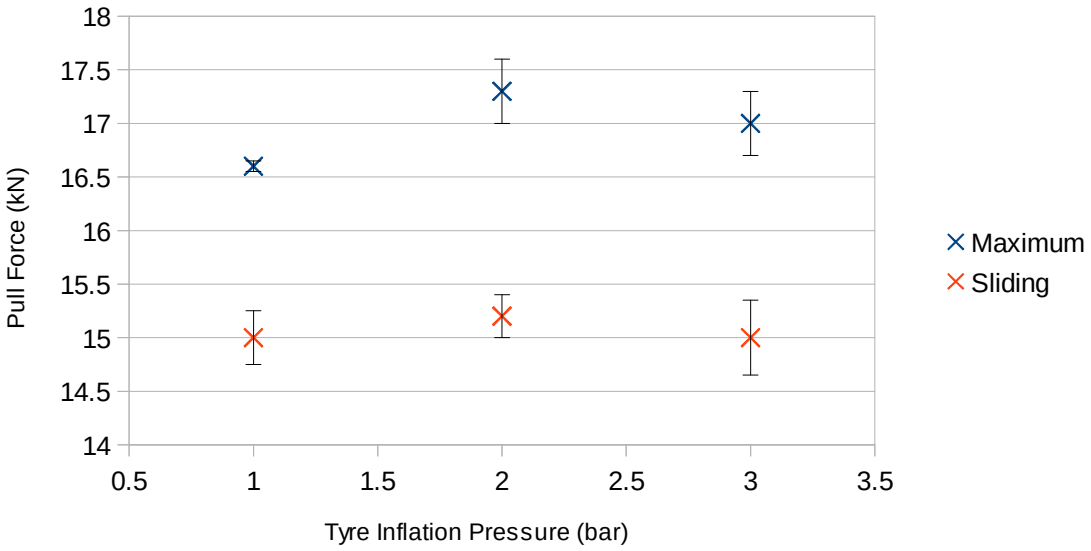

Figure 5.12: Pull force dependent upon tyre inflation pressure

Considering the weight of the car of 1900 kg the highest deviation for the maximum pull force of 0.8 kN is 4% of the total pulled weight. The experimental set-up caused inaccuracies, due to the fact that the vehicle brakes could not lock effectively the tyres during the whole test run. Reference is made to advanced, smaller experimental investigations at RWTH University Aachen measuring the influence of the contact area on the sliding friction [89].

Summary

As it can be shown from the data, the tyre inflation pressure has a negligible effect on the braking distance and, thus the size of the contact area. Also reference is made to [90], where similar findings are shown for ABS experiments. To explain the effect, Persson's theory is used and described in the following chapter.

Chapter SIX

Chapter six gives an introduction to Hertz', Greenwood-Williamson's, Bush's et al. and Persson's theories on contact mechanics. The fact that most real surfaces exhibit surface roughness across many decades of length scales, contact formation between two solids is still not understood very well. Then, a rubber friction law is introduced which can be used to calculate tyre and vehicle dynamics.

6. Contact mechanics

6.1 Introduction

The real area of contact when two solids are brought into contact is a fundamental question. The contact area influences a large number of physical properties e.g. heat transfer, friction, the contact resistivity, wear and adhesion between solids in sliding contact or in stationary. Hertz published his pioneering work in 1882 [91]. The frictionless contact between elastic solids with smooth surface profiles is studied. The theory uses parabolics as approximation and the contact area A increases non-linearly with the squeezing force F_N using $A \sim F_N^{2/3}$. A randomly rough but nominal flat surface is modelled using a regular array of spherical cups with the same diameter and height. Squeezing an elastic solid with a flat surface against the model, the area of real contact should scale as $F_N^{2/3}$ with the applied load. However, experiments with randomly rough surfaces have shown the real area of contact is proportional to F_N for purely elastic contact, as long as the contact area A is small, compared to the nominal contact area A_0. This is the physical origin of Coulomb's friction law. The friction law of Coulomb states that the friction is proportional to the normal load.

Greenwood and Williamson described the rough surface with spherical cups using the same diameter, but with a Gaussian distribution of heights. The model states, that the real area of contact is almost proportional to the applied load. Bush improved the model by approximating the summits with paraboloids [92].

The shown mechanical contact models assume the real area of contact A as very small compared to the nominal contact area A_0. Therefore, the interaction between different contact regions is neglected, e.g. when an asperity is squeezed against a flat, hard surface. The surface will not just deform locally, but the elastic deformation will extend at some distance away of the asperity. This influences the deformation of other asperities. Also, the described contact mechanic models can only applied as long as $A << A_0$.

The Persson theory uses the opposite limit of complete contact, when the pressure distribution at the interface is exact. Also the elastic coupling between the asperity contact regions is accounted. The theory predicts for small squeezing forces, that the contact area A is proportional to the nominal load F_N. While F_N increases A converges A_0 continuously. It was originally developed to describe rubber friction on rough surfaces.

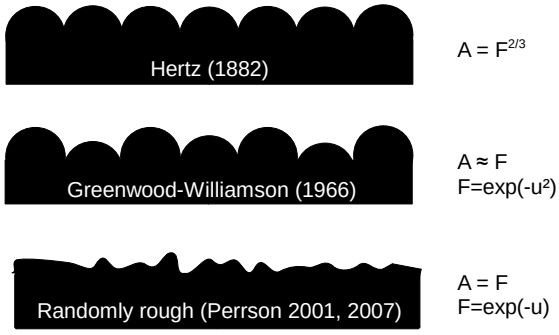

Figure 6.1: The three different models of a rough surface [93]

6.2 Hertz theory

Hertz describes the contact of two spherical, elastic bodies with the radius R_1 and R_2. The surfaces are perfectly smooth. The force F squeezes the spheres into contact and the deformation field in the solids can be calculated by minimizing the elastic deformation energy. The circular contact region is given by the radius r_0:

$$r_0 = \left(\frac{R_1 R_2}{R_1 + R_2}\right)^{1/3} \left(\frac{3\mathrm{F}\left(1-\nu^2\right)}{4E}\right)^{1/3} \qquad \text{(Equation 6.1)}$$

using:

$$\frac{1-\nu^2}{E} = \frac{1-\nu_1^2}{E_1} + \frac{1-\nu_2^2}{E_2} \qquad \text{(Equation 6.2)}$$

with ν_1 and ν_2 as the corresponding Poission ratios and E_1 and E_2 as the elastic moduli [94]. The two solids are approaching each other with the distance *s*, expressed by:

$$s=\left(\frac{R_1+R_2}{R_1 R_2}\right)^{1/3}\left(\frac{3\mathrm{F}\left(1-\nu^2\right)}{4E}\right)^{2/3} \quad \text{(Equation 6.3)}$$

Is a sphere with the radius *R* in contact with a flat surface, Equations 6.2 and 6.3 give the area of contact:

$$A=\pi r_0^2=\pi Rs \quad \text{(Equation 6.4)}$$

For calculating the squeezing force following equation can be used:

$$F=\frac{4E}{3\left(1-\nu^2\right)}s^{3/2}R^{1/2} \quad \text{(Equation 6.5)}$$

The pressure distribution in the contact area only depends on the distance r from the centre of the circular contact area:

$$\sigma\left(r\right)=\sigma_0\left[1-\left(\frac{r}{r_0}\right)^2\right]^{1/2} \quad \text{(Equation 6.6)}$$

The average pressure is:

$$\sigma_0=\frac{F}{\pi r_0^2} \quad \text{(Equation 6.7)}$$

To include adhesion between the two solid objects, the Hertz contact theory can be generalized. The deformation field in the solids is determined by minimizing the elastic energy and adding the interfacial binding energy which is done by Johnson-Kendall-Roberts.

6.3 Greenwood-Williamson theory

Greenwood and William [95] assume a frictionless contact between the elastic bodies. The system is described by $z = h_1(x)$ and $z = h_2(x)$ for the surface height profiles. The Young's elastic moduli is determined by E_1 and E_2, and the corresponding Poisson ratios by v_1 and v_2. Thus, without loss of generality, the contact problem is equivalent to the contact between a rigid solid with the roughness profile $h(x) = h_1(x) + h_2(x)$ and an elastic solid with a flat surface with the Young's modulus E and the Poisson ratio v, chosen that Equation 6.2 is obeyed.

The joint height probability distribution P_h depends on the area of contact and the load, as a function of the distance between the two converging solids. Assuming the surface roughness on a single length scale, the asperities are approximated as spherical cups with the same radius R and a Gaussian height distribution. Figure 6.1 illustrates the context.

$$P_h = \frac{1}{(2\pi)^{1/2} h^*} \exp\left(-\frac{h^2}{2h^{*2}}\right) \quad \text{(Equation 6.8)}$$

h* is the root-mean-square amplitude of the summit height fluctuations and is slightly smaller than the root-mean-square roughness amplitude h_{rms}. The elastic interaction between the asperity contact regions is neglected. The separation between the two surfaces is denoted by d. The asperity with the height will make contact with the plane. The penetration s is the difference of h and d. Thus, the Hertz contact theory with s = h – d gives the normalized area of real contact:

$$\frac{\Delta A}{A_0} = \pi n_0 R \int_d^\infty dh \ (h-d) P_h \quad \text{(Equation 6.9)}$$

Here, A_0 is the nominal contact area and n_0 the number of asperities per unit area. For calculating the number of asperities in contact per unit area is:

$$\frac{N}{A_0} = n_0 \int_d^\infty dh \ P_h \quad \text{(Equation 6.10)}$$

using to calculate the nominal squeezing stress:

$$\sigma_0 = \frac{F_N}{A_0} = \frac{4E}{3(1-\nu^2)} n_0 \int_d^\infty dh \ (h-d)^{3/2} R^{1/2} P_h \quad \text{(Equation 6.11)}$$

The Greenwood-Williamson theory is generalized for the adhesive contact between randomly rough surfaces by Fuller and Tabor. There, the Johnson-Kendall-Roberts asperity contact model is applied to each asperity contact area, instead of using the Hertz as it is used in the original theory [96].

6.4 Bush, Gibson and Thomas theory

Bush et al. neglect the elastic coupling between the asperities like Greenwood-Williamson. While Greenwood-Williamson assume roughness on a single length scale, Bush et al. includes roughness occurring on many different length scales. This means, the real area of contact is proportional to the squeezing force only for small squeezing forces, i.e., $A \sim F_N$ as long as $A << A_0$. Hence, for small loads, the real area of contact A is proportional to the load only when roughness occurs on many different length scales. The average size A of an asperity contact region and the stress distribution at the interface are independent of the applied load. The reason is that, as the load is increased, the exiting contact areas grow and new contact regions are formed. In the theory, the asperities are modelled as paraboloids with two different diameters and applying the Hertzian solution for their deformation. The asperities are determined with the heights h and the radii r_1 and r_2. When r_1 is the maximum and r_2 the minimum curvature, means $r_1 > r_2 > 0$. The theory predicts for small loads that the area of real contact is proportional to the load:

$$A = \alpha F_N$$

where

$$\alpha = \kappa \frac{(1-\nu^2)}{E} \left(\int d^2q \;\; q^2 C(q) \right)^{-1/2} \qquad \text{(Equation 6.12)}$$

with

$$\kappa = (2\pi)^{1/2}$$

For a detailed description of the model it is also referred to [97].

6.5 Persson theory

Persson's contact mechanics theory is not using the assumption of the other shown multiasperity contact theories, that the area of real contact is small, compared to the normal contact area. Instead, Persson's approach is using the limiting case of full contact condition, where the theory gives exact results. The approach moves between a rigid rough surface and an initially flat elastic half-space. It accounts for partial contact by requiring that the stress probability distribution vanishes when the local normal surface stress σ vanishes, in case of adhesionless contact [98, 99]. The fundamental concept is not to exclude any roughness length scale before. The magnification ζ refers the arbitrary chosen reference length scale. The reference length scale can be for example the lateral size L of the nominal contact area

$$\zeta = L/\lambda = q/q_L \qquad \text{(Equation 6.13)}$$

where λ is the shortest wavelength roughness which can be resolved at the magnification ζ. Input for the theory is the surface roughness power spectrum C(q) and the elastic properties E and v of the two objects in contact. Under the magnification ζ, the stress distribution in the contact area is P(σ, ζ). It satisfies the diffusion-like equation for complete contact where time is replaced by the magnification ζ [100]. The spatial coordinate is replaced with the stress σ and the diffusion constant f(ζ) depends on ζ.

$$\frac{\partial P}{\partial \zeta} = f(\zeta)\frac{\partial^2 P}{\partial \sigma^2} \qquad \text{(Equation 6.14)}$$

where

$$f(\zeta) = G'(\zeta)\sigma_0{}^2 \qquad \text{(Equation 6.15)}$$

and the average pressure in the nominal contact area

$$\sigma_0{}^2 = \frac{F_N}{A_0} \qquad \text{(Equation 6.16)}$$

where

$$G(\zeta)=\frac{\pi}{4}\left(\frac{E}{(1-\nu^2)\sigma_0}\right)^2 \int_{q_L}^{\zeta q_L} dq \quad q^3 C(q) \qquad \text{(Equation 6.17)}$$

The physical meaning of Equation 6.14 is explained in the following. Assuming a system at the lowest magnification $\zeta = 1$, where no surface roughness can be observed. The object makes contact with the substrate everywhere in the nominal contact area which is shown in Figure 6.3. In this case, the applied stress σ_0 equals the stress at the interface. The stress distribution is a delta function

$$P(\delta,1)=\delta(\sigma-\sigma_0) \qquad \text{(Equation 6.18)}$$

Introducing the surface roughness with wavelength down to Equation 6.13 to the system with increasing magnification leads to emerging non-contact regions. The stress distribution $P(\sigma, \zeta)$ exhibits, like shown in Figure 6.3 (b), as the stress must go to zero at the edges of the boundary between the contact and the non-contact regions. Increasing the magnification further, the distribution becomes even broader like in a diffusion problem which is shown in Figure 6.3 (c).

The stress distribution $P(\sigma, \zeta)$ at the interface is expressed with

$$P(\delta,1)=\frac{1}{A_0}\int_A d^2x \quad \delta(\sigma-\sigma(x,\zeta)) \qquad \text{(Equation 6.19)}$$

and $\sigma(x, \zeta)$ is the stress at the interface including only surface roughness components with the wavevector $q < \zeta q_L$. A is the area of contact and used for the integration. An integration over the whole surface area A_0 would have a delta function $[(A_0 – A) / A_0]\delta(\sigma)$. In this approach, this term is excluded. The real area of contact on the xy-plane can be directly obtained form the stress distribution. From Equation 6.19 follows

$$\frac{A(\zeta)}{A_0}=\frac{1}{\sqrt{\pi}}\int_0^{\sqrt{G}} dx \quad e^{-x^{2/4}}=erf\left(\frac{1}{2}\sqrt{G}\right) \qquad \text{(Equation 6.20)}$$

Figure 6.2 (a) shows the dependency of the normalized contact area A/A_0 at the highest magnification on the squeezing pressure σ_0. The dependency on the magnification of $A(\zeta)/A_0$ is shown in Figure 6.2 (b). The theory predicts a linear increase of the contact area with the load for low squeezing pressures. $\zeta = 1$ refers to a resolution $\lambda_0 = 2\pi/q_0$ for a constant nominal pressure σ_0. The area of contact decreases monotonically with increasing the magnification which introduces shorter roughness wavelength components. The true area of contact would vanish if no short distance cut-off exists. The theory is investigated numerically in [101].

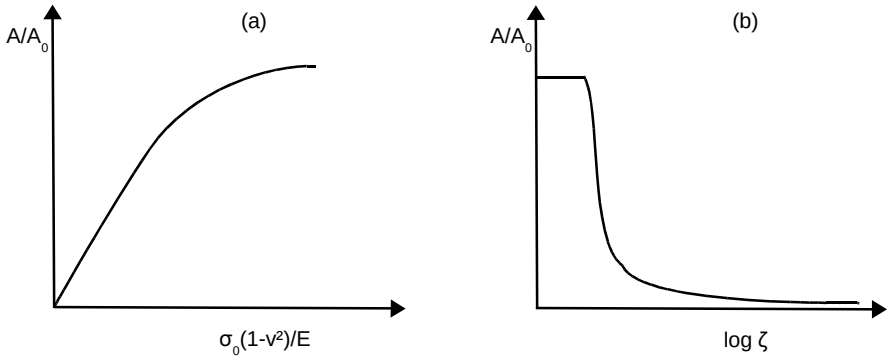

Figure 6.2: The dependence of the normalized contact area at the highest magnification A/A_0 on the squeezing pressure σ_0 in units of $E/(1-\nu^2)$ and the dependence of A/A_0 on the logarithm of the magnification (b)

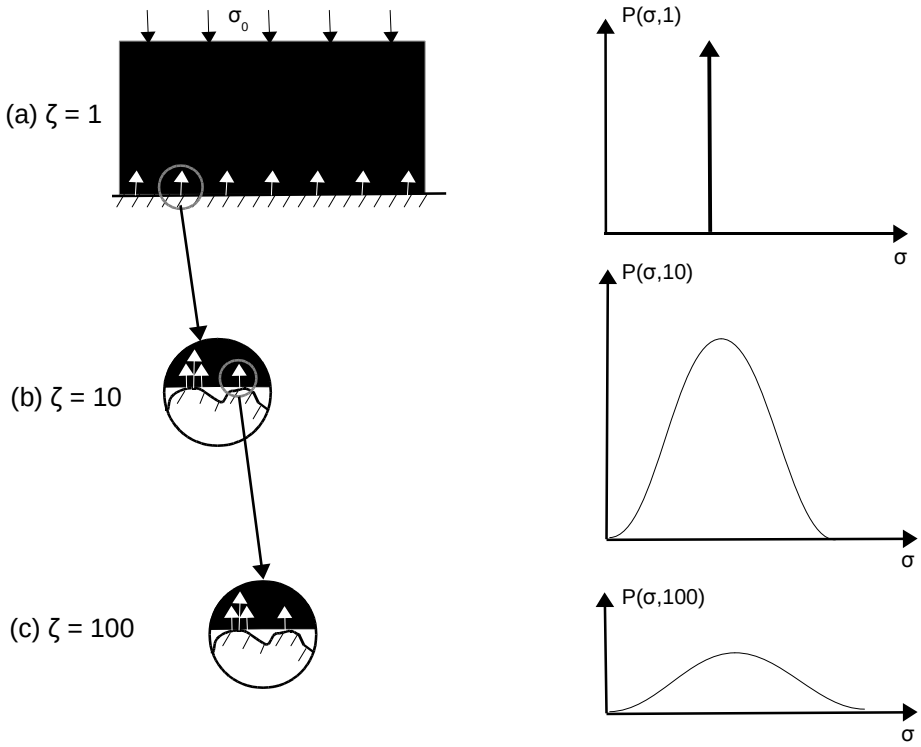

Figure 6.3: The stress distribution at increasing magnification in the contact area between an elastic substrate and a rigid block

6.6 Rubber friction theory

Rubber friction is a crucial topic, especially for practical applications. Examples are tyres, wiper blades, rubber seals, syringes or conveyor belts [102, 103, 104, 105, 106, 107, 108, 109, 110, 111, 112, 113, 114]. In most theoretical studies, rubber friction is described using very simple phenomenological models, e.g. the Coulomb friction law. The friction coefficient may depend on the local sliding velocity. However, rubber friction depends on the history of the sliding motion (memory effects), which is found to be very important for an accurate description of rubber friction, as shown in previous contributions [115]. When rubber is sliding on a hard rough substrate, the history dependency of friction is mainly due to frictional heating in the rubber-substrate contact regions. Many experimental studies have shown the influence of frictional heating on the rubber friction as an apparent dependence of the rubber friction on the normal stress.

Many papers have been published related to tyre dynamics, e.g. in the context of ABS braking models. The central point in tyre dynamics is the road-tyre interaction, thus the rubber friction. Hence, unless this friction is accurately described, no tyre model, independent of the tyre body description detail level, will provide an accurate representation of the tyre dynamics. Usually the road-tyre friction is described only in a very approximate way. Many sophisticated finite element models for tyre dynamics, describe the frictional interaction only via a static and a kinetic rubber friction coefficient. In other studies, the dynamic behaviour of the whole tyre is described simply by using interpolation formulas. The most famous example is the well established Magic Formula [116]. However, this approach requires a very large set of measurements to characterize the tyre properties which is very expensive and time-consuming to obtain. In addition, it cannot describe the influence of the sliding history (memory effects) on tyre dynamics.

Rubber friction depends on the history of the sliding motion, because the temperature in the rubber-road asperity contact regions at time t depends on the sliding history for all earlier times t' < t due to frictional heating. This dependency is called memory effect which is essential for an accurate description of rubber friction. This effect is illustrated in Figure 6.4 and Figure 6.5 for rubber tread blocks sliding on different surfaces. The calculated kinetic friction coefficient for stationary sliding without flash temperature is shown as blue curve, whilst the red curve includes the flash temperature, as a function of the velocity v of the bottom surface of the rubber block. The black lines represent the effective friction during non-stationary sliding, experienced by a rubber tread block during braking at various slips. Note that some finite sliding distance is necessary in order to fully develop the flash temperature effect. The initial friction acting on the tread block follows the blue curve according to 'cold-rubber'. In this case, the flash temperature is negligible. For larger slip distances the friction follows the hot branch (red curve). Therefore, it is not possible to describe rubber friction accuratly using only a static and a kinetic friction coefficient, as is usually done, even in advanced finite-element tyre dynamics models. In fact, as shown above, the friction cannot even be described by a function $\mu(v)$ which depends on the instantaneous sliding velocity $v(t)$, but the friction depends on $v(t')$ for all times $t' \leq t$ (memory effect).

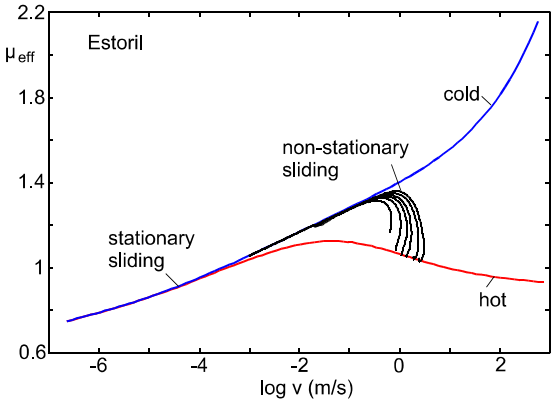

Figure 6.4: The kinetic friction coefficient (stationary sliding) as a function of the logarithm (with 10 as basis) of the sliding velocity

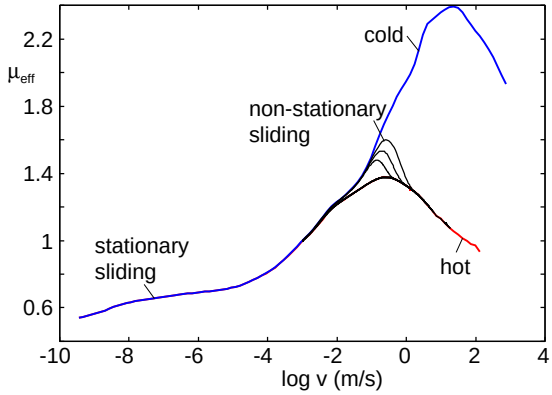

Figure 6.5: Same as in Figure 6.4 but for sandpaper surface and a different rubber compound

The results in Figure 6.4 are for a tyre on an asphalt road surface. The blue line, marked “cold”, is without the flash temperature. The red line, marked “hot”, is including the flash temperature. The black curves are showing the effective friction, experienced by a tread block, when it goes through the footprint, for the car velocity 27 m/s and for several slip values 0.005, 0.0075, 0.01, 0.03, 0.05, 0.07 and 0.09. The experienced friction of the tread block follows first the“cold“ rubber branch of the steady state kinetic friction coefficient. After, when the block has slipped a distance of order of the diameter of the macroasperity contact region, and the flash temperature has fully evolved, the “hot” rubber branch is followed. Here the so-called macroasperity contact regions (see below) are relatively large, because of the large sand particles on the road surface. For other substrates such as safety walk or sandpaper, the size of the macroasperity contact regions can be very small. In this case, even a very small slip distance will result in motion along the hot-rubber branch. This is illustrated in Figure 6.5 for non-stationary sliding experienced by a rubber tread block during braking at various slip values 0.07, 0.15 and 0.8 for the car velocity 16.66 m/s on the sandpaper 80 substrate used in the tyre dynamics measurements presented later. The experienced friction of the tread block follows first the “cold“ rubber branch of the steady state kinetic friction coefficient. And after, when the block has slipped a distance of order the diameter of the macroasperity contact region, the “hot” rubber branch is followed.

To give a preparation to what follows, the rubber friction theory is reviewed. In the theory the road asperities cause the viscoelastic deformations of the rubber surface which result in energy dissipation. An asperity contact region with the diameter d generates time dependent (pulsating) deformations of the rubber. The deformation is characterized by the frequency ω = v/d, where v is the sliding velocity. The viscoelastic deformation, and most of the energy dissipation, extend into the rubber by a characteristic distance of order d. Therefore, most of the energy dissipation occurs in a volume element of d^3 order. To have a large asperity-induced contribution to the friction, the frequency ω should be close to the maximum of the tanδ = ImE(ω)/ReE(ω) curve. Here, E(ω) is the viscoelastic modulus of the rubber. In reality, there will be a wide distribution of asperity contact sizes. This means, there will be a wide range of deformation frequencies, lets say from ω_0 to ω_1, as shown in Figure 6.6. A large friction requires, that tanδ is as big as possible for all these frequencies.

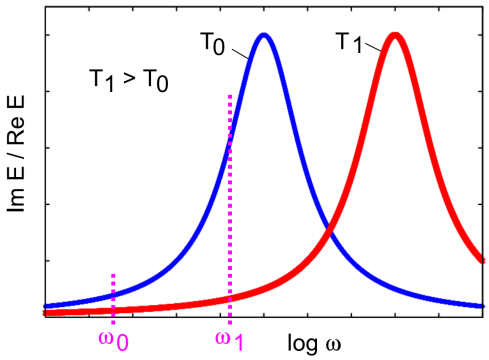

Figure 6.6: When the temperature increases the tanδ =ImE/ReE spectra shifts to higher frequencies

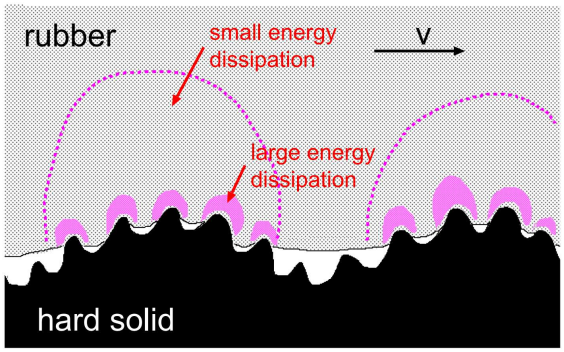

Figure 6.7: The energy dissipation per unit volume

Usually, the viscoelastic modulus of rubber-like materials depends strongly on the temperature T. When the temperature increases the tanδ =ImE/ReE spectra shifts to higher frequencies. In general, this results in a decrease of the rubber friction. It is assumed that the road asperities causes pulsating frequencies in the range between ω_0 and ω_1. An increase in temperature by 10°C may shift the tanδ-curve to higher frequencies with one frequency decade. In general, this will reduce the rubber friction, shown in Figure 6.6.

The distribution of asperity sizes is usually very wide for real surfaces. A good picture of a rough surface is to think about it as big asperities on top of which occur smaller asperities on top of which occur even smaller asperities and so on. This is shown in Figure 6.7 where roughness occurs on two length scales. To get the total energy dissipation during sliding on a real surface, it is needed to sum up the contribution from asperity induced deformation of the rubber on all relevant length scales. It is of importance to note that different decades in length scales may be equally important. The highest energy dissipation is in the smallest asperity contact regions.

Temperature has a significant influence on rubber friction. The most important contribution to rubber friction is the viscoelastic energy dissipation. This results in a local heating of the rubber in the region, where the energy dissipation occurs. This results in local temperature increase which becomes larger when smaller and smaller asperity contact regions are observed. This in time-and-space local temperature increase is referred to as the flash temperature. The flash temperature has an extremely significant effect on the rubber friction which is illustrated in Figure 6.4 and Figure 6.5. In the figures the calculated steady state kinetic friction coefficient is shown, when a block of tread rubber is sliding on an asphalt road surface. The upper curve is the result without taking the flash temperature into account. This means the temperature is assumed to be the same as the background temperature T_0 everywhere. The lower curve is including the flash temperature. Note that for sliding velocities $v > 0.001$ m/s, the flash temperature results in a decrease of the sliding friction. For velocities $v < 0.001$ m/s, the produced heat has enough time to diffuse away from the asperity contact regions, resulting in a negligible flash temperature effect.

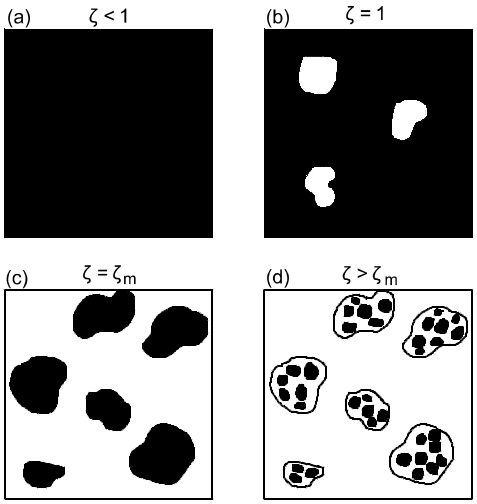

Figure 6.8: The contact region between a tyre and a road surface

The concept of the macroasperity contact region is very important for the rubber friction theory. Studying the footprint contact region between a tyre and a road surface at different magnification ζ shows the following: at low magnification, the road surface seems smooth and the contact between the tyre and the road appears to be complete within the footprint area. This is illustrated in Figure 6.8 (a). However, increasing the magnification ζ, non-contact regions can be detected (see Figure 6.8 (b)). At high enough magnification, isolated contact regions can be observed as presented in Figure 6.8 (c). When the magnification increases even further, contact regions break up into even smaller contact regions as shown in Figure 6.8 (d). The contact regions observed in Figure 6.8 (c) are denoted as the macroasperity contact regions with the average diameter D. Also, the corresponding magnification is denoted by ζ_c. Formally, ζ_c is defined to be the magnification, where the second derivative of logP(ζ) with respect to logζ has its first maximum with increasing ζ [117]. When the nominal pressure in the tyre-road contact region is small enough, the macroasperity contact regions get separated. But the separation between the microasperity contact regions within the macroasperity contact regions are in general rather small. When the flash temperature effect is calculated, the produced heat by the microasperity contact regions is smeared out uniformly within the macroasperity contact regions. For road surfaces $D \approx 0.1 - 1$ cm and the fraction of the tread block surface occupied by the macroasperity contact regions is

typically between 10% and 30%.

It is assumed that only the surface roughness with wavevectors $q < q_1$ has a contribution to the friction in the theory. For clean road surfaces the cut-off wavevector q_1 is determined by a yield condition: It is assumed that the local stress and temperature in the asperity contact regions on the length scale $1/q_1$ are so high that the rubber bonds break resulting in a thin modified (dead) layer of rubber at the surface region of thickness $\approx 1/q_1$. In another approach by of Heinrich and Klüppel a different mechanism for obtaining q_1 is presented [118].

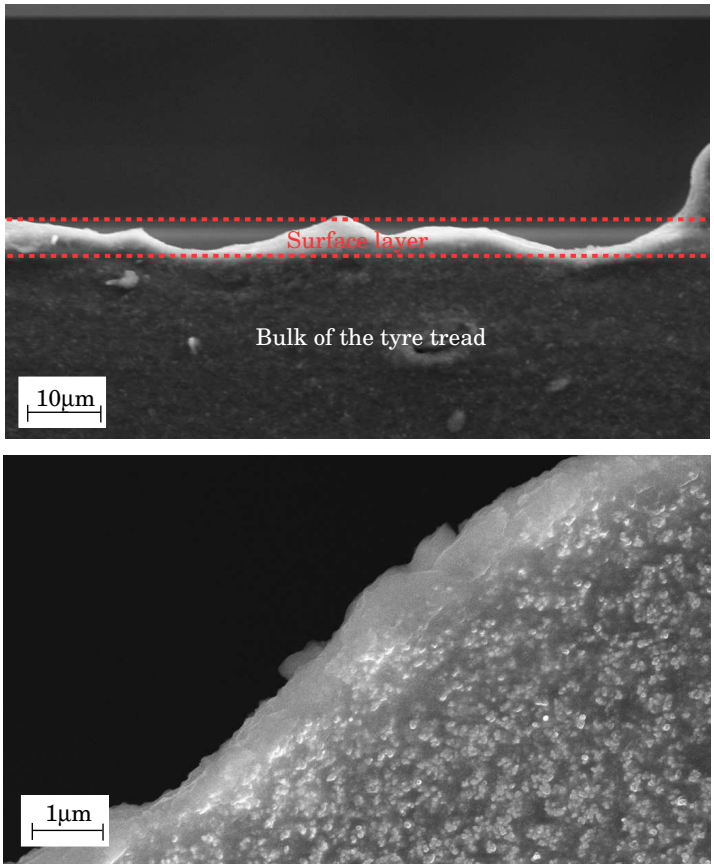

Figure 6.9: SEM pictures of the surface region of a car tyre tread block at low magnification (top) and at higher magnification (bottom)

Modified surface layers have indeed been detected on rubber tread blocks [119]. Figure 6.9 shows scanning electron microscopy (SEM) pictures of the surface region of a tyre tread block at two different magnifications. Acknowledgement is made to Dr Marc Masen, Imperial College London for providing the pictures. In the high magnification picture (bottom picture) one can observe a ≈ 1 μm thick layer of modified rubber. Note that in this layer no filler particles (carbon black) can be observed. Energy-dispersive x-ray spectroscopy analysis showed an increased concentration of oxygen when compared to the bulk material. The increase of oxygen in the surface region suggests that the rubber reacts chemically with the environment and is undergoing oxidation processes during sliding. This is indeed expected because of the high (flash) temperature and large stresses in the rubber road asperity contact regions during slip. The viscoelastic properties of the modified surface layer were studied using indentation experiments. It was found that the surface layer is much softer than the bulk, with a long-time (relaxed) modulus about ≈ 1000 times smaller than in the bulk, while the short-time response indicated a ≈ 5 times softer surface layer. Furthermore, the viscoelastic spectral density exhibited much slower relaxation processes (longer relaxation times) than in the bulk. From this follows:

(1) The rubber friction after run-in is rather insensitive to the road surface roughness on clean roads. This has been found in different experimental studies [120], and can be understood as follows. The cut-off q_1 on surfaces with smoother and less sharp roughness, or for surfaces where the roughness occurs at shorter length scales, will be larger, i.e. the cut-off wavelength $\lambda_1 = 2\pi/q_1$ will be smaller, than for road surfaces with larger roughness in such a way that the temperature and stress increase in the asperity contact regions observed at the resolution λ_1 or magnification $\zeta = q_1/q_0$, are roughly the same on all surfaces. This means that a larger range of roughness will contribute to the rubber friction on “smoother” surfaces as compared to more rough surfaces. From this follows that the friction after run-in may vary much less between different clean road surfaces than expected from the variation of the magnitude of the surface roughness.

(2) The cut-off q_1 may be determined by the nature of the road surface contamination. In this case, if the cut-off is fixed, for example by the size of the contamination particles, a much larger change in the friction coefficient can be observed between different road surfaces, and for tyres with different types of tread rubber.

For clean surfaces q_1 is determined by the thickness of a thin modified (dead) layer (see Figure 6.9) which is generated by the high stresses and temperatures at the tread rubber surface during run-in. This process is likely also related to rubber wear. Rubber wear occurs during slip and leads to a contamination of the track by small wear elements. This may have some effect on the sliding friction. It is also well known to occur when a car brakes or accelerates on a road, leaving black strips of rubber particles on the road surface. However, it is not expected that the wear particles have a large effect on the investigated friction. This is because most of them are of similar size as the cut-off distance is determined by the rubber strength. During moderate slip the particles only cover a small part of the road surface. Also, this statement is supported by lab experiments where a negligible change in the rubber friction force is observed, when the same rubber tread element, or rubber block slides a second time on the same, not cleaned road track, or even on a much smoother grinded steel surface.

The cut-off length $1/q_1$ depends on the rubber compound use, and also on the characteristics of the road surface. Changing the road surface requires some short run-in to form a new thin modified surface layer on the tread block which is corresponding to a new cut-off length. A set of equations are derived describing the friction acting on a rubber block squeezed with the stress σ_0 against a hard randomly rough surface. In the following, the basic equations are summarized. There are two contributions to the frictional stress $\sigma_f = \mu(t)\sigma_0$ existing. One is the dissipation of energy inside the rubber which is because of viscoelasticity of the rubber material. This depends on the history of the sliding motion (velocity $v(t) = \dot{x}(t)$) expressed via the following series of equations:

$$\mu(t) = \frac{1}{2}\int_{q_0}^{q_1} dq \;\; q^3 C(q) P(q,t) \;\times\; \int_0^{2\pi} d\phi \;\; \cos\phi \, \mathrm{Im} \frac{E(qv(t)\cos\phi, T_q(t))}{(1-\nu^2)\sigma_0} \quad \text{(Equation 6.21)}$$

The flash temperature at time *t* enters in:

$$T_q(t)=T_0+\int_0^t dt'\ \ \Gamma(t,t')\int_{q_0}^{q_1} dq'\ \ f(q',t')\times\frac{1}{\pi}\int_0^{\infty} dk\ \ \frac{4q^2}{k^2+4q^2}4q'\frac{2}{k^2+4q'^2}e^{-Dk^2(t-t^2)}$$

(Equation 6.22)

where Γ(t,t') = h(ω(t,t')) with

$$h(\omega)=1-\frac{2}{\pi}\omega(1-\omega^2)^{1/2}-\frac{2}{\pi}\arcsin\omega$$

(Equation 6.23)

for ω < 1 and h(ω) = 0 for ω > 1, and where ω(t, t') = [x(t) − x(t')]/2R depends on the history of the sliding motion. The function

$$f(q,t)=\frac{v(t)}{\rho C_v}q^4C(q)\frac{P(q,t)}{P(q_m,t)}\times\int d\phi\ \ \cos\phi\,\mathrm{Im}\,E\frac{(qv(t)\cos\phi,T_q(t))}{1-v^2}$$

(Equation 6.24)

where v(t) = ẋ(t) depends on time. The function P(q,t) (which also depends on time) is represented by:

$$P(q,t)=\frac{2}{\pi}\int_0^{\infty} dx\ \ \frac{sinx}{x}\exp[-x^2G(q,t)]=erf\left(\frac{1}{2\sqrt{G}}\right)$$

(Equation 6.25)

where

$$G(q,t)=\frac{1}{8}\int_{q_0}^{q} dq\ \ q^3C(q)\int_0^{2\pi} d\phi\ \left|\frac{E(qv(t))\cos\phi,T_q(t)}{(1-v^2)\sigma_0}\right|^2$$

(Equation 6.26)

The second contribution to the rubber friction is deduced from the area of (apparent) contact observed at the magnification ζ_1 and is given by $\tau_f A_1/A_0$. Here, τ_f (v) the weakly velocity-dependent effective frictional shear stress is acting in the contact area $A_1 = A(\zeta_1) = P(q_1, t)$. This theory is denoted as the “full theory”.

6.7 The phenomenological rubber friction law

In automotive tyre applications, for a slip between 5-10% and a typical footprint length of 10 cm, the slip distance of a tread rubber block in the footprint will be of order 1 cm. This is of the order or larger than the diameter D of the macroasperity contact regions. As long as the slip distance r(t) is small compared to D the friction follows the cold rubber branch of the steady state relation μ(v) (see blue curve in Figure 6.4). So $\mu(t) \approx \mu_{cold}(v(t))$ for the slip distance r(t) << D. When the tread block travels towards the end of the footprint the slip distance r(t) may be of the order of D, or larger, and the friction will follow the hot branch of the μ(v) relation. This means $\mu(t) \approx \mu_{hot}(v(t))$ for r(t) > D. It is found that the following history dependent friction law below predicts almost the same as the full theory presented above:

$$\mu(t) = \mu_{cold}(v(t), T_0)\, e^{-r(t)/r_o} + \mu_{hot}(v(t), T_0)\left[1 - e^{-r(t)/r_0}\right] \qquad \text{(Equation 6.27)}$$

Here v(t) is the instantaneous sliding velocity, r(t) is the sliding distance, and $r_0 \approx 0.2D$. Equation 6.27 is denoted as the cold-hot friction law. The length D which is typically $D \approx 0.1 - 1$ cm, depends on the road surface and on the rubber compound. Applying the full friction theory, the functions $\mu_{cold}(v, T_0)$, $\mu_{hot}(v, T_0)$ and the length D can be calculated.

To illustrate the accuracy of the cold-hot rubber friction law (Equation 6.27), the dynamics of one tread block is analysed as it travels through the tyre-road footprint. The frictional shear stress acting on a tread block as a function of time for many slip values: 0.005, 0.0075, 0.01, 0.03, 0.05, 0.07, 0.09, 0.12, 0.15 and 0.25 is shown in Figure 6.10. For the car velocity 27 m/s and tyre background temperature $T_0 = 60°C$. Note that the cold-hot friction law (Equation 6.27) (red curves) gives approximately the same result when compared with the full friction theory (green curves). The μ-slip curve for a passenger car tread compound is shown in Figure 6.11.

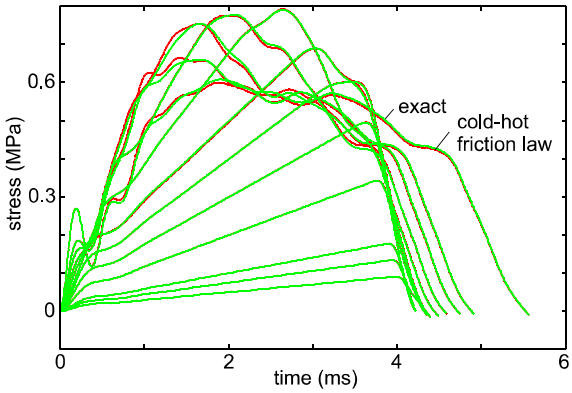

Figure 6.10: The frictional shear stress acting on a tread block as a function of time for many slip values

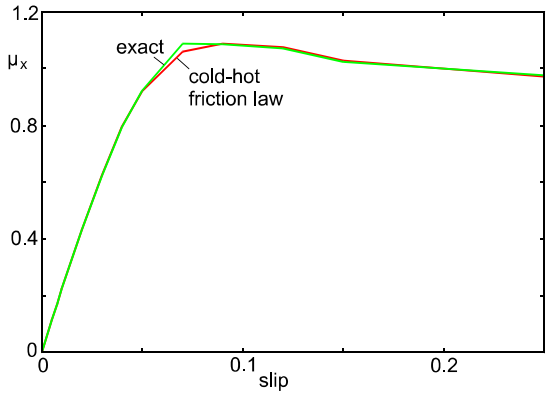

Figure 6.11: The μ-slip curve for the 1D tyre model using the full friction model and the cold-hot friction law (Equation 6.27)

Chapter SEVEN

Chapter seven compares the friction law to experimental data. A one- and two-dimensional tyre model is introduced which combines the rubber friction law with a mass-spring description of the tyre body. The tyre model is very flexible and can be applied to different manoeuvres. It can be used for calculating μ-slip curves, self aligning-torque, braking and cornering or combined motion (e.g. braking during cornering). The theory predictions are compared to measured data from indoor tyre testing on sandpaper substrate.

7. Comparison of theory and experimental data

7.1 Characterisation of the viscoelastic properties of rubber

The characterisation of the viscoelastic properties of rubber is a topic of great interest. It is used for example for contact mechanics or rubber friction calculations. It is necessary to have the information about the complex elastic modulus over a large frequency range and at different strain values including very large strain of 100%. A common way to measure the viscoleastic modulus is to deform the rubber sample oscillating with a constant strain or stress amplitude at different frequencies and then repeated at different temperatures. The gained values can be time-temperature shifted (TTS) to a master curve at a chosen reference temperature, covering a broad range of frequencies. In this study the Q800 produced by TA Instruments is used for the dynamic mechanical analysis (DMA), shown in Appendix G. The device covers a temperature range between -150°C and 600°C. The isothermal stability is ±0.1°C and the modulus precision ±1%. The rubber sample is clamped on both sides and elongated in an oscillatory manner. The rubber sample was cut out of the tyre tread pattern. Samples with a rectangular cross-section of order 1.5 mm x 1.5 mm with a length of about 30 mm are formed. When a sample is fixed by the clamps, the free sample length is about 6 mm between the top and bottom clamp.

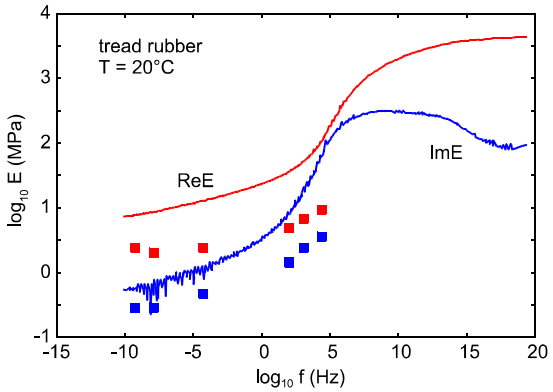

Figure 7.1: The logarithm of the real and imaginary part of the viscoelastic modulus as a function of the logarithm of the frequency

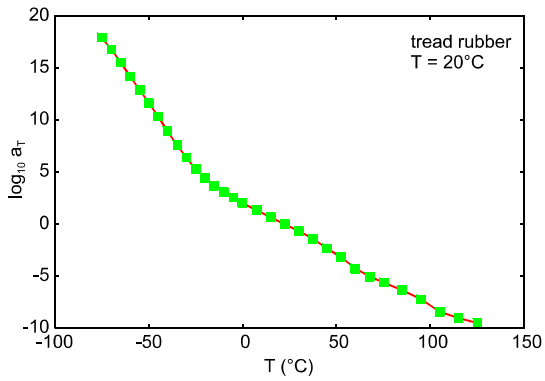

Figure 7.2: The shift factor a_T as a function of the temperature T

First, the complex viscoelastic modulus is measured in constant strain mode with an amplitude of 0.2% strain at different frequencies. The frequencies in the experiment are 28.0 Hz, 25.0 Hz, 14.0 Hz, 7.9 Hz, 4.4 Hz, 2.5 Hz, 1.4 Hz, 0.79 Hz, 0.44 Hz and 0.25 Hz. The strain is chosen rather small to avoid strain softening effects, e.g. the Mullins or Payne effect, as these effects can change significantly the viscoleastic response of the sample. To measure in tension mode requires to prestrain the sample with a static strain which needs to be larger as the dynamic strain during oscillation. To avoid compressing the rubber during the experiment, the prestrain has been set to 250% of the dynamic strain. The device automatically controls the prestrain for each measurement point.

The temperature is starting at -50°C and is increased by 5°C when the modulus is measured at all mentioned frequencies till 120°C is reached. The gained results are shifted in order to form either a smooth E' or E'' master curve. In Figure 7.1 is the logarithm of the real (red) and the imaginary (blue) part of the viscoelastic modulus as a function of the logarithm of the frequency of the tread rubber compound at the reference temperature T_0 = 20°C shown. The square symbols are large strain or stress results obtained from strain-sweep data using the self-consistent stress procedure (Equation (13) in Ref. [121]) for a substrate surface with the rms slope $\kappa = 0.7$. Figure 7.2 shows the shift factor α_T as a function of the temperature T for the same rubber compound. The reference temperature is T = 20°C. It is also used to shift the individual strain sweep measurements in Figure 7.3. The curves are obtained at different temperatures starting from 120°C to −40°C.

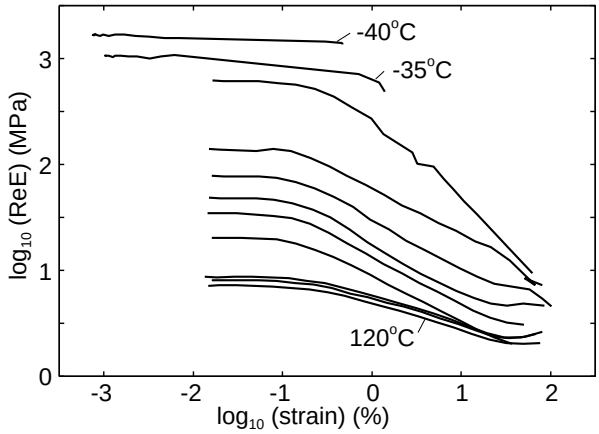

Figure 7.3: Logarithm of the real part of E as a function of the applied strain during oscillation at different (fixed) temperatures at fixed frequency of 1 Hz

To approximately describe softening effects like the breakdown of the rubber-filler network, called the Payne effect, a second strain sweep experiment is performed to include the non-linear behaviour in the characterisation of the material. Here, the rubber sample is measured at different fixed temperatures at a fixed frequency of 1 Hz, while the strain amplitude is increased from very small values ~ 0.04% until the maximum force of the instrument is reached or the sample breaks. A new rubber sample is used for each measurement, starting with a temperature of T = 120°C to T = -40°C. The data of the strain sweeps are time-temperature shifted using the shift factor α_T obtained by the small strain measurement. The master curve can be interpolated at all relevant strain values.

Figure 7.4 shows tangent delta (tanδ) as a function of frequency as obtained using experimental data for a tread rubber compound. The temperature T = 20°C and the red curve is for small strain (0.2%), while the green squares are the large strain or stress results obtained from strain-sweep data using the self consistent stress procedure for a substrate surface with the rms slope $\kappa = 0.7$.

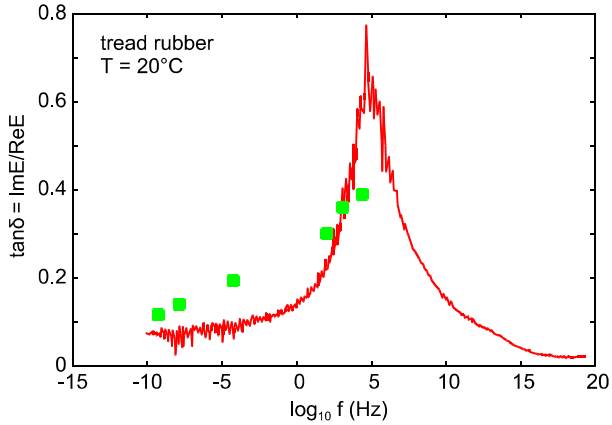

Figure 7.4: tanδ as a function of frequency, as obtained using experimental data for a tread rubber compound

7.2 Surface roughness

To specify and quantify the surface roughness, the vertical deviations z = h(x,y) of a real surface from its ideal form is used. A large deviation means a rough surface, while a small deviation means a smooth surface. For the roughness characterisation usually simple parameters are used, e.g. the arithmetic average R_a, the average R_z or the root-mean-square surface roughness R_q. A randomly rough surface can be generated using h(x) as a Gaussian random variable. The statistical properties of the surface are described by the power spectrum C(q), also called power spectral density. Transforming the height-height correlation function using Fourier

$$C(q) = \frac{1}{(2\pi)^2} \int d^2x \ \langle h(x)h(0)\rangle e^{-iq\cdot x} \qquad \text{(Equation 7.1)}$$

The topography information z = h(x,y) is transformed from real space x = (x,y) to frequency or wavevector space q = (q_x, q_y), where q = 2π/λ is the roughness wavelength. The power spectrum describes how the signal varies with frequency. For this case z = h(x) is the height of the surface at the point x = (x,y) above a flat reference plane chosen that ⟨h(x)⟩ = 0. The angular bracket represents the ensemble averaging.

However, most surfaces of interest are approximately self-affine fractals. A property of a fractal surface is, that magnifying a section with different magnifications in the perpendicular direction to the surface as compared with the in plane direction, it looks the same. Also the statistical properties are invariant under this scale transformation. The self-affine fractal surface power spectrum is

$$C(q) \sim q^{-2(H+1)} \qquad \text{(Equation 7.2)}$$

where H is the Hurst exponent related to the fractal dimension using $D_f = 3 - H$. In reality, surfaces are not self-affine over all length scales. Hence, the largest possible wavevector is $q_1 \approx 2\pi/\alpha$ where α is the smallest relevant length scale, e.g. an atomic distance or lattice constant. The smallest possible wavevector is $q_L \approx 2\pi/L$, defined by the linear size L of the surface. In good approximation technologically important surfaces are self-affine fractals in some finite wavevector regime $q_0 < q < q_1$, shown in Figure 7.5. The typical fractal dimension of sand blasted surfaces or surfaces prepared by crack propagation is typically $D_f \approx 2.2$ to 2.5.

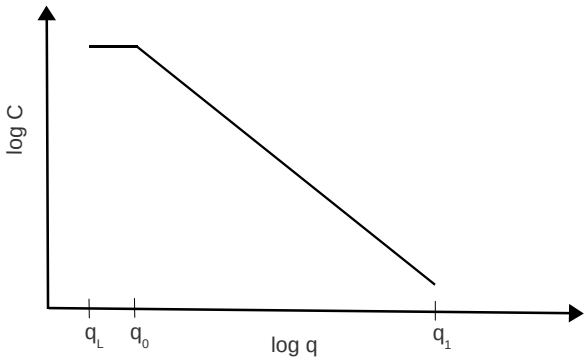

Figure 7.5: The surface roughness power spectrum of a surface which is a self-affine fractal

In this study the surface topography of the sandpaper surface used in the tyre dynamics experiments is measured. However, the measurements were done on used sandpaper when it was removed from the experimental set-up after long time of use. The surface of the sandpaper was much smoother than that of new sandpaper of the same type due to wear when the tyres slip over the sandpaper. The actual tyre friction measurements were done some time in the middle of the life time of the sandpaper and for that reason, no direct information about the surface topography of the sandpaper at that time is available. The amplitude of the measured surface roughness is increased by a factor of $(1.18)^2 \approx 1.4$ to take into account that the roughness amplitude likely was larger at the time of the tyre dynamics measurements.

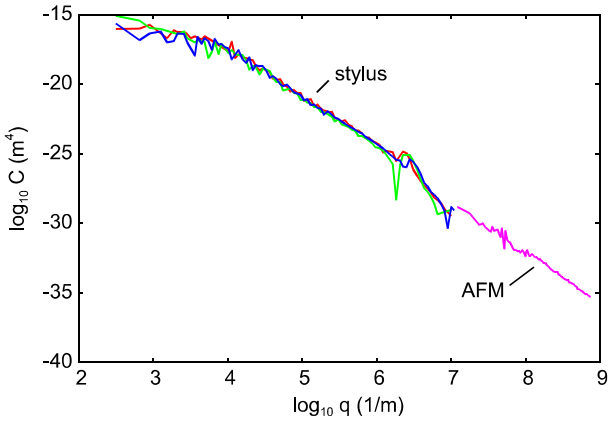

Figure 7.6: The power spectrum for corundum P80 sandpaper, as a function of the wavevector q

Figure 7.6 shows the surface roughness top power spectrum of the corundum P80 sandpaper, calculated from the measured surface height profile on a $\log_{10}$-$\log_{10}$ scale. The long wavelength roughness was probed using a stylus instrument [122] and gives the blue, green and red lines in the figure, while the short wavelength roughness was studied using atomic force microscope (AFM) [123] on top of some big corundum particles. The actual power spectrum used in the calculations was the measured one multiplied by a factor of $(1.18)^2 \approx 1.4$ to take into account the larger surface roughness expected at the time of the tyre measurements.

7.3 1D tyre model

The results presented in this section have been obtained using a 1D-model of a tyre. A tread block is attached to a tyre body block which is connected to the rim by viscoelastic springs having both elasticities and dampings. The springs have both elongation and bending elasticity k (and damping γ) which are used in longitudinal (e.g. braking) or transverse (cornering) direction.

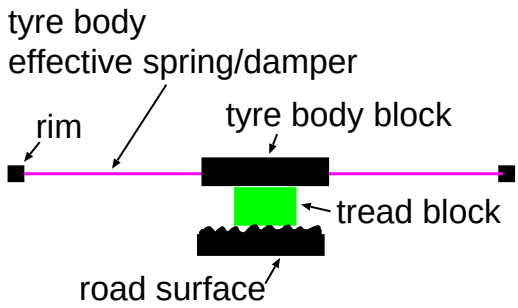

Figure 7.7: 1D-model of a tyre

The tyre-body spring constant is optimized to reproduce the tyre transverse (cornering) and longitudinal stiffness. The damping has been chosen so as to give a critical damping which gives the best agreement with the full 2D tyre model which is discussed in Chapter 7.4. That is $\gamma = 2(mk)^{1/2}$ where k is the (bending or elongation) spring constant and m the mass of the tread block plus the tyre body block. The free oscillations are determined by

$$m\ddot{u} = -ku - \gamma \dot{u} \qquad \text{(Equation 7.3)}$$

so, the damped oscillator with the complex frequency

$$\omega = i\frac{\gamma}{2\mathrm{m}} \pm \left[\frac{k}{m} - \left(\frac{\gamma}{2\mathrm{m}}\right)^2\right]^{1/2} \qquad \text{(Equation 7.4)}$$

The critical damped case is when the square-root term vanishes or $\gamma = 2(mk)^{1/2}$. The optimization of the tyre body (bending or elongation) spring constant k is done in an iterative way: first the (longitudinal and transverse) stiffness C_c for a given spring constant k is calculated and then replaced

$$k \to k \times (C / C_C)$$ (Equation 7.5)

where C is the measured (longitudinal or transverse) stiffness. After a few steps of iterations one obtains a spring constant which gives a calculated stiffness C_c which agrees well with the measured value C.

7.3.1 Numerical results and comparison to experiment

In this sub-chapter the μ-slip and μ-slipangle curves are calculated using the 1D tyre model and compared to experimental data. Chapter 7.4.3 shows that the 2D tyre model gives very similar results. However, the 2D tyre model calculations are much more time consuming and therefore it is focused on the 1D tyre model when comparing to experimental data.

Longitudinal μ-slip curve

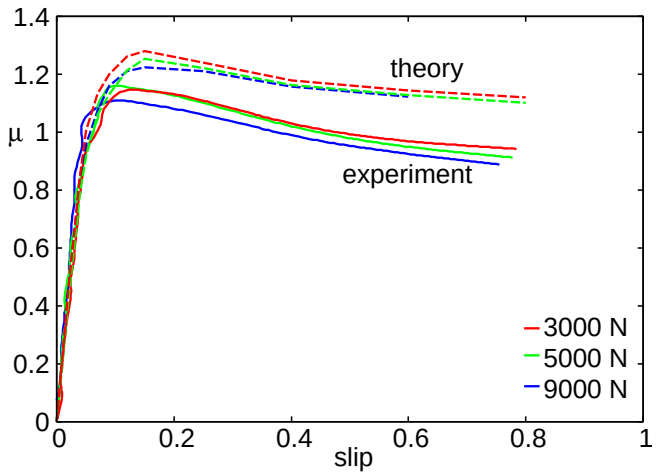

Figure 7.8: The μ-slip curve for the 1D tyre model compared with experimental data

Figure 7.8 shows the friction coefficient $\mu = F_x/F_z$ as a function of slip during braking calculated using the 1D tyre model. The car velocity v_{car} = 16.6 m/s at $T_0 \approx 37°C$ for the tyre loads F_N = 3000 N, 5000 N and 9000 N. The theoretical calculated friction coefficient is somewhat higher than found in the experiment. This may be due to inaccuracy in the surface roughness power spectrum. As pointed out in Chapter 7.2 the surface roughness profile of the sandpaper was not measured at the time the tyre measurements were done but only much later when the sandpaper

surface most likely had a modified (reduced) height profile due to wear. To account for this effect the amplitude of the surface roughness was increased by a factor of ≈ 1.18.

Another difference between the theory result and the experimental data is that the friction coefficient tends to decrease slightly faster with increasing slip in the measured data. This may be due to a temperature effect so far not included in the theory. That is, according to the theory, that an increase in the rubber temperature decreases the friction. So far the flash temperature effect is included but the fact that after some slip distance a road-rubber macroasperity contact region may move into the “hot” strip-region of rubber produced by another road asperity contact region in front of it, see Figure 7.25 is not considered. Taking into account this effect will reduce the friction for large slip and may be the reason for why the measured friction coefficient decreases faster with increasing slip than observed in the theory. Figure 7.9 shows the μ-slipangle curve (where $\mu = F_y/F_N$) for the 1D tyre model compared with experimental data for the tyre loads (a) F_N = 3000 N, (b) F_N = 5000 N and (c) F_N = 9000 N for the car velocity v_{car} = 16.6 m/s. In the calculations the background temperature T_0 has been chosen to be the same as the measured surface temperature. The tyre tread surface temperature was measured at the centre of the tyre after rotating half a full rotation out of the footprint, see Figure 7.10(b), and this temperature is taken as background temperature. Thus T_0 depends on the slipangle and on the load. Note that the temperature variation is very large, from ≈ 36°C at the smallest load and slipangle zero (start of measurement) to ≈ 75°C at the highest load and slipangle ≈ −10° (and even higher temperature for the negative slipangles which were not used in the calculations).

Transverse μ-slip curve

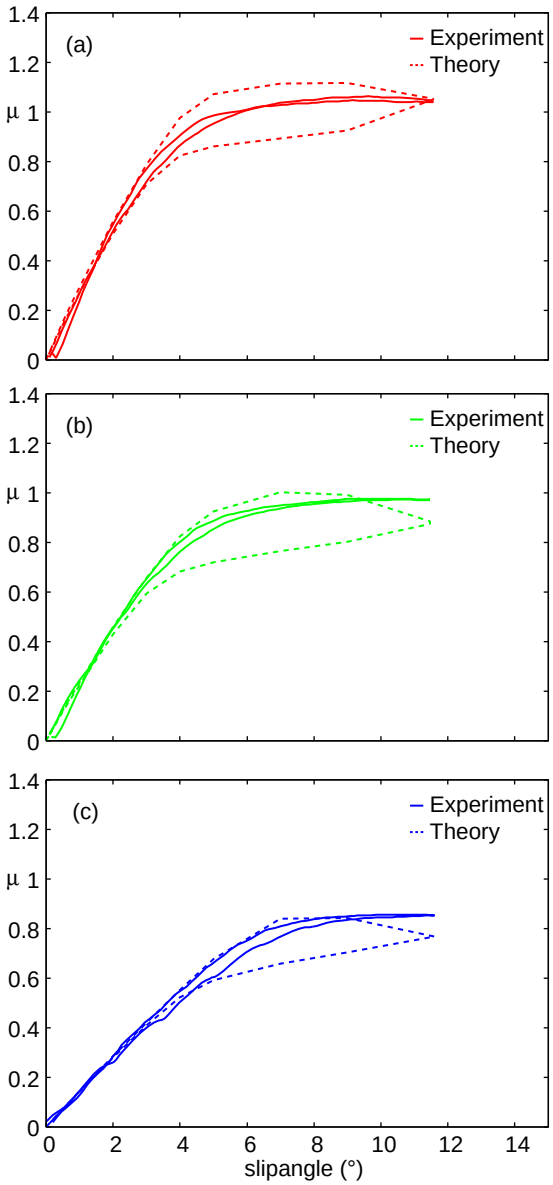

Figure 7.9: The μ-slipangle curve for the 1D tyre model compared with experimental data

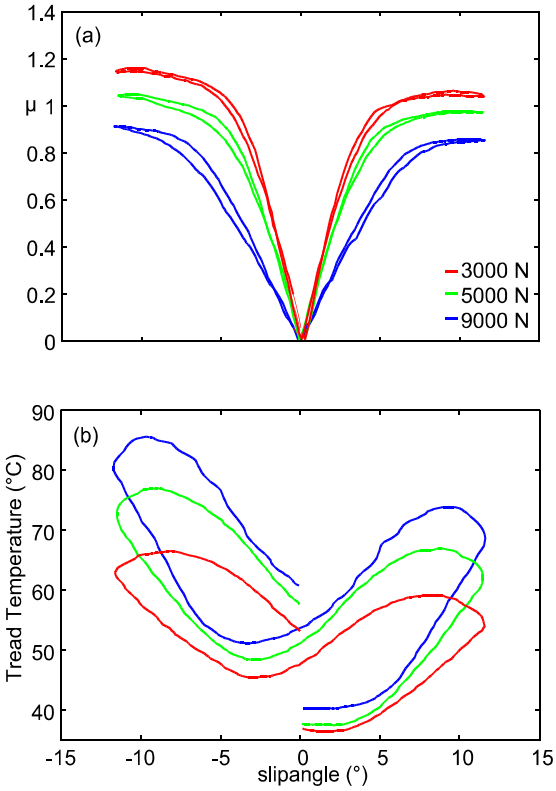

Figure 7.10: (a) The measured μ-slipangle curves, (b) the tread surface temperature

The strong increase in the temperature during cornering results in much smaller friction coefficients as compared to braking where the temperature increase is much smaller (see Figure 7.8). This is also illustrated in Figure 7.11 which reproduces the results from Figure 7.9(b) and also shows the calculated friction coefficient assuming the same temperature as in the calculation of the longitudinal μ-slip curve in Figure 7.8. In Figure 7.11 is the tyre load F_N = 5000 N and the background temperature was fixed at 37.7°C. At the lower curve the background temperature varied between 30°C and 70°C (from Figure 7.10(b)).

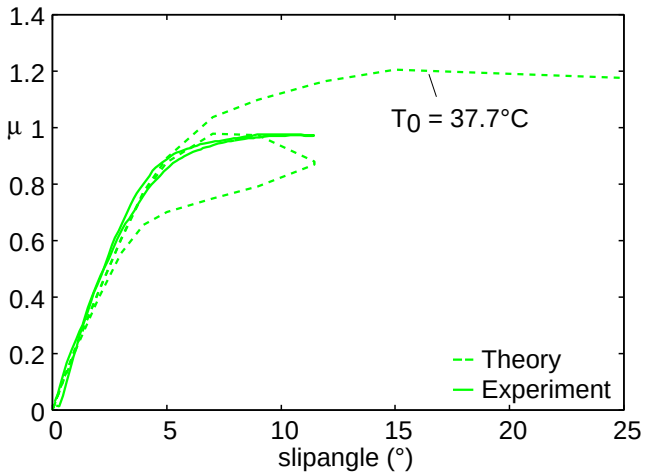

Figure 7.11: The lateral μ-slip curve for the 1D model compared with the experimental results

The used background temperature in the study above is only in an approximate way. First, it is the measured surface temperature which may differ from the temperature inside the rubber (in the surface region) which is the relevant temperature for rubber friction. In addition, it is the temperature at one spot on the tyre which may differ from other surface areas depending on where most of the friction energy is produced (which depends on the tyre-road footprint pressure distribution and hence on the tyre load). Finally, it is the temperature after half a tyre rotation while the relevant temperature is the temperature after one tyre rotation, i.e., just when a tread block enters the contact region, again.

The calculated results in Figure 7.9 exhibit a stronger variation with the load than found in the experiment. Also the hysteresis between increasing and decreasing slipangle is larger in the theory predictions than in the observations in the experiments. In the theory the hysteresis is entirely due to the change in the background temperature. Thus, the difference between theory and experiment may reflect uncertainty in $T_0(t)$ as discussed above. However, there may be another effect related to rubber wear and contamination of the road track, discussed in the following.

7.3.2 Discussion

Figure 7.10(a) shows the measured μ-slipangle curves for the tyre loads F_N = 3000 N, F_N = 5000 N and F_N = 9000 N. In the experiment the slip angle has been changed by 2° (or −2°) per second. It was first changed from 0° to +12°, then to −12°, and then back to 0°. During this cycle the tyre temperature varies as shown in Figure 7.10 (b), where the tyre tread surface temperature is shown, measured in the centre of the tyre after half a tyre rotation. As anticipated, the tyre temperature is higher for negative slip angles than for positive slipangles due to increased time of frictional heating (the cornering angle first goes positive and then negative). One remarkable effect is that the rubber-road friction is larger for negative slipangles as for positive slipangles in spite of the higher temperature for negative slipangles. The reason for why the hysteresis in the friction is larger in the calculations compared with the experiments, may be due to contamination of the road surface by hot rubber fragments (smear) which may continuously increase the contribution to the friction from the area of real contact. This effect is known to occur on Formula 1 race tracks, but may also occur in these indoor experiments due to high temperature and sever wear.

7.4 2D tyre model

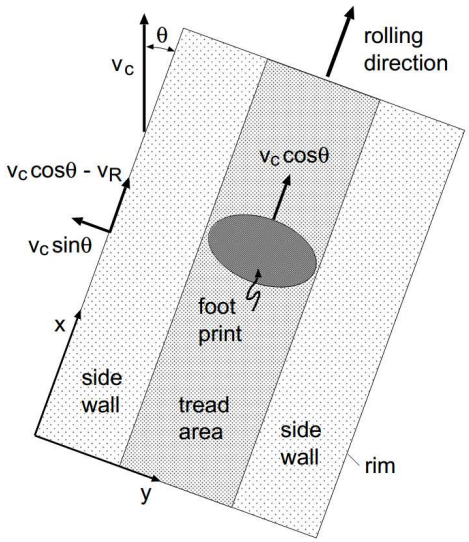

Figure 7.12: Schematically the 2D-model of a tyre

The used 2D-model is shown schematically in Figure 7.12. The car velocity v_c points in another direction than the rolling direction, resulting in a non-zero cornering angle θ. A coordinate system with the y-axis in the transverse direction and the x-axis along the longitudinal rolling direction is introduced. The road is considered as stationary. The car velocity $v_c(t)$, the rolling velocity $v_R(t)$ and the cornering angle θ(t) determine the transverse $v_y(t)$ and longitudinal $v_x(t)$ velocities of the rim:

$$v_y = v_c \sin\theta \qquad \text{(Equation 7.6)}$$

$$v_x = v_c \cos\theta - v_R \qquad \text{(Equation 7.7)}$$

The longitudinal slip s(t) is determined by

$$s = \frac{v_x}{v_c \cos\theta} = \frac{v_c \cos\theta - v_R}{v_c \cos\theta} \qquad \text{(Equation 7.8)}$$

When the cornering angle θ = 0, the equation simplifies to

$$s = \frac{v_c - v_R}{v_c} \qquad \text{(Equation 7.9)}$$

The slip s(t) and the cornering angle θ(t) depend upon the time t for non-stationary tyre dynamics. The footprint moves in the rolling direction with the rolling velocity $v_c\cos\theta - v_x = v_R$ relative to the rim and with the velocity $v_c\cos\theta$ relative to the road.

The tyre body is described as a set of mass points connected with viscoelastic springs with the elasticity k and the viscous damping γ. The springs have both elongation and bending elasticity. They are denoted by k and $k_B = k'$, and the corresponding viscous damping coefficients γ and $\gamma_B = \gamma'$. There are N_x and N_y tyre body blocks assumed along the x- and y-directions with $x_{ij} = (x_{ij}, y_{ij})$ denoting the displacement vector of the tyre body block (i, j) (i = 1, ..., N_x, j = 1, ..., N_y). As the tyre is a torus shaped object, periodic boundary conditions are used in the x-direction so that $x_{N_x+1,\,j} = x_{1,\,j}$ and $y_{N_x+1,\,j} = y_{1,\,j}$

The following boundary conditions apply. For i = 0, ..., N_x + 1:

$$\dot{y}_{i0} = v_y\,, \qquad \dot{x}_{i0} = v_x$$

$$\dot{y}_{i,\,N_y+1} = v_y, \quad \dot{x}_{i,\,N_y+1} = v_x \qquad \text{(Equation 7.10)}$$

For stationary tyre motion these Equations can be reduced to:

$$y_{i0} = v_y t\,, \qquad x_{i0} = v_x t$$

$$y_{i,\,N_y+1} = v_{yt}\,, \quad x_{i,\,N_y+1} = v_x t \qquad \text{(Equation 7.11)}$$

For j = 1, ..., N_y the periodic boundary conditions are:

$$y_{N_x+1,\,j} = y_{1\mathrm{j}}\,, \quad x_{N_x+1,\,j} = x_{1\mathrm{j}}$$

$$y_{0\mathrm{j}} = y_{N_x,\,j}\,, \qquad x_{0\mathrm{j}} = x_{N_x,\,j} \qquad \text{(Equation 7.12)}$$

If the mass of a tyre body element (i, j) is denoted by m_j, one obtain for i = 1, ..., N_x, j = 1, ..., N_y:

$$m_j \ddot{y}_{iJ} = F_{yij} + k_{yj}(y_{i,\,j-1} - y_{ij}) + k_{yj+1}(y_{i,\,j+1} - y_{ij}) + \gamma_{yj}(\dot{y}_{i,\,j-1} - \dot{y}_{ij})$$

$$+ \gamma_{yj+1}(\dot{y}_{i,\,j+1} - \dot{y}_{ij}) + k'_{xj}(y_{i+1,\,j} + y_{i-1,\,j} - 2y_{ij}) + \gamma'_{xj}(\dot{y}_{i+1,\,j} + \dot{y}_{i-1,\,j} - 2\dot{y}_{ij}) \qquad \text{(Equation 7.13)}$$

$$m_j \ddot{x}_{iJ} = F_{xij} + k_{xj}(x_{i-1,\,j} - x_{ij}) + k_{xj}(x_{i+1,\,j} - x_{ij}) + \gamma_{xj}(\dot{x}_{i-1,\,j} - \dot{x}_{ij}) + \gamma_{xj}(\dot{x}_{i+1,\,j} - \dot{x}_{ij})$$

$$+ k'_{yj}(x_{i,\,j-1} - x_{ij}) + k'_{yj+1}(x_{i,\,j+1} - x_{ij}) + \gamma'_{yj}(\dot{x}_{i,\,j-1} - \dot{x}_{ij}) + \gamma'_{yj+1}(\dot{x}_{i,\,j+1} - \dot{x}_{ij}) \qquad \text{(Equation 7.14)}$$

In the equations above, F_{xij} and F_{yij} are the force components in the x- and y-directions. They are acting on the tyre body block (i, j) of the tread block (i, j). Therefore, $F_{ij} = (F_{xij}, F_{yij})$ is only nonzero when (i, j) is in the tyre tread area. In total, eight parameters have been optimized. Namely the tyre body viscoelastic spring parameters (k, γ) and (k′, γ′) in the tread area and in the side wall area. This is done in order to reproduce a number of measured tyre properties, e.g. the longitudinal and transverse tyre stiffness values for three different loads and also the frequency and damping of the lowest longitudinal and transverse tyre vibrational modes. The vibrational modes are shown in Figure 7.13. The optimization is performed by using the amoeba method of multidimensional minimization [124].

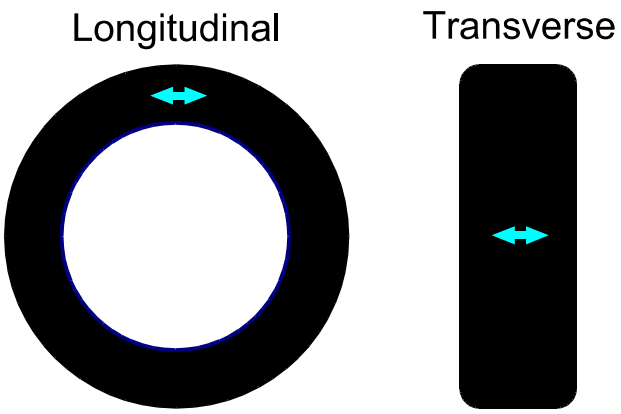

Figure 7.13: The longitudinal and transverse tyre vibrational modes of an unloaded tyre with fixed rim

7.4.1 Tyre body optimization

As discussed above, there are 16 unknown parameters which need to be determined. 10 out of these 16 parameters can be deduced. However, 6 parameters need to be imposed in order to get all quantities defined. If Q denotes the ratio of the width of the tyre body side wall block and the width of the tyre body tread area block then these conditions are:

On the side wall:

$$\gamma_x = \gamma_y Q^2, \qquad \gamma'_x = \gamma'_y Q^2 \qquad \text{(Equation 7.15)}$$

In the tread area:

$$\gamma_y = 2\gamma_y(1)Q, \quad \gamma'_x = 2\gamma'_x(1)/Q \qquad \text{(Equation 7.16)}$$

$$\gamma'_y = 2\gamma'_y(1)Q, \quad \gamma_x = 2\gamma_x(1)/Q \qquad \text{(Equation 7.17)}$$

where $\gamma_y(1)$, $\gamma'_y(1)$, $\gamma_x(1)$ and $\gamma'_x(1)$ all refer to the side wall. Note that γ_y and γ'_y are fitted to agree with the damping constant of the tyre transverse and longitudinal mode vibrations. The factor of 2 in the equations above are quite arbitrary but reflects larger damping of the tyre body in the tread area.

The tyre optimization is done in an iterative way. First the measured tyre vibration frequencies and damping constants are used to determine the tyre body spring constants and damping in a similar way as for the 1D tyre. That is, for all tyre body spring and damping constants (on both side wall and tread area) during the iteration it is replaced

(a) for transverse mode:

$$k_y \rightarrow k_y \times (\omega_T/\omega_{Tc})^{2,} \qquad \gamma_y = \gamma_y \times (\gamma_T/\gamma_{Tc}) \qquad \text{(Equation 7.18)}$$

(b) for longitudinal mode:

$$k'_y \rightarrow k'_y \times (\omega_L/\omega_{Lc})^{2,} \qquad \gamma'_y = \gamma'_y \times (\gamma_L/\gamma_{Lc}) \qquad \text{(Equation 7.19)}$$

The iteration is continued until the measured tyre vibration frequencies ω_T and ω_L and damping γ_T and γ_L are reproduced.

Next the tyre longitudinal and transverse stiffness values for 3 loads (total 6 parameters) are used as follows:

Transverse stiffness: In the tread area k_y, k'_x are varied and also in the side wall k'_x.

Longitudinal stiffness: In the tread area k'_y, k_x are varied and also in the side wall k_x.

The optimization of the transverse and longitudinal tyre stiffness for all three tyre loads using the amoeba method to minimize the effective potential or error functions:

$$V_T = \left[\sum \left(\frac{C_T}{C_{Tc}} - 1 \right)^2 \right]^{1/2}, \qquad V_L = \left[\sum \left(\frac{C_L}{C_{Lc}} - 1 \right)^2 \right]^{1/2} \qquad \text{(Equation 7.20)}$$

where C_T is the measured tyre stiffness and C_{Tc} the calculated (for a given set of spring constants and damping) transverse stiffness value, and similar for the longitudinal stiffness C_L and C_{Lc}. The tyre stiffness values are defined as $C_T = F_y/(\theta F_N)$ (where θ is in degree) as the slipangle $\theta \rightarrow 0$ and $C_L = F_x/(sF_N)$ as the slip $s \rightarrow 0$. The sum $\sum$ is over the three different tyre loads. In Table 7.1 and 7.2 the results of a tyre optimization are shown. The longitudinal and transverse tyre vibrations and dampings are perfectly reproduced. The transverse (cornering) stiffness is also very well reproduced. However, the longitudinal stiffness for the largest load shows some discrepancy. Table 7.3 also presents several other calculated quantities for which no measured values were known. The pneumatic trail is defined as M_z/F_y and the self aligning moment stiffness is defined as $M_z/(\theta F_N)$ as the slipangle $\theta \rightarrow 0$. Finally, the camber stiffness coefficient is defined as $F_y/(\varphi F_N)$ as the camber angle (in degree) $\varphi \rightarrow 0$. For the loads F_N = 3000 N, 5000 N and 9000 N the length of the tyre footprint is L_x = 90 mm, 128 mm and 189 mm, respectively. Thus the ratio between the pneumatic trail δ (see Table 7.3) and the length of the footprint are δ/L_x = 0.21, 0.27 and 0.28 respectively. The simple brush model predict $\delta/L_x = 1/6 \approx 0.17$, but it is known from measurements that the pneumatic trail usually is larger than predicted by the brush model, in accordance with the model predictions.

	ω_T (Hz)	γ_T (s^{-1})	ω_L (Hz)	γ_L (s^{-1})
calculated	46.1	1.10	63.0	2.72
experimental	46.2	1.10	63.0	2.72

Table 7.1: The calculated (optimized) and experimental values for the longitudinal and transverse tyre vibration eigenfrequencies and dampings.

F_N (N)	C_T	C_{Tc}	C_L	C_{Lc}
3000	0.31	0.30	25.0	26.3
5000	0.23	0.21	22.5	21.5
9000	0.14	0.14	22.0	16.2

Table 7.2: The calculated (optimized) and experimental values for the longitudinal and transverse stiffness for the three different normal loads.

F_N (N)	Pneumatic trail (mm)	Self-aligning moment stiffness coefficient	Camber moment stiffness coefficient
3000	18.9	0.0057	0.0094
5000	34.2	0.0071	0.0093
9000	53.3	0.0077	0.0112

Table 7.3: The values for the pneumatic trail, the self-aligning moment stiffness coefficient and the camber stiffness coefficient after the tyre optimization for the three different normal loads.

The tyre body elasticity and damping for square tyre-body elements as resulted from the tyre optimization are shown in Table 7.4 and 7.5.

location	k_x (kN/m)	k_{Bx} (kN/m)	k_y (kN/m)	k_{By} (kN/m)
side wall	141.1	68.0	11.6	22.5
tread area	223.4	102.4	105.6	56.6

Table 7.4: The calculated (optimized) tyre-body spring constants.

location	γ_x (Ns/m)	γ_{Bx} (Ns/m)	γ_y (Ns/m)	γ_{By} (Ns/m)
side wall	0.736	2.015	0.700	2.088
tread area	1.472	4.030	1.400	4.175

Table 7.5: The calculated (optimized) tyre-body damping constants.

Note that the side wall spring constants k_y and k_{By} are considerably softer than the other spring constants. In Chapter 7.4.3 it is shown that these spring constants are determined mainly by the inflation pressure. Note also that, as expected, the spring constants of the tyre body in the tread area are higher than in the sidewalls. Consider a rubber block with thickness d and the width and height b. If the stress $\sigma = F/bd$ is applied to two opposite sides it will elongate a distance u so the strain $\varrho = u/b$ (see Figure 7.14).

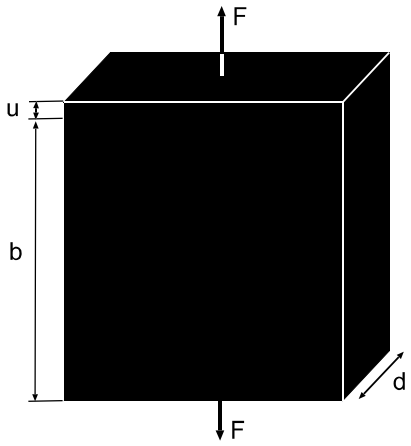

Figure 7.14: A rubber block sheet of square form (side b) and thickness d exposed to a uniform stress σ = F/db will elongate a distance u

If E is the elastic modulus one have σ = Eǫ which gives F = uEd or the elongation spring constant k = Ed. Similar the shear spring constant k_B = Gd (where G = E/(2(1 + ν)) is the shear modulus. If the thickness of the rubber block d = 1 cm as typical for tyre body and if E = 10 MPa as is typical for the low-frequency Young's modulus of filled rubber, one get k = 100 kNm and k_B ≈ 30 kNm. These values are similar but slightly smaller than the values given in Table 7.4. This is expected, as in the tyre body are fibers with much higher stiffness than the rubber itself. Note, as pointed out above, that the side wall spring constants k_y and k_{By} are considerably softer than the other spring constants and also smaller than estimated above for a rubber block. The reason is that in the model these two spring constants have a geometrical origin in combination with the inflation pressure, see Chapter 7.4.3. Calculations of the tyre body longitudinal and transverse stiffness are performed neglecting the deformations of the tread blocks. In this case the tyre stiffness values are entirely due to the deformations of the tyre body. It is found that neglecting the deformations of the tread blocks increases the tyre longitudinal stiffness by ≈ 18% and the transverse tyre stiffness by ≈ 8%. In addition to the longitudinal and transverse tyre stiffness obtained from the μ-slip and μ-cornering-angle curves it is also the longitudinal (K_L) and transverse (K_T) stiffness measured defined as follows. The tyre is pushed against a substrate with a given load and a tangential force

F is applied while the tangential tyre displacement u from the centre axis is measured. The tyre is not allowed to rotate. In this way a u(F) curve is obtained which is nearly linear up to the point when the tyre starts to slip. It is $K_L = F_x/u_x$ and $K_T = F_y/u_y$ defined.

In Figure 7.15 the measured and calculated relation between F/F_N is shown and the longitudinal and transverse tyre displacement. For the longitudinal stiffness (left) K_L for the drive velocity v = 2.2 mm/s and the lateral stiffness K_T for the drive velocity v = 6.45 mm/s and the tyre load F_N = 5000 N.

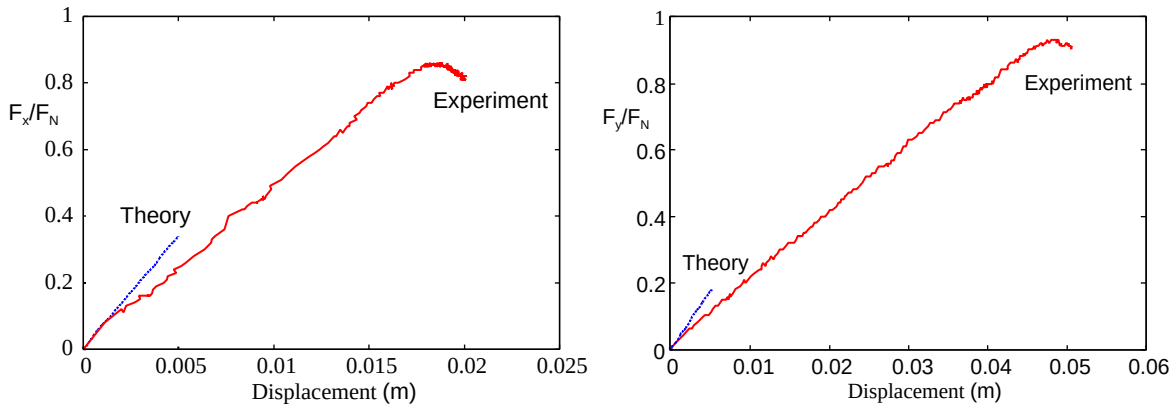

Figure 7.15: The calculated and experimental results for the longitudinal stiffness (left) K_L and the lateral stiffness K_T

Figure 7.16 shows the calculated results for K_L and K_T for three different loads and the corresponding measured data for two loads. While the trend in the data as a function of the normal load are the same there are some quantitative differences. The calculated stiffness values are higher than measured. The origin of this may reflect uncertainties in the experimental data used in the optimization of the tyre body, in particular in the tyre resonance frequency ω_T and ω_L.

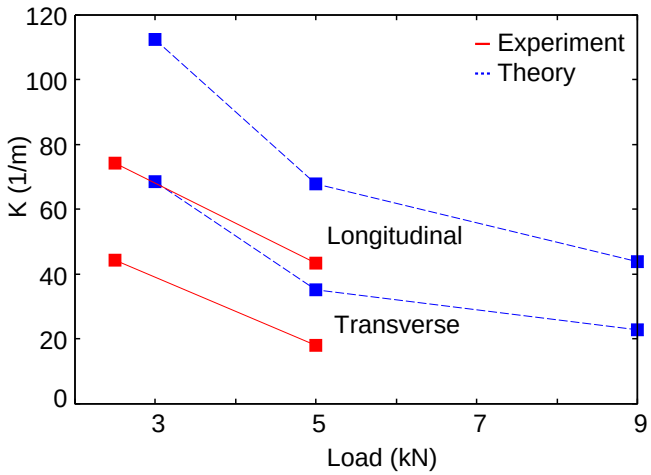

Figure 7.16: The calculated results for the stiffness parameters K_L and K_T

7.4.2 Tyre footprint pressure distribution

In the tyre dynamics calculations the measured tyre footprint pressure distribution are used shown in Figure 7.17 for the normal loads (a) F_N = 3000 N, (b) F_N = 5000 N, and (c) F_N = 9000 N. The tyre model does not use the exact tread pattern from the real tyre, but assumes square tread blocks. By processing the pressure profiles shown in Figure 7.17 so that the tread blocks experience contact pressures with a very similar spatial distribution as the measured footprint pressure distribution. Also note that the pressure profiles in Figure 7.17 refer to static condition. During rolling, braking and cornering the pressure distribution will be modified but this effect is not taken into account in the present study.

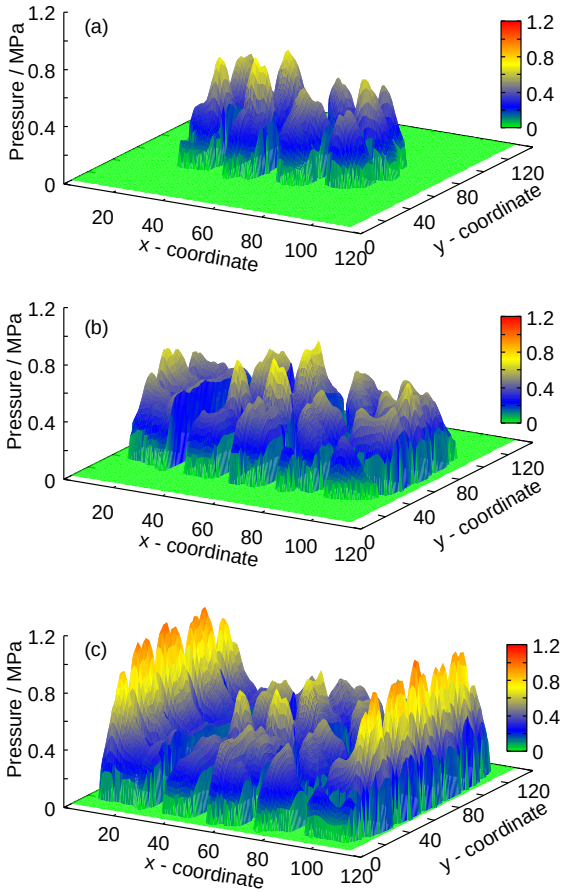

Figure 7.17: The tyre footprint pressure distribution for the three normal loads

7.4.3 Numerical results

In this section the µ-slip curves calculated with the 2D-tyre model are compared with the 1D-tyre model. Additionally the calculated self aligning moment curve with experimental data is compared. Finally snapshot pictures of the tyre deformation field during braking and cornering are presented.

Comparison with the 1D model

In Figure 7.18 the longitudinal µ-slip curve for the 1D and 2D-tyre models are compared to the experimental result for the tyre load F_N = 5000 N. Note that the 1D and 2D-tyre models give very similar results.

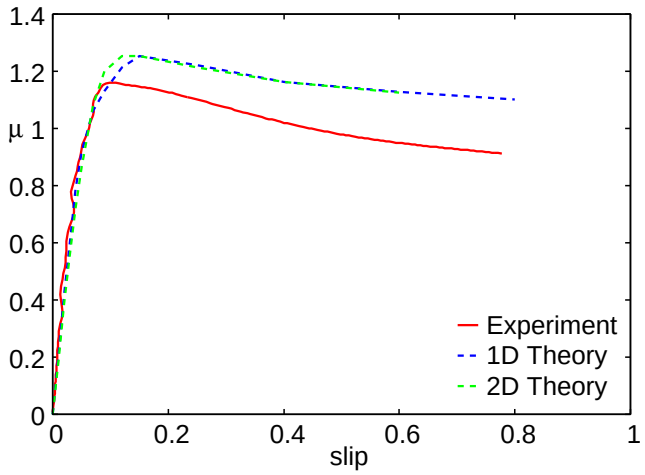

Figure 7.18: The longitudinal μ-slip curve for the 1D and 2D model compared with the experimental results

Self aligning torque: comparison with experiment

Figure 7.19 shows the self-aligning moment as a function of the slipangle for the tyre load F_N = 3000 N, F_N = 5000 N and F_N = 9000 N. The measured result is given by the solid line and the prediction of the 2D-tyre model by the dashed line. Note that the maximum of the measured self-aligning moment is larger than predicted theoretically.

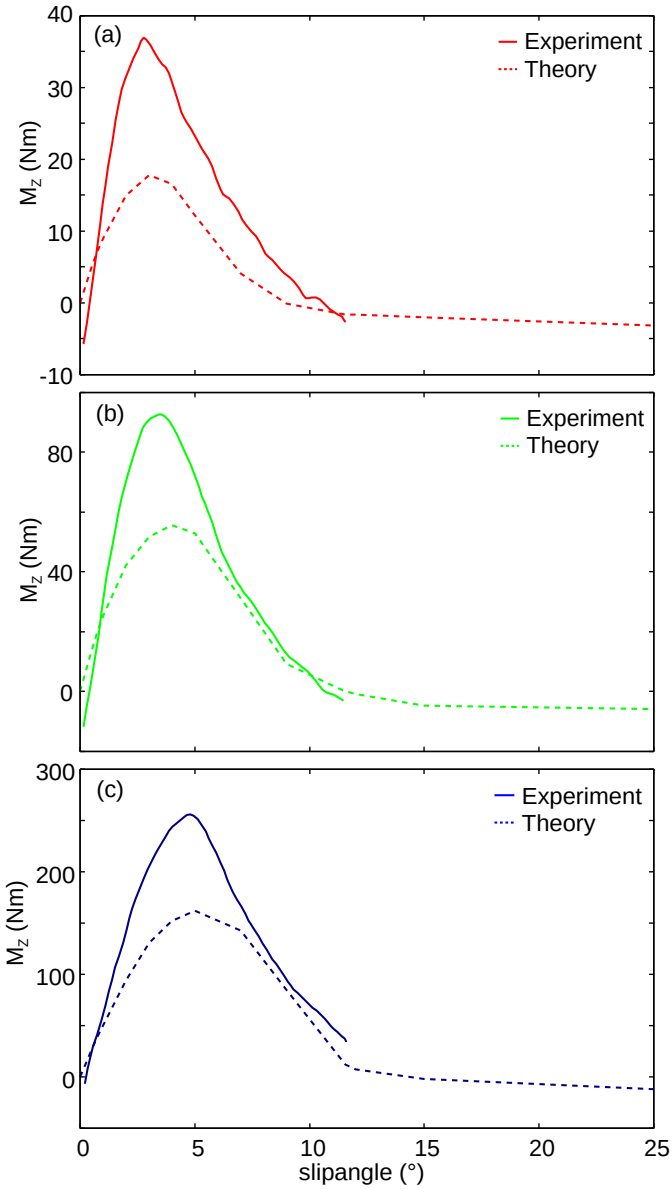

Figure 7.19: The self-aligning moment as a function of the slipangle

Relaxation length

Figure 7.20 shows the variation of the transverse force on the tyre (in units of the normal force F_N) as a function of time when the cornering angle increases linear with time from $\theta_0 = 0°$ at time $t_0 = 0$ to $\theta_1 = 1°$, 3°, 7° and 12° at $t_1 = 0.02$s. The relaxation length L is the tyre rotation distance in order for the transverse force to reach 60% of its final value. In the present case L ≈ 0.5 m for $\theta_1 = 1°$ and 3°. This corresponds to ≈ 1/4 of a full tyre rotation. For large slip angles the relaxation length is smaller, as also observed in experiments. The transverse friction force shown in Figure 7.20 as a function of time exhibit high-frequency oscillations with the frequency f_0 ≈ 500 Hz. These oscillations reflect the variation of the number of tread blocks in the tyre-road footprint. In the model, where the tread blocks are considered as mass points, there will be fluctuations in the friction force as the number of tread blocks in the footprint varies. If d is the distance (in the x-direction) between the centre of mass of two nearby tread blocks, then the period of the oscillations in the force will be T = d/v. In the present case v = 16.6 m/s and d ≈ 3 cm giving a fluctuation frequency $f_0 = 1/T$ ≈ 500 Hz. The variation in the amplitude of the fluctuations with differnet slipangle may result if the driving frequency f_0 becomes close to some short-wavelength tyre vibration eigenmode, localized to the vicinity of the contact patch. The frequency f may depend on the tyre deformation which depends on the cornering angle.

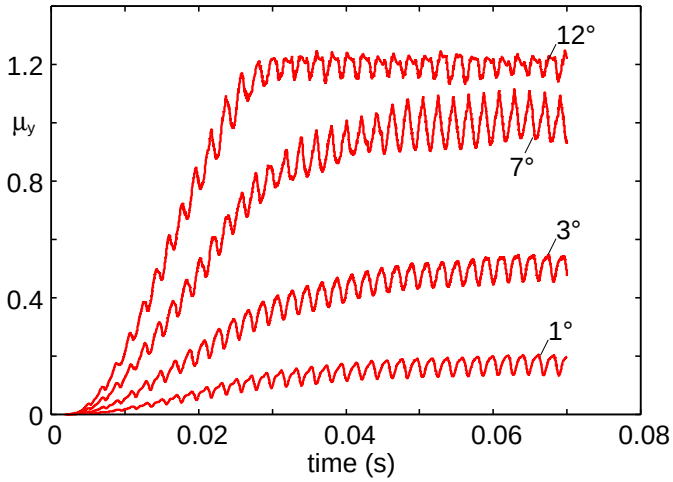

Figure 7.20: The variation of the transverse force on the tyre (in units of the normal force F_N) as a function of time

Tyre body deformation field

Figure 7.21 shows snapshot pictures of the tyre deformation field during braking (left) and cornering (right) for the rubber background temperature T_0 = 80°C and the car velocity 16.6 m/s. For braking in all cases the slip s = 0.05 and the cornering angle θ = 0. The short vertical lines indicate the displacement of the tyre body from the undeformed state. The maximum tyre body displacements are 0.92, 1.39 and 1.84 cm.

For cornering in all cases the slip s = 0 and the cornering angle θ = 5°. The short horizontal lines indicate the displacement of the tyre body from the undeformed state. The maximum tyre body displacements are 1.20, 1.81 and 2.31 cm.

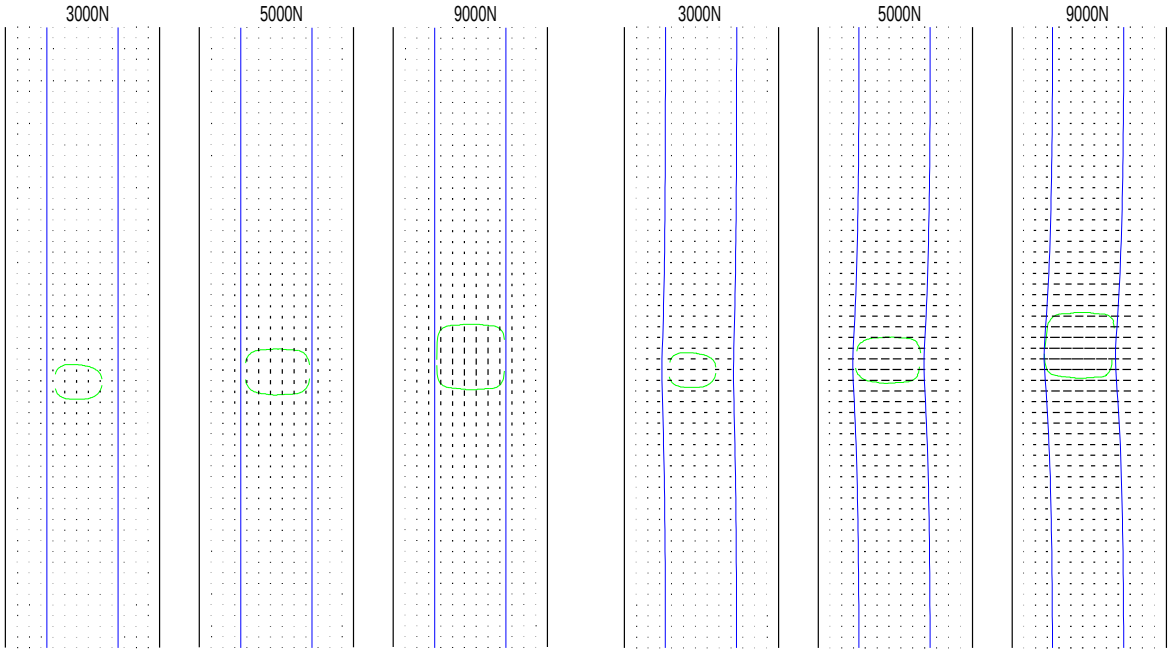

Figure 7.21: Snapshot pictures of the tyre body deformations

Influence of tyre gas (inflation) pressure

The inflation pressure has two (related) influences on the tyre dynamics: increasing the inflation pressure will (a) increase the tyre body stiffness, which will increase the longitudinal and transverse (cornering) tyre stiffness, and (b) will reduce the length of the tyre footprint which will reduce the longitudinal and transverse (cornering) tyre stiffness. For vehicle tyres these two effects nearly cancel each other resulting in only a small change in the tyre stiffness which could be either a positive or negative sign, depending upon which effect is stronger.

In a first approximation the normal pressure in the footprint is given by the inflation pressure (this would hold exactly for a membrane without bending stiffness) and the area of the footprint would be proportional to the inflation pressure. In this case, if both the width and the length of the footprint would change with an equal factor, then the length $L_x \sim p^{1/2}$. If the width would instead be constant (as it must be the case for small inflation pressures or large tyre loads) then $L_x \sim p$.

Increasing the inflation pressure will result in a stiffening of the tyre side walls which can be understood as follows. Assume for simplicity that the tyre cross section is rectangular with the tread area of width w, and the side wall of width h, see Figure 7.22. Applying a transverse force uniformly on the tread area deforms the tyre body which is assumed as indicated in Figure 7.22. This will in first approximation change the volume of the gas contained in the tyre by $\Delta V = Lwh - Lwh\cos\alpha \approx Lwh\alpha^2/2$ resulting in a work done against the gas pressure by $p\Delta V$. In the tyre model it does not account for the inflation pressure explicitly, so this effect of the gas in the tyre must be contained in the tyre springs used in the model (see Chapter 7.4). In the 2D-tyre model the tyre body is discredited into square blocks of width a in the tread area, and into rectangular blocks on the side walls with length $b_x = a$ and width b_y. Thus, if there are N_y blocks in the y-direction, $N_y b_y = h$, and if L is the length (x-direction) of the 2D-tyre then $N_x b_x = L$. The transverse tyre deformations involve only the side wall springs k_y. In the model the deformation in Figure 7.22 moves the tread area relative to the (fixed) rim in the transverse direction by the amount $h\sin\alpha \approx h\alpha$ so that each spring will elongate (on one side) or contract (on the other side)

with $b_y\alpha$. If the total number of side wall springs k_y is denoted by $N = 2N_xN_y$ then one gets the energy conservation equation:

$$\frac{1}{2}Nk_y(b_y\alpha)^2=\frac{1}{2}N\,k_y^0(b_y\alpha)^2+p\Delta V \qquad \text{(Equation 7.21)}$$

where k_y^0 is the tyre k_y-spring constant for zero inflation pressure. Thus:

$$k_y=k_y^0+p\,Lwh/(2N_x N_y b_y^2) \qquad \text{(Equation 7.22)}$$

or

$$k_y=k_y^0+(pw/2)(b_x/b_y) \qquad \text{(Equation 7.23)}$$

Applying instead an uniform longitudinal force on the tread area, and using the same arguments as above, one can show that:

$$k_{By}=k_{By}^0+(pw/2)(b_x/b_y) \qquad \text{(Equation 7.24)}$$

Thus one expect k_y and k_{By} to depend linearly on the inflation pressure. However the prefactor will not be exactly $(w/2)(b_x/b_y)$ because the undeformed tyre-body will not be exactly rectangular as assumed above, and the deformed tyre body will not involve just the simple shear deformation indicated in Figure 7.22.

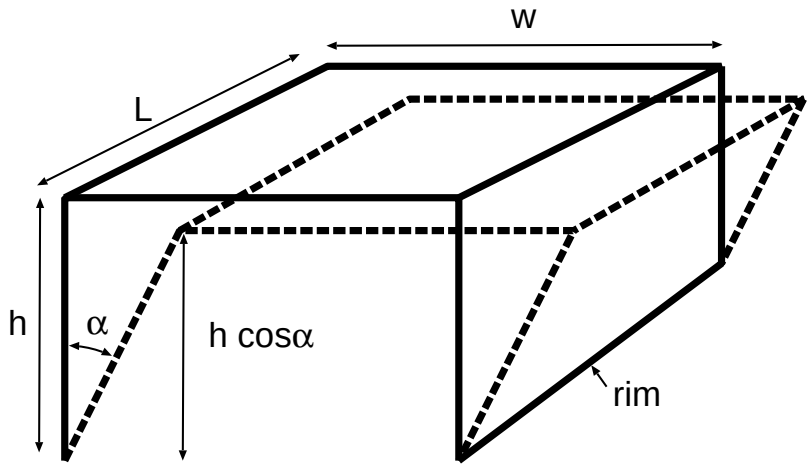

Figure 7.22: An uniform transverse force acting on the tyre tread area deforms the tyre body

It is assumed that at the nominal inflation pressure the pressure term in brackets will dominate over k_y^0 (and similar for k_{By}), and in the model calculations the pressure independent term is neglected. This is intuitively clear since it is much easier to displace the tread area of an uninflated tyre than of an inflated tyre. Note that in the present case (where p = 0.25 MPa, w ≈ 0.18 m and $b_x/b_y \approx 0.8$) this would give a pressure contribution to k_y of about $\approx 1.3\times10^4$ Nm and similar for k_{By}. This is remarkable close to the the spring constants obtained for the optimized tyre which are $k_y \approx 1.0 \times 10^4$ Nm and $k_{By} \approx 1.8 \times 10^4$ Nm, respectively. Also note that all the other spring constants of the optimized tyre are much larger, so in these cases the dependency of the spring constants on the inflation pressure will be smaller. However, it is found that k_y and k_{By} have very small influence on tyre longitudinal and transverse stiffness (but of course crucial for the longitudinal and transverse tyre vibration modes) so it is still important to take into account the dependency of k_x and k_{Bx} on the inflation pressure. It is expected from dimensional arguments that k_x and k_{Bx} depend on p in a similar way as k_y and k_{By} so that

$$k_{By} = k_x^0 + \alpha_x (pw/2)(b_y/b_x), \qquad k_{Bx} = k_{Bx}^0 + \alpha_{Bx}(pw/2)(b_y/b_x) \qquad \text{(Equation 7.25)}$$

where it is expected that α_x and α_{Bx} to be of order unity. Note, from dimensional arguments these numbers may depend on h/w. In the model calculations it is reported that $\alpha_x = \alpha_{Bx} = 1$ is chosen, but these parameters could in principle be determined by comparing how the calculated longitudinal and transverse tyre stiffness compares to the measured tyre stiffness for two different inflation pressures.

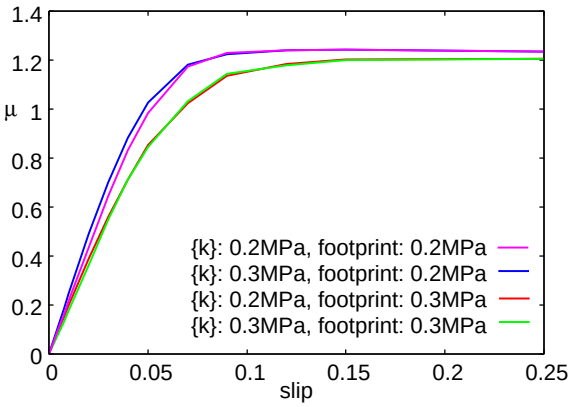

Figure 7.23: The μ-slip curve in dependency of the tyre inflation pressure

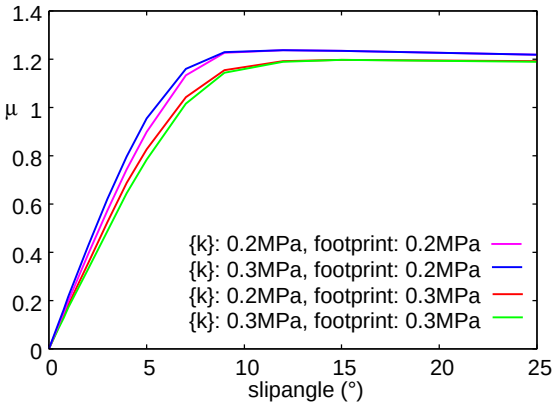

Figure 7.24: The μ-slipangle curve in dependency of the tyre inflation pressure

In Figure 7.23 and 7.24 the dependency of the μ-slip and the μ-slipangle curves on the inflation pressure is shown. 4 model calculations are done where the tyre body stiffness parameters {k} and the footprints have been modified to correspond to the inflation pressures 0.2 and 0.3 MPa. Note that in the model there is a very small influence of the tyre body stiffness on the μ-slip curve, while the μ-slip curve depends strongly on the size of the footprint. In the present calculation the normal tyre load is fixed and the footprint was taken as rectangular with equal width for the inflation pressures 0.2 and 0.3 MPa. Thus at the lower inflation pressure the footprint is 3/2 = 1.5 times longer than for the larger inflation pressure. In reality, as the inflation pressure changes, the shape of the footprint may get modified in a different way than assumed in the model calculations, but it is in principle easy to use footprints measured at different inflation pressure in the calculations.

7.4.4 Discussion

All the calculations presented above have been obtained using the 2D tyre model described in Chapter 7.4, with the tyre body optimized using experimental data for a passenger car tyre. The viscoelastic springs associated with this tyre body are kept fixed in all the calculations, except in Chapter 7.4.3 where the influence of the tyre inflation pressure is studied (which affects the tension in the tyre walls) on tyre dynamics. Thus the model calculations do not take into account the changes in the tyre body viscoelastic properties due to variations in the tyre (background)

temperature. In principle this effect can be relatively simply taken into account in the model, but has not been included so far.

It is emphasized that the 2D tyre model is not a “stationary tyre model”, but the model describes arbitrarily complex tyre dynamics, e.g. combined (time dependent) variation in the longitudinal slip, the cornering angle and the camber angle, while the (forward or rolling) velocity may depend on time in any arbitrary way. The full (time-dependent) set of equations of motion are solved numerically without any limitation. In fact, even “stationary tyre motion” involves non-steady tread block motion. Thus, at small slip a tread block entering the footprint is first (nearly) pinned to the substrate, and only close to the exit of the footprint will it undergo fast slip. Furthermore, after leaving the footprint the tread block may perform damped high-frequency vibrations for a short time (resulting in high frequency noise). This is all accurately described by the tyre model but not discussed here.

In the model the tyre is discredited into blocks. To each tyre body element in the tread area is “connected” a tread block which in turn is discredited in the vertical direction into many (typically 10) thinner block-elements (describing vertical slices of the tread block) which are coupled to each other using viscoelastic springs (corresponding to the measured viscoelastic modulus of the tread rubber). This model also allows a gradient in the tread rubber properties, as is typical in real applications, where a stiffer, less hysteritic, rubber is often used in the upper part of the tread block in order to reduce (stabilize) the deformations of the tread block when exposed to large stresses, and in order to reduce the rolling resistance. The parallel (frictional) stress, which acts on a tread block, is the product of the normal stress times the friction coefficient, which depends on the history of the sliding motion of the tread block element, as described by the theory, or by the simplified friction law given by Equation 6.27. Thus the present theory includes the memory effects of the friction force resulting from the non-uniform (in time) slip motion of the tread blocks.

The present study only accounts for frictional heating via the flash-temperature effect. In reality the background temperature T_0 may also change with time, e.g. during ABS braking, or during the measurement of the μ-slip curve. (It is well known in indoor measurements of tyre μ-slip curves that the increase in T_0 with increasing time may result in large “hysteresis” if the slip is first increased from zero to unity, and then reduced back to zero). This effect is not included so far, but it can relatively easily be taken into account in the present theory. There is also another temperature effect coming from the overlap of hot spots from different asperity contact regions which is not included in this study (see below).

The flash temperature depends on both the slip velocity and the slip distance. The amount of dissipated energy (which is the product of friction force and slip distance) goes to zero as the slip distance goes to zero so negligible frictional heating (and negligible temperature increase) of the rubber will occur when the slip distance is very small. On the other hand when the slip distance becomes larger than the diameter D of the macroasperity contact regions then there is no longer any overlap between the present (say, at time t) contact region and the original (say, at time t = 0) macroasperity contact region, and at this point the flash temperature has been fully developed. This picture neglects the fact that after long enough slip a given macroasperity contact region may overlap with the “hot rubber track” emerging from another asperity contact region in front of it. Note, this hot rubber track will widen in time due to heat diffusion, and finally (for long enough time) contribute to the background temperature $T_0(t)$, see Figure 7.25. When a rubber block slides on a rough surface the heat produced in the asperity contact regions will result in hot tracks (dotted area) on the rubber surface. When an asperity contact region moves into the hot track resulting from another asperity contact region in front of it (in the sliding direction) it will experience a rubber temperature higher than the back-ground temperature T_0. This “thermal interaction” between hot spots becomes important if the slip distance is larger than the average separation between the (macro) asperity contact regions.

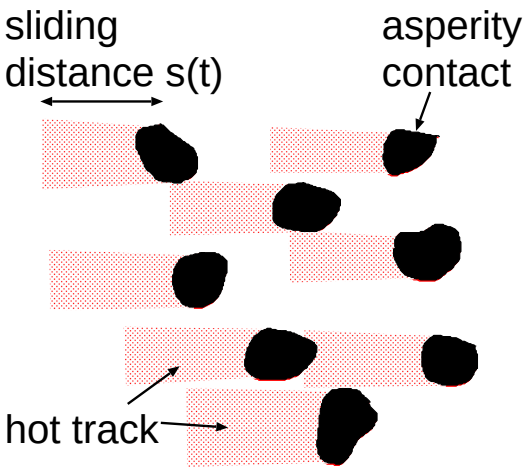

Figure 7.25: Rubber block sliding on a rough surface

This effect is also included as an option in the computer code, but was not activated in the present study as it has not been tested in detail. However, this effect is not important for slip up to (and slightly beyond) the point where the mu-slip curve has its maximum, which is the most important region of slip for practical applications (e.g. ABS braking), but will give rise to a decrease in the friction for large slip.

Chapter EIGHT

This chapter presents simulations of anti-lock braking using two different control algorithms. For the calculations, the 2D tyre model presented in chapter seven is used, and the model includes the phenomenological rubber friction law introduced in chapter six.

8. ABS braking simulations

In the following results are shown using two different control algorithms. In both algorithms, the braking torque is changed (increased or decreased) in steps of ΔM at time $t_n = n\Delta t$ (n = 1, 2, ...). The first method (a) assumes, that the maximum friction and the corresponding slip s* are both known and time independent. Thus, the braking torque is increased if the slip $s(t_n)$ at time t_n is below s* and otherwise it is decreased (see Figure 8.1).

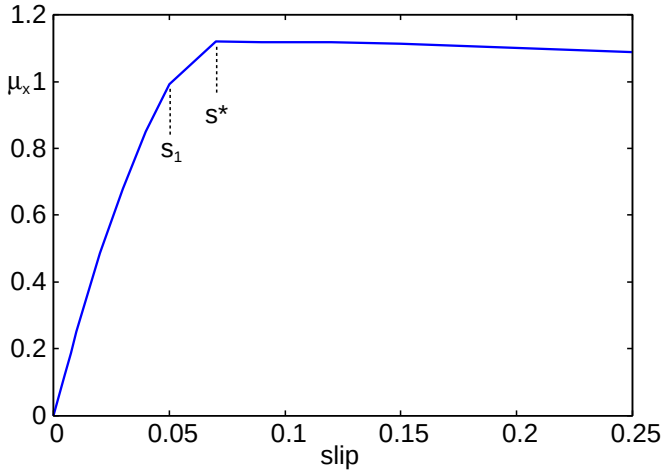

Figure 8.1: The μ-slip curve for the car velocity v_c = 27.0 m/s with the maximum slip s = s = 0.07*

One problem here is that the slip s* depends on the car velocity which changes during the braking process. However, for the system under investigation s* ≈ 0.07 is nearly independent of the car velocity for 1 m/s < v_c < 27 m/s. Note that s* depends on the background temperature T_0 which increases during braking due to the frictional heating. However, in the present study this effect is not considered.

On the second control algorithm (b), it is assumed that s* is unknown. However, by analysing the variation with time of the longitudinal friction $F_x(t)$ and the slip s(t) one can determine on what side of the maximum s* (left or right) one is. Thus, if

$$F_x(t_n) > F_x(t_{n-1}) \quad \text{and} \quad s(t_n) < s(t_{n-1}) \qquad \text{(Equation 8.1)}$$

or if

$$F_x(t_n) < F_x(t_{n-1}) \quad \text{and} \quad s(t_n) > s(t_{n-1}) \qquad \text{(Equation 8.2)}$$

implies $s(t_n) > s^*$. So, the braking torque at time t_n must be decreased, otherwise increased. Here, $F_x(t_n)$ is the longitudinal friction force and $s(t_n)$ the slip at time $t_n = n\Delta t$ (n = 1, 2, ...).

Now numerical results are presented to illustrate the two ABS braking algorithms. Denoting M as the mass-load acting on a wheel and I is the moment of inertia of the wheel without the tyre. For simplification purposes, the suspension is rigid and mass-load transfer is neglected. The motion equation for the centre of mass coordinate x(t) of the wheel and the angular rotation coordinate φ(t) are:

$$M\,\ddot{x} = F_{rim} \qquad \text{(Equation 8.3)}$$

$$I\,\ddot{\phi} = M_{rim} - M_B \qquad \text{(Equation 8.4)}$$

where F_{rim} is the force acting on the rim. M_B is the braking torque and M_{rim} the torque acting on the rim from the tyre. For constant rolling velocity $F_{rim} = F_f$ is the tyre-road friction force and $M_{rim} = RF_f$, where R is the rolling radius. But during angular accelerations, these relations are no longer true because of tyre inertia effects. In the calculations M = 360 kg and I = 0.4 kgm² are used.

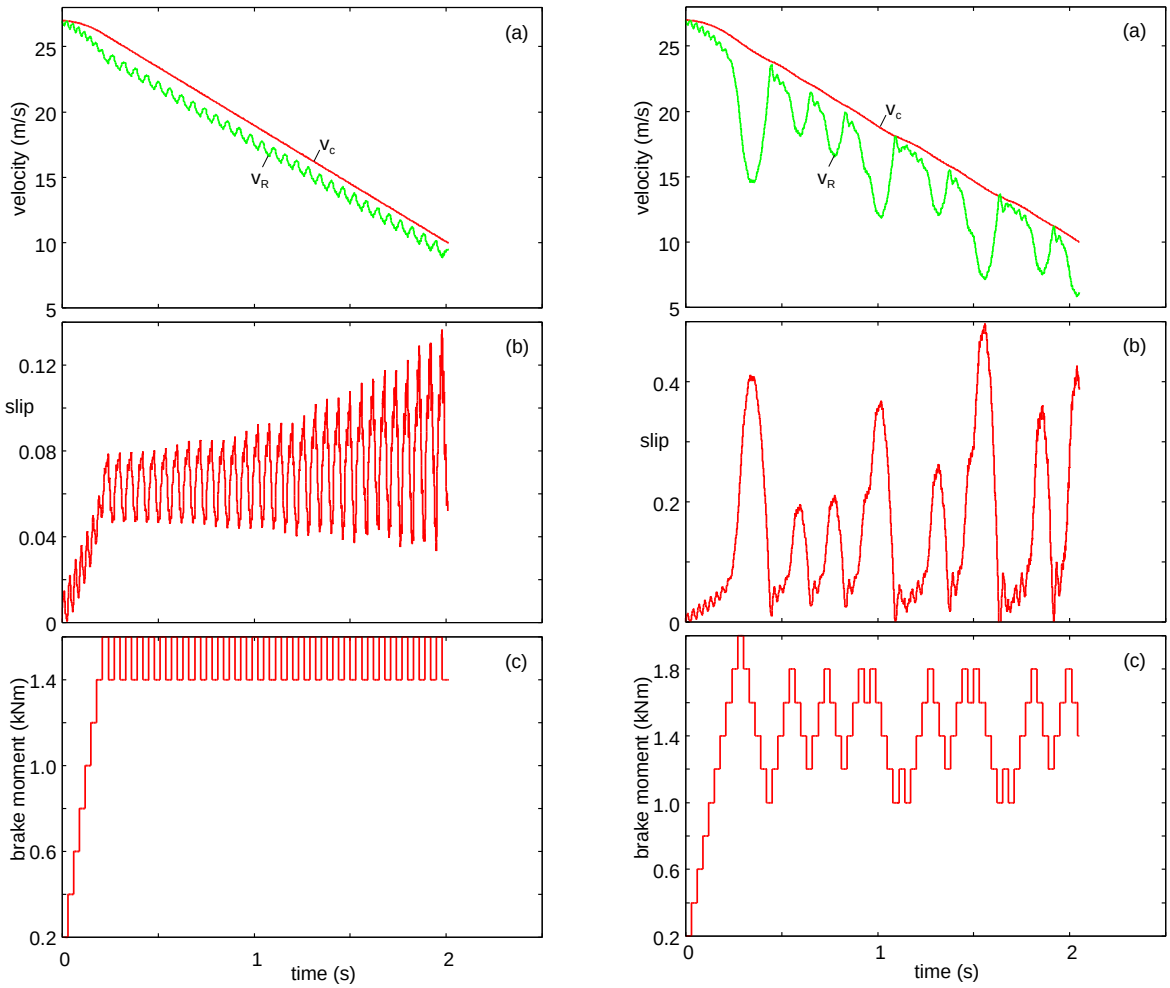

Figure 8.2: (a) The car velocity v_c and the rolling velocity v_R, (b) the slip and (c) the braking moment as a function of time t using control algorithms a (left) and b (right)

Firstly control algorithm (a) is investigated. It is assumed ΔM = 200 Nm, Δt = 0.03 sec, and $s^* \approx 0.05$ (compare Figure 8.2 left). The actual maximum of the μ-slip curve occurs for s^* = 0.07 and is discussed below the difference between using these two different values for s^*. In Figure 8.2 is (a) the car velocity v_c and the rolling velocity v_R, (b) the longitudinal slip and (c) the braking torque as a function of time shown.

The duration (t ≈ 2 sec) to reduce the car velocity from v_0 = 27 m/s to v_1 = 10 m/s corresponds to an effective friction coefficient $\mu = (v_0 - v_1)/gt = 0.87$ which is smaller than the actual maximum of the μ-slip curve. The slope of the car-velocity line in Figure 8.2 left (a) for t > 0.2 sec corresponds to the friction coefficient 0.92. This is larger than the average friction calculated from the stopping time. The slightly smaller friction obtained from the stopping time reflects the short initial time interval which is necessary to build up the braking torque.

In Figure 8.2 right results for the ABS control algorithm b are shown. Note that here it also takes about 2 sec to reduce the car velocity from v_0 = 27 m/s to v_1 = 10 m/s which gives the same effective friction as obtained using ABS control algorithm (a). The maximum in the μ-slip curve (see Figure 8.1) depends on the car velocity and is of order μ_{max} = 1.1 meaning that the ABS braking control algorithm used above could still be improved. Note also that the wheel tends to lock about 3 or 4 times per second. However, since the speed of the car is usually not known during ABS braking, braking control algorithms used in most cars today assume the braking torque only from the wheel rotation acceleration. This is possible because, as shown in Figure 8.2 right (a), as the wheels tend to lock, the rotational velocity very rapidly decreases, and hence the ABS controller decreases the braking torque.

Note that the (average) of the slip in Figure 8.2 left (b) and right increases with increasing time or, equivalently, decreasing car velocity. This is due to the fact that the time it takes for the wheel to lock, when the slip s > s*, decreases as v_c decreases. Thus, during the time period Δt between two changes of the brake torque, the maximal slip (corresponding to the minimum rolling velocity) will increase as v_c decreases. This is easy to show mathematically. Since the car velocity changes slowly compared to the rolling velocity, from the definition $s = (v_c - v_R)/v_c$ one get

$$\frac{dv_R}{dt} \approx -v_c \frac{ds}{dt} \qquad \text{(Equation 8.5)}$$

If approximating the μ-slip curve for s > s* with a straight line,

$$\mu_{eff} \approx \mu_0 - \Delta\mu\, s \qquad \text{(Equation 8.6)}$$

from Equation 8.4

$$I\frac{d^2\phi}{dt^2}=\frac{I}{R}\frac{dv_R}{dt}\approx-\frac{Iv_c}{R}\frac{ds}{dt}=MgR[\mu_0-\Delta\mu s]-M_B \qquad \text{(Equation 8.7)}$$

or

$$\frac{d_s}{dt}=-A+Bs \qquad \text{(Equation 8.8)}$$

where $A = (MgR\mu_0 - M_B)(R/Iv_c)$ and $B = \Delta\mu(MgR^2/Iv_c)$. Since A and B can be considered as constant during the time interval between the changes in the braking torque, one get

$$s(t)=\left(s(0)-\frac{A}{B}\right)e^{Bt}+\frac{A}{B} \qquad \text{(Equation 8.9)}$$

where

$$\frac{A}{B}=\frac{1}{\Delta\mu}\left(\mu_0-\frac{M_B}{MgR}\right) \qquad \text{(Equation 8.10)}$$

One can show that

$$s(0)-\frac{A}{B}=[s(0)-s^*]+\frac{M_B-M^*_B}{\Delta\mu MgR} \qquad \text{(Equation 8.11)}$$

where $M^*_B = Mg(\mu_0 - \Delta\mu s^*)$ is the braking torque necessary in order to stay at the maximum in the μ-slip curve. If $s(0) > s^*$ and the braking torque $M_B > M^*_B - \Delta\mu MgR[s(0) - s^*]$ one have $s(0) - A/B > 0$ and during the time interval Δt the slip will increase with $[s(0) - A/B]\exp(B\Delta t)$. Since $B\Delta t \sim 1/v_c$ the maximum slip will increase exponentially (until the wheel blocks, corresponding to s = 1) with the inverse of the car velocity. This behaviour (i.e., the increase in the slip with decreasing car velocity) can be seen in Figure 8.2 (b) and is even stronger for the second ABS control algorithm.

Figure 8.3 shows the μ-slip curve during stationary slip (green curve) and the instantaneous effective friction coefficient $\mu_{eff}(t) = F_x(t)/F_N$ during braking (red curve) for the car velocity $v_c = 27$ m/s.

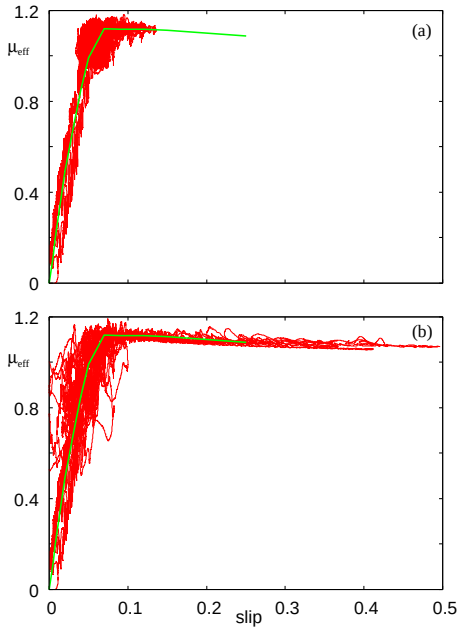

Figure 8.3: The μ-slip curves for ABS braking using algorithms a (top) and b (bottom)

The red and green curve in Figure 8.4 show the car velocity using the ABS control algorithms (a) and (b). The ABS control algorithm (a) is slightly more effective than algorithm (b), but algorithm (a) assumes that s* is known and remains constant during the braking event. The procedures a and b result in nearly the same time ≈ 2 sec.

In the calculations above for ABS algorithm (a) s* = 0.05 is used which, in fact, is not the maximum of the μ-slip curve which instead is at s* = 0.07 (see Figure 8.1). However, remarkable, the braking distance using s* = 0.07 in the present case is almost the same as for s* = 0.05, see Figure 8.4 (left). In Figure 8.4 (right) using algorithm a with s* = 0.05 and 0.07. Both cases result in nearly the same time for reducing the car velocity from 27 to 10 m/s. The effective friction μ ≈ 0.87 is smaller than the maximum kinetic friction which is ≈ 1.1.

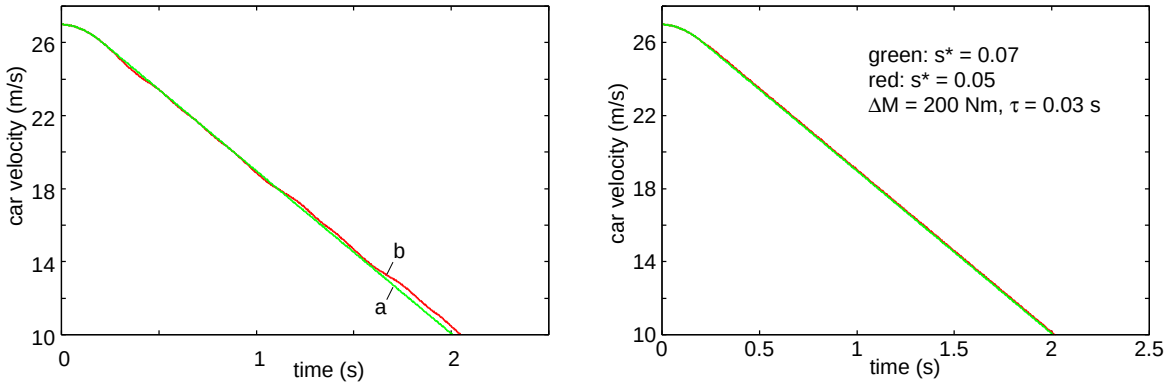

Figure 8.4: The car velocity v_c as a function of time t during ABS braking using two algorithms a (with s = 0.05) and b (left)*

The reason for this is that with the relative large magnitude of the brake moment change ΔM = 200 Nm and the relative low frequency of the brake moment changes (time interval τ = 0.03 sec) the algorithm (a) is not able to focus on a narrow region of slip around s* but in each case fluctuates over a similar range of slip values as shown in Figure 8.5 left where the blue curve is the steady-state μ-slip curve. In Figure 8.5 right, the relation between the slip and the effective friction coefficient for the case where ΔM is 100 Nm and τ = 0.015 sec is shown.

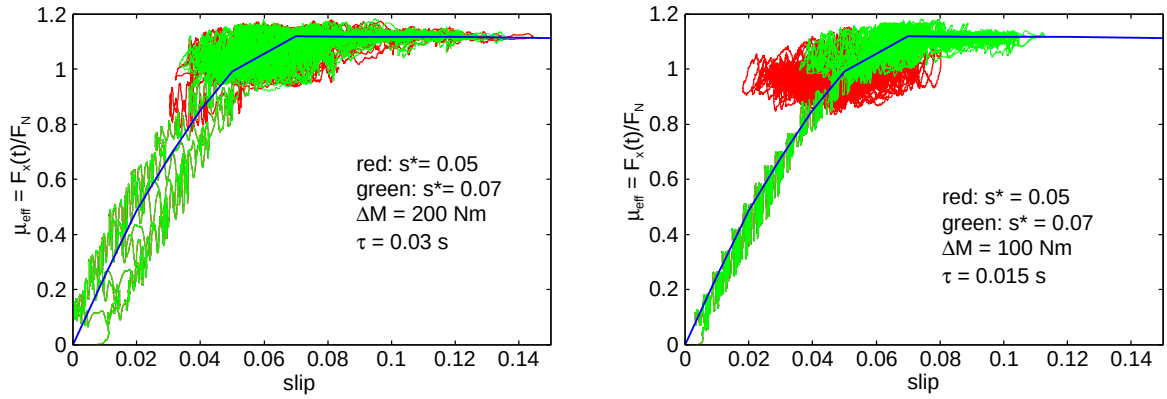

Figure 8.5: Dynamical μ-slip curves for ABS braking using two different chosen s-slip values for control algorithm a*

However, if ΔM is lowered to 100 Nm and double the rate at which the brake moment is modified (so that τ = 0.015 sec) then the algorithm (a) results in a more narrow distribution of slip centred around s*. This results in an increase in the braking distance for the case s* = 0.05 while the braking distance for s* = 0.07 is modified very little, see Figure 8.6.

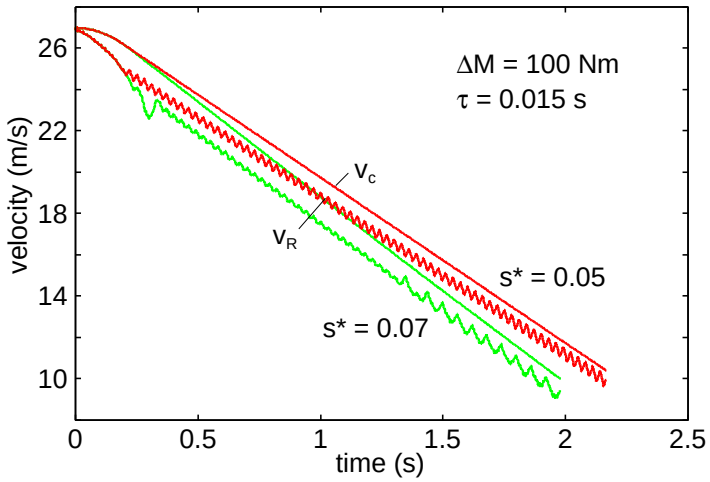

Figure 8.6: The car velocity v_c and the rolling velocity v_R as a function of time t for ABS braking with two different chosen s-slip values using algorithm a*

The ABS braking control algorithms used today usually assumes that only the wheel rolling velocity $v_R(t)$ is known. Basically, whenever a wheel tends to lock-up, which manifests itself in a large (negative) wheel angular acceleration, the braking torque is reduced. These ABS braking control algorithms (e.g. the Bosch algorithm) are rather complex and not public. However, the tyre model and the phenomenological rubber friction law can be applied to realistic ABS braking control algorithms and to more complex cases such as braking during load fluctuations (e.g. braking on uneven road surfaces) and switching between different road surfaces (by using different road surface power spectra during an ABS braking simulation).

Chapter NINE

This chapter summarises the research findings. The achievements are compared to the objectives defined in chapter one. The author's conclusions are presented and the contribution to the field's knowledge is outlined. Finally, areas for future research are addressed.

9. Conclusion and future work

9.1 Review of research objectives and achievements

The objectives presented in Chapter 1 of the research project and key achievements are described in the following:

Objective 1: To conduct a literature review of current research in the areas of rubber friction, tyres and automotive safety.

Achievement 1: A detailed survey of the relevant publications and state-of-the-art references associated with rubber friction and tyre research is presented in Chapter 3. Moreover, an in depth overview of automotive safety systems is given in Chapter 1.2. In this part, an enhanced focus is placed on current trends and likely future developments. In addition the historical development of vehicle brake systems development is presented in Chapter 2.1. Finally, Chapter 2.3 introduces the concept of predictive safety systems.

Objective 2: To identify potential novel automotive safety systems.

Achievement 2: Objective 1 showed, that state-of-the-art safety systems are started automatically even some time before a potential collision. The assumption of a tyre with low inflation pressure causes a higher friction resulted in the idea of a novel automotive safety system. To trigger the system equations to calculate moments of warnings and interventions of predictive safety systems are derived in Chapter 2.3. The concept of the novel automotive system is shown in Chapter 4. It is based on a double chamber rim. The second chamber, which is also called low pressure chamber, is designed below the base of the 'standard rim' and connected with the first chamber in case of a upcoming collision to increase the tyre contact patch.

Objective 3: To demonstrate the concept of a potential safety system application.

Achievement 3: To illustrate the technical realisation, a double chamber wheel is designed, presented in Chapter 4.3. The feasibility of the system is shown in Chapter 4.2, where the three main groups of the manufacturing process are introduced. All production methods can be applied to produce the novel double chamber rim. An electronic interface to the in-vehicle bus system is implemented by the author during the Master project 'The Development of a New Automotive Diagnostic Approach', which can be used to get the information of a distance sensor. A wireless connection to the rim is implemented using the ZigBee standard to trigger the actuator for linking both chambers, shown in Chapter 4.3.

Objective 4: To investigate the influence of internal tyre pressure on vehicles' braking distance of vehicles.

Achievement 4: Experiments are carried out using a state-of-the-art brake robot system designed by Anthony Best Ltd. The results are shown in Chapter 5.1. Additional braking test data are provided by Hankook Tyres presented in Chapter 5.2. Also an experiment is performed pulling a car with locked wheels using a winch described in Chapter 5.3. All experimental data show a negligible effect of the tyre inflation pressure on the braking distance or the pull force and therefore on the area of the contact patch.

Objective 5: To identify a theoretical approach for explaining the experimental results.

Achievement 5: A contact to Dr. Persson and Dr. Lorenz, Forschungszentrum Jülich is established to gain a deeper look into contact mechanics and rubber friction. Contact mechanics theories after Hertz, shown in Chapter 6.2, Greenwood-Williamson in Chapter 6.3 and Bush et al. in Chapter 6.4 are discussed. Chapter 6.5 describes the novel contact mechanics theory of Persson and the rubber friction theory presented in Chapter 6.5 till 6.7. These theories were used, inter alia, to explain the experimental data of Chapter 5.

Objective 6: To validate Persson's novel rubber friction law and tyre model by comparing them to experimental results.

Achievement 6: The novel contact mechanics theory and rubber friction theory of Persson, introduced in Chapter 6.5 till 6.7, is validated using experimental tyre data. The experimental data is provided by the ika of RWTH University Aachen. For the study, the viscoelastic modulus of the tyre rubber is measured using DMA, explained in Chapter 7.1. The surface roughness of sandpaper is characterised in Chapter 7.2. A novel 1D and 2D tyre model is introduced in Chapter 7.3 and 7.4 and the calculations are compared to experimental data.

9.2 Contribution to knowledge

Contribution 1: The concept of a novel safety systems is developed which can be used in different vehicles e.g. cars, buses or trucks. Therefore, a new tyre needs to be designed which is not changing the tyre stiffness, when the inflation pressure is changed or which develops a significant higher traction for a low inflation pressure. A detailed description of the tyre inflation pressure influence on the friction is shown in Chapter 7.4.3.

Contribution 2: The investigation of the influence of tyre inflation pressure on the stopping distance using a state-of-the-art brake robot system. A detailed description can be found in Chapter 5. As far as known this kind of experiment was not conducted previously.

Contribution 3: A novel friction law and tyre model is tested. Therefore, a study between theoretical predictions and experimental data is carried out. Good agreement between theory and experimental data is found, presented in Chapter 7.3 and 7.4. The 2D tyre model, which is including the phenomenological rubber friction law, can be used, e.g. for vehicle dynamic simulations. Therefore, calculations of ABS braking are performed, using two different algorithms, to investigate the influence of maximum slip on the braking distance, discussed in Chapter 8.

9.3 Conclusions

Conclusion 1: The literature review, presented in Chapter 3 shows a high potential for research in the areas of rubber friction and tyres. Also the end of the development of road safety systems is not finished yet. In order to achieve the target set by the European Commission to halve the number of road deaths in 2020 or the long term goal of an accident free traffic, advanced safety systems need to be developed, discussed in Chapter 1.

Conclusion 2: The feasibility of the novel safety system is possible as shown in Chapter 4, but a new tyre needs to be developed which has a higher friction potential for low inflation pressure. How big the effect in terms of emergency braking is needs to be evaluated in following projects.

Conclusion 3: Using a valve as actuator of the double chamber rim is not ideal, due to the restricted flow rate. An alternative option is the use of a blow out disc which is discussed in Chapter 4.

Conclusion 4: Experiments have shown, that the tyre inflation pressure has only little influence on the braking distance with state-of-the-art tyres. Using a brake robot system for this kind of measurement allows to perform tests in a repeatable way, shown in Chapter 5.

Conclusion 5: The experimental set-up of pulling a car with locked wheels to measure the friction is not the best way. The wheels of the car could not be locked during the whole experiment. Alternative test rigs are existing which is addressed in Chapter 5.

Conclusion 6: To measure the pressure distribution in the tyre contact area, two methods were used during this research. The first method uses a Fujitsu Prescale Film which is has low costs but with a limited resolution. The second method uses the sensor technology based on the change of capacity to visualize the pressure distribution. This method is much more advanced and gives more accurate results.

Conclusion 7: Comparing the novel rubber friction law and tyre model with experimental data gives good agreement, as shown in Chapter 7. However, sandpaper is not the best substrate for validating the theory due to the relative sharp roughness which causes a much stronger wear than on asphalt or concrete road surfaces.

9.4 Future work

Future work 1: Performing brake tests using the brake robot system and a vehicle fitted with run-flat tyres. The design of run-flat tyres has a different influence on the tyre stiffness. This can cause some influences on the braking distance at low tyre inflation pressure. Additional, the tyres should be fitted with a tyre pressure monitoring system (TPMS) to record the change of the inflation pressure during the experiments.

Future work 2: Building a prototype of the novel safety system which can be tested in vehicles to show the feasibility of realization. Therefore, four double chamber rims need to be produced and fitted with a blow out disc. The brake disc can be triggered using a wireless signal using e.g. the ZigBee standard. The moment of intervention can be deviated using the calculations presented in Chapter 2.3.3.

Future work 3: The potential of the novel safety system can be evaluated theoretically and experimentally using the friction properties of a new designed tyre for the described application, shown in Chapter 4. The computer code which is used in Chapter 7 can be applied for the theoretical investigation or other vehicle dynamic simulation programs.

Future work 4: To conduct a study for comparing the novel rubber friction theory and tyre model with experimental data using a trailer test rig. Furthermore, the results can be compared to the drum experiments, which were gained during the present investigations, to evaluate the differences between the two tyre characterisation test rigs.

Future work 5: To develop a novel test rig for the identification of the required input parameters for the tyre characterisation which are needed for the calculations using the new rubber theory and tyre model. The parameters for the code are:

- The viscoelastic modulus of the tyre rubber.
- The powerspectrum of the surface.
- The pressure distribution in the contact area at three different nominal loads.
- The lowest eigenfrequency in longitudinal and transverse direction.
- The tyre stiffness and damping.

A method to measure the pressure distribution in the contact area dynamically would also give better results. Current approaches do not show satisfying results and are at prototype status.

Future work 6: The algorithm of the ABS calculations, presented in Chapter 8 do not take the load transfer into account. Therefore, the code can be extended using the approach shown in Chapter 2.2. Also the 2D tyre model presented in Chapter 7.4, which is including the phenomenological rubber friction law shown in Chapter 6.5 till 6.7, can be applied to realistic ABS braking control algorithms.

Future work 7: To develop a user friendly environment for using the rubber friction law and tyre model. At the moment the code can be operated using the command line under Linux. To make the program more user friendly, it is possible to develop a graphical user interface (GUI). Another option is the implementation of the friction law and tyre model in a different environment, e.g. using Matlab.

Bibliography

[1] European Parliament, Regulation No 661/2009, “Concerning type-approval requirements for the general safety of motor vehicles, their trailers and systems, components and separate technical units intended therefor”, Brussels, 2009

[2] Persson, B.: “Rubber friction and tire dynamics”, Journal of Physics: Condensed Matter 23, 2011

[3] Seiffert, U. et al.: “Automotive Safety Handbook”, SAE International, 2nd Edition, 2007

[4] Wilfert, K.: “Entwicklungsmoeglichkeiten im Automobilbau”, ATZ, 1973

[5] Seiffert, U.: “Fahrzeugsicherheit Personenwagen” VDI-Verlag, Duesseldorf, 1992

[6] Schulenberg, P., Gonter, M.: “Active Safety by Driver Assistance Systems”, International Seminar on Automotive Electronics Technology”, SAE-China, 2009

[7] Koenig, M. et al.: “A Sensor System for Pre-Crash Deployment with extremely low False Alarm Rate”, 5th International Workshop on Intelligent Transportation (WIT), Hamburg, Germany, 2008

[8] Waldt, N. et al.: “Testing of Pre-Crash-Airbag-Systems with Extreme Low False Alarm Rate”, 9th International Airbag Symposium on Car Occupant Safety Systems, 2008

[9] Braess H., Seiffert U.: “Handbuch Kraftfahrzeugtechnik”, Ed. 6, Wiesbaden, 2011

[10] Statistisches Bundesamt Deutschland: “Verkehr, Verkehrsunfälle”, Fachserie 8, Reihe 7, 2013

[11] Statistia GmbH: “Entwicklung der Fahrleistung von PKW seit 1975”, 2013

[12] Bundesverband Güterkraftverkehr Logistik und Entsorgung e.V.: “Fahrleistungen”, 2013

[13] European Union: “European Road Safety Action Programme, Halving the number of road accident victims in the European Union by 2010”, 2003

[14] International Road Traffic and Accident Database: “Road Safety Annual Report 2013”

[15] Klanner, W.: “Status Report and Future Development of the Euro NCAP Programme”, 17 International Technical Conference on the Enhanced Safety of Vehicles, Amsterdam, 2001

[16] European Union: “Towards a European road safety area: policy orientations on road safety 2011-2020”, 2010

[17] Selig M.: “The Development of a New Automotive Diagnostic Approach”, Masterthesis University of Huddersfield, 2010

[18] Breuer B., Bill K.H.: “Bremsenhandbuch: Grundlagen, Komponenten, Systeme, Fahrdynamik”, Vieweg + Teubner Verlag, Wiesbaden, 2006

[19] Brown, I. D.: “Review of the ‚Looked-but-Failed- to-See‘ Accident Causation Factor”, Road Safety Research Report No. 60, Department for Transport, London, 2005

[20] Salmon, P. M., Regan, M. A., Johnston, I.: “Human Error and Road Transport: Phase One – A framework for an error tolerant road transport system”, Report Nr. 256, Monash University Accident Research Centre, Victoria, Australia, 2005

[21] NHTSA – Report, 2001

[22] Langwieder, K.: “Analyse des Bremsverhaltens bei Verkehrsunfällen“, Gesamtverband der deutschen Versicherungswirtschaft, 2001

[23] Bosch: “Analyse des Bremsverhaltens bei Unfällen auf Basis der GIDAS-Datenbank”, Internal Study, 2008

[24] Winner H. et al.: “Handbuch Fahrerassistenzsysteme”, Vieweg + Teubner, Wiesbaden, 2009

[25] Kopischke, S.: “Entwicklung einer Notbremsfunktion mit Rapid Prototyping Methoden”. Bericht aus dem Institut für Elektrische Messtechnik und Grundlagen der Elektrotechnik der Technischen Universität Braunschweig, Band 10. Aachen, Mainz., Diss. TU-Braunschweig, 2000

[26] Bender, E.: “Handlungen und Subjektivurteile von Kraftfahrzeugführern bei automatischen Brems- und Lenkeingriffen eines Unterstützungssystems zur Kollisionsvermeidung”, Dissertation TU Darmstadt, Stuttgart: Ergonomia-Verlag, 2008

[27] Convention on Road Traffic of 1968 and European Agreement Supplementing the Convention, UN, 1968

[28] Seeck, A.; Gasser, T. M.: “Klassifizierung und Würdigung der rechtlichen Rahmenbedingungen im Zusammenhang mit der Einführung moderner FAS”, Tagung Aktive Sicherheit durch Fahrerassistenzsysteme, München, 2006

[29] Weinberger, M.: “Der Einfluss von Adaptive Cruise Control Systemen auf das Fahrerverhalten”, Diss. Technische Universität München. Berichte aus der Ergonomie, Shaker-Verlag, Aachen, 2001

[30] Isermann, R., Schmitt, K., Mannale, R.: “Collision Avoidance Systems PRORETA: Situation Analysis and Intervention Control”, IFAC Symposium “Advances in Automotive Control”, München, 2010

[31] Knoll, P.M.: “Vorausschauende Sicherheitssysteme – die Schritte zur Unfallvermeidung“, VDA Technischer Kongress, Rüsselsheim, 2004

[32] Hoffmann; J.: “Das Darmstädter Verfahren (EVITA) zum Testen und Bewerten von Frontalkollisionsgegenmaßnahmen”, Dissertation TU Darmstadt, 2008

[33] Bachmann T.: “Literaturrechereche zum Reibwert zwischen Reifen und Fahrbahn”, VDI Verlag, 1996

[34] Amontons, M.: “Memoires de l'Académie Royale”, Paris, 1699

[35] Coulomb, C.A.: “Memoires de Mathematiques”, Physique de l'Académie des Sciences, No. 10, Paris, 1785

[36] Tomlinson, G.A.: Phil. Mag., 7, 1929

[37] Bowden, F. P., Hughes, T. P.: “The friction and lubrication of solids”, Oxford University Press, Oxford, 1950

[38] Kummer, H. W.: “Unified theory of rubber and tire friction”, Pennsylvania State University, Engineering Bulletin B-94, 1966

[39] Ludema, K. C., Gujrati, B. D.: “An analysis of the literature on tire road skid resistance”, ASTM special technical publication 541, 1973

[40] Moyer, R.A.: “Historical background of skid resistance measurement - American experience”, Proceedings of the First International Skid Prevention Conference, Virginia, 1958

[41] Brix: “Versuche über die Fahrsicherheit auf Teer und Asphaltstraßen”, Verkehrstechnik, 1928

[42] Schenk, R.: “Fahrbahnreibung und Schlüpfrigkeit der Straßen im Kraftwagenverkehr”, Berlin, Verlag Krayn, 1930

[43] Gölz, K.: “Straßendecke und Kraftwagen:Beziehungen zwischen Rauhigkeit und Reibung sowie Unebenheit und Stoßbeeinflussung”, Die Betonstraße, 07/1937

[44] Gölz, K.: “Straßenoberfläche und Kraftfahrzeug”, Habilitationsschrift, Mitteilung aus dem Straßenbauinstiut der TH Darmstadt, 1938

[45] Gölz, K.: “Straßendecke und Kraftwagen”, Mitteilung aus dem Straßenbauinstitut der TH Darmstadt, Die Betonstraße 1937 Heft 6/7

[46] Stinson, Roberts: “Coefficients of friction between tires and road surfaces”, Proceedings, Highway Research Board, Vol. 13, 1933

[47] Moyer, R. A.: “Skidding characteristics of road surfaces”, Proceedings Highway Research Board, Vol. 13, 1933

[48] Bird, J.; Scott, W.J. O.: “Studies in road friction I. Road surface resistance to skidding”

[49] Schindler: “Die statistische und dynamische Fahrbahnreibung und die Mittel zu deren Bestimmung”, ETH Zürich, Dissertation, 1936

[50] First International Skid Prevention Conference, Charlottesville, Virginia, 1959

[51] Second International Skid Prevention Conference, Columbus, Ohio, 1977

[52] Meyer, W.E., Walter, J. D.: “Frictional Interaction of Tire and Pavement Symposium”, Akron-Fairlawn, Ohio

[53] PIARC: International PIARC Experiment to Compare and Harmonize Texture and Skid Resistance Measurements, 1995

[54] Bowden, F. P., Tabor, D.: “The friction and lubrication of solids”, Oxford University Press, Oxford, 1950

[55] Kragelski, I.V., Dobcin, M.N.M Kambalov, V.S.: “Grundlagen der Berechnung von Reibung und Verschleiß”, München 1983

[56] Geyer W.: “Beitrag zur Gummireibung auf trockenen und insbesondere nassen Oberflächen”, Dissertation TU-München, 1971

[57] Clark S. K.: “Mechanics of Pneumatic Tires”, U.S Department of Transportation National Traffic Safety, Washington, 1981

[58] Fink, J.: “Beitrag zur Untersuchung des Kraftschlusses von Gummi auf vereisten Oberflächen”, Dissertation TU-München, 1982

[59] Moore, D.F.: “The friction and lubrication of elastomers”, Pergamon Press, Oxford, 1972

[60] Wiliams, M. L., Landel, R. F., Ferry, J. D.: “The Temperature Dependence of Relaxation Mechanisms in Amorphous Polymers and Other Glass-forming Liquids”, Journal of American Chemical Society 77, 1955

[61] Geyer W.: “Der Einfluß geometrischer Reibflächen-Rauhigkeitsformen auf das trockene und nasse Reibverhalten von Gummi”, Automobil-Industrie, 1972

[62] Gent A.N., Walter J.D.: “The Pneumatic Tire”, U.S. Department of Transportation, 2006

[63] The European Tyre and Rim Technical Organisation, “Standards Manual and Engineering Design Information”, Brussels, 2013

[64] European Parliament, Regulation No 1222/2009, “Labelling of tyres with respect to fuel efficiency and other essential parameters”, Brussels, 2009

[65] Gipser M.: “FTire”, www.cosin.eu

[66] Mäkinen, T & al.: “APOLLO Final Report including Technical Implementation Plan”, Tampere, Finland, 2005

[67] Clarke, D. et al.: “Fatal Vehicle-occupant Collisions: An In-depth Study”, Road Safety Research Report No. 75, Department for Transport, London, 2007

[68] Peussa, P. et al.: “FRICTION Final Report”, Tampere, Finland, 2009

[69] SAE J 175-2003: “Wheel Impact Test Procedures Road Vehicles”, 2003

[70] ISO 9227:2012: “Corrosion tests in artificial atmospheres. Salt spray tests”, 2012

[71] Schrötlin W.: “Das mechatronische Rad”, Final year project, Frankfurt UAS, Germany, 2011

[72] DIN 7817-1:1990-06: “Rims for motor vehicles and trailers; rims with flange J, JK and K without bead retaining contour”, 1990

[73] Data sheet of Axial miniature magnetic valve, BMT Fluid Control Solutions GmbH, Frankfurt, 2011

[74] Clapeyron, M. C.: “Mémoire sur la puissance motrice de la chaleur”, Journal de l'École polytechnique, 1834

[75] Balaban L., Simon A.: “Wireless actor/sensor network”, Project documentation, Frankfurt UAS, Germany, 2011

[76] IEEE Computer Society, IEEE Standard 802.15.4: “ Low-Rate Wireless Personal Area Networks (LR-WPANs)”, 2012

[77] ISO 7498-1:1994: “Information technology – Open Systems Interconnection – Basic Reference Model: The Basic Model”, 1994

[78] Atmel: “Datasheet ATmega128RFA1”, 2012

[79] Atmel: “Datasheet AT90CAN128”, 2008

[80] Anthony Best Dynamics Ltd: “In-vehicle products for vehicle testing, Detailed Catalogue”, Bradford on Avon

[81] iMAR GmbH: “Datasheet iTraceRT”, 2013

[82] GeneSys GmbH: “Datasheet ADMA-G: Automotive Dynamic Motion Analyzer”, 2013

[83] OXTS: “RT3000 User Manual”, Upper Heyford

[84] Fujifilm: “Datasheet Prescale Film”, Düsseldorf, 2007

[85] Intelligent Perception: “Pixcavator Software”, 2013

[86] Oh, Y., Kuk N.S.: “Private Communication”, Hankook Tire, Ltd

[87] ika, RWTH University Aachen: “Brochure Testing Facilities”, 2013

[88] ISO 7500-1:2004: “Metallic materials – Verification of static uniaxial testing machines – Part 1: Tension/compression testing machines – Verification and calibration of the force-measuring system, 2004

[89] JCGM 100:2008: “Evaluation of measurement data – Guide to the expression of uncertainty in measurement”, 2008

[90] Marshek K.M. et al.: “Performance of Anti-Lock Braking System Equipped Passenger Vehicles – Part III: Braking as a Function of Tire Inflation Pressure”, SAE, 2002

[91] Hertz H. R.: “Über die Berührung fester elastischer Körper”, Journal für die reine angewandte Mathematik, 1882

[92] Bush A. W., Gibson R.D., Thomas T.R.: “The elastic contact of a rough surface”, Wear, 1975

[93] Lorenz B.: “Contact Mechanics and Friction of Elastic Solids on Hard and Rough Substrates”, Dissertation RWTH University Aachen, 2012

[94] Johnson K. L., Kendall K., Roberts A.D.: “Surface energy and contact of elastic solids”, Proceedings of the Royal Society, London, 1971

[95] Greenwood J. A., Williamson J.B.P.: “Contact of nominally flat surfaces”, Proceedings of the Royal Society, London, 1966

[96] Fuller K.N.G., Tabor D.: ”Effect of surface-roughness on adhesion of elastic solids”, Proceedings of the Royal Society, London, 1975

[97] Carbone G., Mangialardi L.: “Asperity contact theories: Do they predict linearity between contact area and load?” Journal of Mechanics and Physics of Solids, 2008

[98] Persson B.N.J.: “Theory of rubber friction and contact mechanics”, Journal of Chemical Physics, 2001

[99] Persson B.N.J.: “Adhesion between an elastic body and a randomly rough hard surface”, The European Physical Journal, 2002

[100] Persson B.N.J.: “Elastoplastic contact between randomly rough surface”, Physical Review Letters, 2001

[101] Persson B.N.J., Bucher F., Chiaia B.: "Elastic contact between randomly rough surfaces: Comparison of theory with numerical results", Physical Review B, 2002

[102] Persson B.N.J.: “Sliding Friction: Physical Principles and Applications”, 2nd ed., Springer Verlag, Heidelberg, 2000

[103] Grosch K.A.: “The Relation between the Friction and Visco-Elastic Properties of Rubber”, Proceedings of the Royal Society, 1963

[104] Heinrich G., Klüppel M., Vilgis T.A.: “Evaluation of self-affine surfaces and their implication for frictional dynamics as illustrated with a Rouse material”, Computational and Theoretical Polymer Science, 2000

[105] Klüppel M., Heinrich G.: “Rubber Friction on Self-Affine Road Tracks”, Rubber Chemistry and Technology, 2000

[106] Westermann S., Petry F., Boes R., Thielen G.: “Experimental Investigations Into the Predictive Capabilities of Current Physical Rubber Friction Theories”, Kautschuk Gummi Kunststoffe, 2004

[107] Persson B.N.J., Volokitin A.I.: “Rubber friction on smooth surfaces”, European Physical Journal, 2006

[108] Carbone G., Lorenz B., Persson B.N.J., Wohlers A.: “Contact mechanics and rubber friction for randomly rough surfaces with anisotropic statistical properties”, European Physical Journal, 2009

[109] Persson B.N.J.: “On the theory of rubber friction”, Surface Science, 1998

[110] Le Gal A., Yang X., Klüppel M.: “Evaluation of sliding friction and contact mechanics of elastomers based on dynamic-mechanical analysis”, The Journal of Chemical Physics, 2005

[111] Persson B.N.J.: “Theory of powdery rubber wear”, Journal of Physics, 2009

[112] Mofidi M., Prakash B., Persson B.N.J., Albohr O.: “Rubber friction on (apparently) smooth lubricated surfaces”, Journal of Physics, 2008

[113] Persson B.N.J., Albohr O., Tartaglino U., Volokitin A.I., Tosatti E.: “On the nature of surface roughness with application to contact mechanics, sealing, rubber friction and adhesion”, Journal of Physics, 2005

[114] Persson B.N.J., Albohr O., Creton C., Peveri V.: “Contact area between a viscoelastic solid and a hard, randomly rough, substrate”, The Journal of Chemistry Physics, 2004

[115] Persson B.N.J.: “Rubber friction: role of the flash temperature”, Journal of Physics, 2006

[116] Pacejka H.B.: “Tyre and Vehicle Dynamics”, 2nd ed., Elsevier, Amsterdam, 2006

[117] Persson B.N.J.: “Contact mechanics for randomly rough surfaces”, Surface Science Reports, 2006

[118] Heinrich G., Klüppel M.: “Rubber friction, tread deformation and tire traction”, Wear, 2008

[119] Rodriguez N.V., Masen M.A., Schipper D-J: “Tribologically modified surfaces on elastomeric materials”, Journal of Engineering Tribology, 2012

[120] Kuhlmann U., Albohr O.: “Private Communication”, Pirelli & C. SpA

[121] Lorenz B., Persson B.N.J., Fortunato G., Giustiniano M., Baldoni F.: “Rubber friction for tire tread compound on road surfaces ”, Journal of Physics, 2013

[122] Taylor Hobson: “Datasheet Form Talysurf-120L”, 1984

[123] Carl Zeiss AG:”Product Information Axiotech 100 HD”, 2013

[124] Press W.H., Teukolsky S.A., Vetterling W.T., Flannery B.P.: “Numerical Recipes”, 2nd ed., Cambridge University Press, 1992

List of figures

List of tables

List of publications

M. Selig, Z. Shi, A. Ball and K. Schmidt: “A Novel Diagnostic Approach for Automotive Systems Condition Monitoring”, 12th International Workshop on Research and Education in Mechatronics

M. Selig, A. Ball, J. Ash and K. Schmidt: “The influence of tyre contact patch on the stopping distance of automotive vehicles”, Journal of Physics: Conference Series, Volume 363

M. Selig, B. Lorenz, D. Henrichmöller, K. Schmidt, A. Ball and B.N.J. Persson: “Rubber friction and tire dynamics: A comparison of theory with experimental data”, Journal of Tire Science and Technology, to be published

List of supervised final year projects at Frankfurt UAS

Uljanow I.: “Fahrzeugfunktionen auf einem Mikrocontroller” (Vehicle Functions on Microcontroller Systems), Intedis GmbH & Co. KG, February 2012

Ahmed S.: “Erstellen einer Elektrische/Elektronische Architektur mit Continental Steuergeräten im Bereich des “Affordable Car” Projekts” (Development of a Electric/Electornic architecture with Continental Control Units for the “Affordable Car” Project), Continental AG, February 2012

Sfeir H.: “Entwicklung einer Mikrocontroller-gestützten Datenerfassung zur Steuerung eines Vector CANalyzer Systems” (Development of microcontroller based data acquisition system to control the Vector CANalyze), Continental AG, April 2012

Prill A.: “Development of an automated machine vision system for infotainment head unit tests”, Hyundai Motor Company AG, July 2012

Winter R.: “Synchronisation eines Schrittmotors durch Vier-Quadranten-Nullpunkterkennung mit Hilfe eines Software-Algorithmus auf einem 16bit Mikrocontroller” (Synchronisation of a step motor via four quadrant zero point detection using a software algorithm on a 16bit microcontroller), Continental AG, August 2012

Böhmer F.: “Objektorientierte Analyse und Entwurf einer flexiblen Prüfstandsapplikation in der Automobilindustrie” (Object Oriented Analyses and Design of a Flexible Test Bench Application in the Automotive Industry), Continental AG, April 2013

Nüvemann C.A.: “Entwicklung einer Testumgebung für Motorsteuergeräte mit Controlled Solenoid Injection – Einspritztechnolgie unter Verwendung von Hardware In The Loop Simulatoren” (Development of a Test Environment for Engine Control Units with Controlled Solenoid Injection using a Hardware In The Loop simulator), Continental AG, June 2013

Balban L.: “Einfluss von Fahrzeugparametern in Bezug auf fehlerbedingte ESP-Eingriffe” (Influence of vehicle parameter in terms of ESP-operation due to an error) , Continental AG, August 2013

La Blunda L.: “Entwicklung einer Innovativen Testumgebung zur Kommunikation über Bussysteme anhand von Graphical User Interfaces” (Development of an Innovative Test Environment for the Communication to In-Vehicle Bus Systems using Graphical User Interfaces), Continental AG, September 2013

Poungon S.: “Die Erstellung einer Parametriersoftware und die Erweiterung der Firmware für einen universellen CAN-RS232 Klimakammer Protokollumsetzer” (The development of a parametrization software and extension of firmware for a universal CAN-RS232 climatic chamber gateway), imc Test & Measurement GmbH, December 2013

Glossary of abbreviations

ABS	Anti-lock Braking System
ACC	Active Cruise Control
ADAS	Advanced Driver Assistance Systems
ADC	Automatic Distance Control
AFM	Atomic Force Microscope
BA	Brake Assist
BD	Braking Deceleration
CAD	Computer-aided design
CAN	Controller Area Network
DAC	Digital to Analogue Converter
DMA	Dynamic Mechanical Analysis
DOT	Department of Transportation
EBD	Electronic Brake Force Distribution
ECU	Electronic Control Unit
EHB	Electro Hydraulic Brake
ESC	Electronic Stability Control
ETRTO	European Tyre and Rim Technical Organisation
ETTC	Enhanced Time To Collision
FEM	Finite Element Analysis
HMI	Human Machine Interface

PIARC	Permanent International Association of Road Congress
SEM	Scanning Electron Microscopy
SPI	Serial Peripheral Interface Bus
SRB	Speed Reduction Braking
SRM	Stuttgarter Reibungsmesser
TCS	Traction Control System
TPMS	Tyre pressure monitoring system
TTC	Time Temperature Shifted
UAS	University of Applied Sciences
UNECE	United Nations Economic Commission for Europe
WLF	Williams, Landel and Ferry

Glossary of notations

a_{obs}	Acceleration of obstacle
a_T	Shifting factor
A	Area of contact
A_0	Nominal contact area
A_{MC}	Master cylinder area
A_{WC}	Wheel cylinder area
b	Relative repeatability error
C	Internal ratio; Measured stiffness
C_C	Calculated stiffness
C(q)	Surface roughness power spectrum
d	Distance; Seperation
$d_B(v_{diff})$	Braking distance
d_{warn}	Warning distance
D_{max}	Maximum deceleration
D_{sub}	Delay subtracted
D_{req}	Required deceleration
D_{obs}	Deceleration of obstacle
E	Elastic modulus
$\underline{E}$	Complex modulus of elasticity
E'	Dynamic modulus

E''	Modulus of loss
f	Frictional force
f(ζ)	Diffusion constant
F_{aero}	Aerodynamic down and up force
F_A	Adhesion force
F_B	Braking force
F_{BB}	Braking force back
F_{BF}	Braking force front
F_{delay}	Delay due to aerodynamic resistance and friction
F_{driver}	Force by driver foot on the brake pedal
F_f	Tyre road friction
F_H	Hysteresis force
F_i	Force indicated by the force indicator of the testing machine
F_N	Normal force
F_{max}	Highest value of F
F_{min}	Lowest value of F
F_{rim}	Force acting on the rim
g	Gravitation
$\underline{G}$	Complex modulus of shearing
G'	Dynamic shear modulus
G''	Modulus of shear loss
h	Height

H	Hurst exponent
h(x)	Height profile
h*	Root-mean-square amplitude
h_{rms}	Root-mean-square roughness amplitude
i	Pedal ratio
I	Wheel inertia moment
$i_ä$	External ratio
k	Elasticity, Coverage factor
l	Length
L	Lateral size
m	Vehicle mass, Mass of tread block
M	Mass load
M_B	Braking torque
M_{rim}	Torque acting on the rim
n	Amount of gas substances
n_0	Number of asperities per unit area
N	Number of asperities in contact per unit area
p	Hydraulic pressure; Gas pressure
P_h	Surface height probability distribution
P(σ, ζ)	Stress distribution in contact area
q	Relative accuracy error, Surface roughness wavevector
Q	Ratio of tyre body side wall width

q_L	Smallest possible wavevector
q_0	Long distance roll-off wavevector
q_1	Short distance cut-off wavevector
r	Effective friction radius
r_{dyn}	Dynamic wheel radius
R	Dynamic tyre rolling radius; Gas constant; radius
s	Absolute position; Slip; Distance; Penetration
s*	Optimum slip
$s_B(v_{xv},0)$	Stopping position
tanδ	Dissipation factor
t_{tB}	Time threshold brake
t_{tC}	Time to collision
$t_{tC}(D_{rel})$	Enhanced time to collision
t_{tS}	Time to stop
T_s	Reference temperature
u_n	Relevant standard uncertainties
u_c	Combined uncertainty
U	Expanded uncertainty
v	Poisson ratios
V	Volume
v_c	Car velocity
v_{diff}	Differential velocity

v_{obs}	Velocity of obstacle
v_R	Rolling velocity
v_{rel}	Relative velocity
v_{sub}	Velocity subtracted
v_t	Circumferential speed
v_x	Absolute velocity
$v_{xv,0}$	Initial velocity
V	Brake booster support
$\ddot{x}$	Deceleration
μ	Coefficient of friction
η	Efficiency; proportionality constant
τ_B	Loss of braking time
τ_R	Driver reaction time
ω	Angular velocity, Complex frequency
τ	Shear stress
$\dot{\gamma}$	Shear rate
ε	Deformation
σ	Stress
ζ	Magnification
λ	Lateral resolution
δ	Phase difference
γ	Damping

Appendix A: Design drawing of double chamber rim

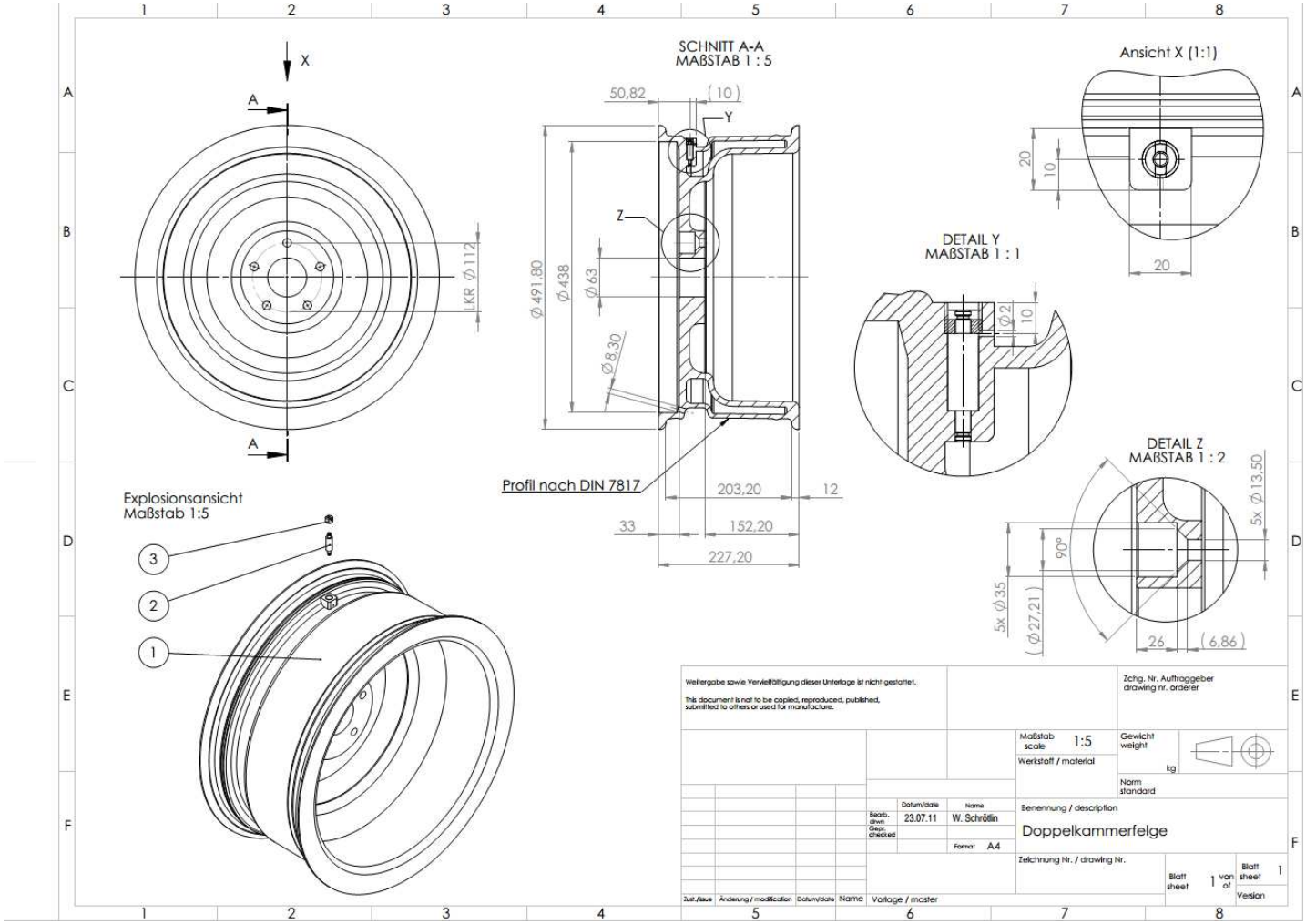

Appendix B: Brake robot composition for experiment

User interface PC

Controller

Power Supply

Appendix C: Brake test results

1.0 bar

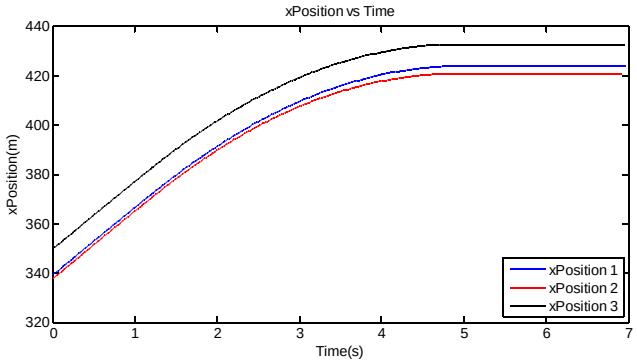

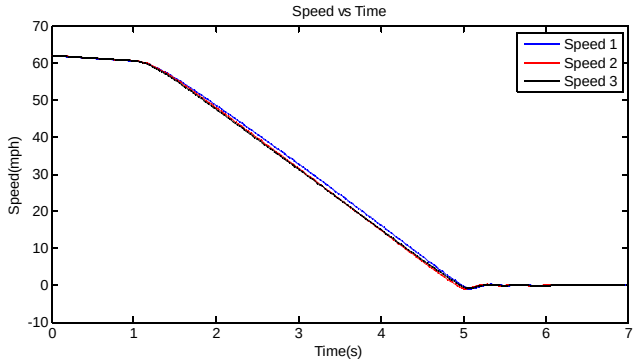

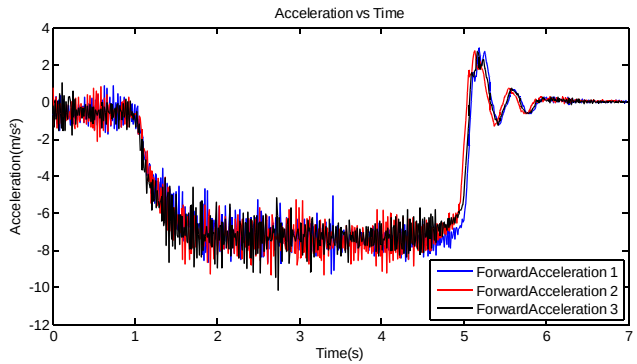

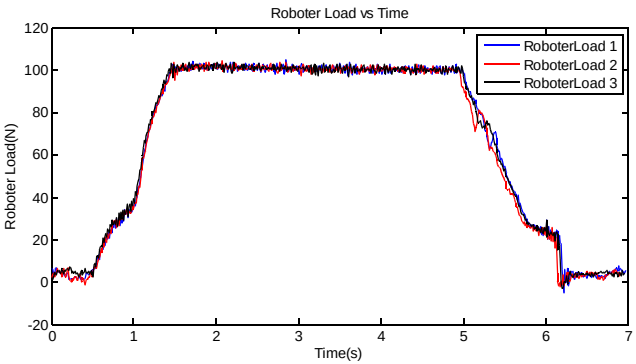

1.2 bar

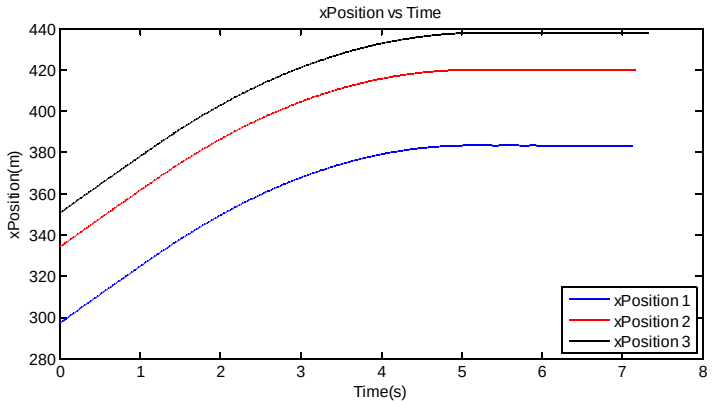
xPosition vs Time
xPosition(m)
Time(s)
xPosition 1
xPosition 2
xPosition 3

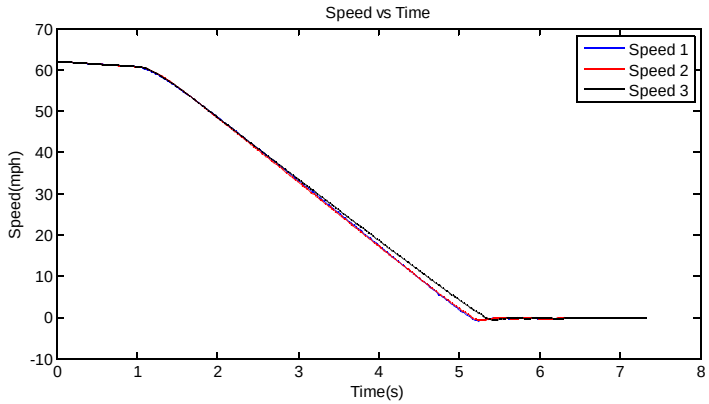
Speed vs Time
Speed(mph)
Time(s)
Speed 1
Speed 2
Speed 3

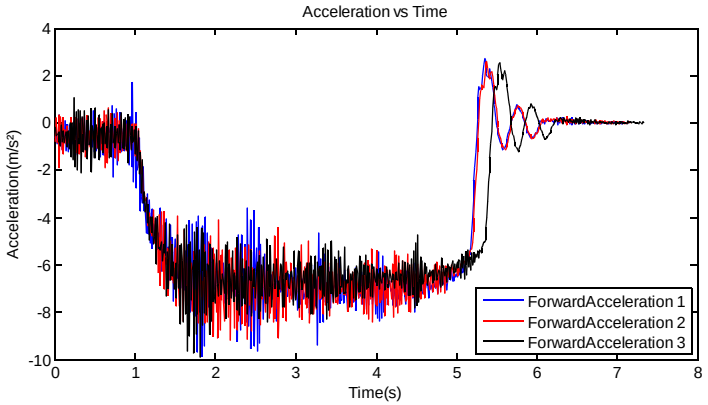
Acceleration vs Time
Acceleration(m/s²)
Time(s)
ForwardAcceleration 1
ForwardAcceleration 2
ForwardAcceleration 3

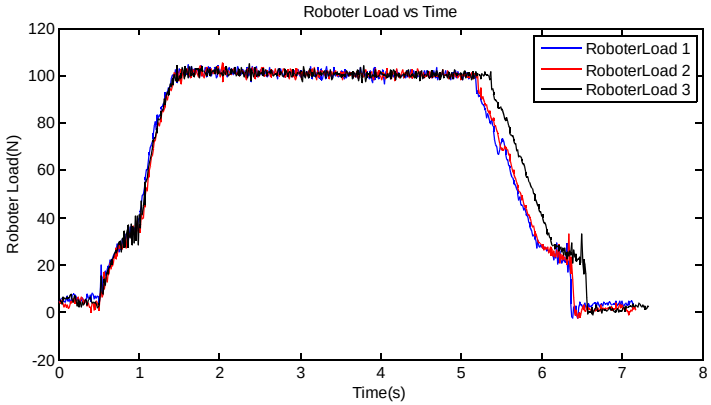
Roboter Load vs Time
Roboter Load(N)
Time(s)
RoboterLoad 1
RoboterLoad 2
RoboterLoad 3

1.4bar

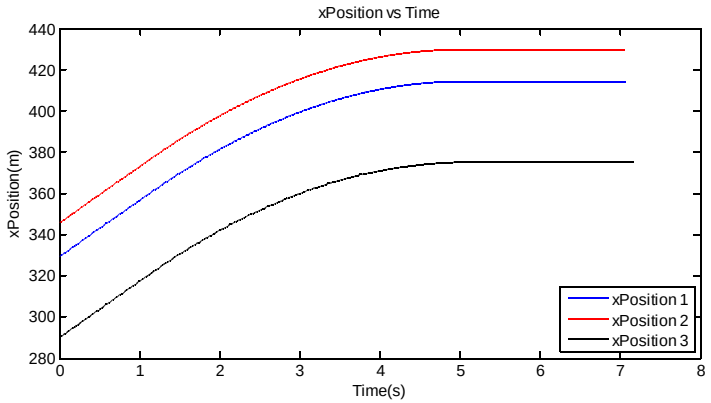
xPosition vs Time
xPosition(m)
Time(s)
xPosition 1
xPosition 2
xPosition 3

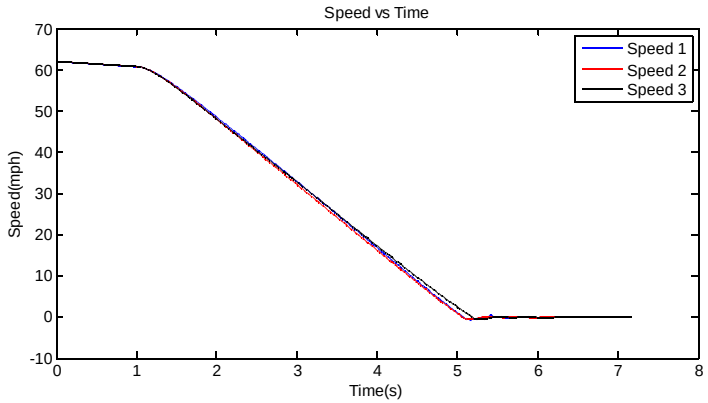
Speed vs Time
Speed(mph)
Time(s)
Speed 1
Speed 2
Speed 3

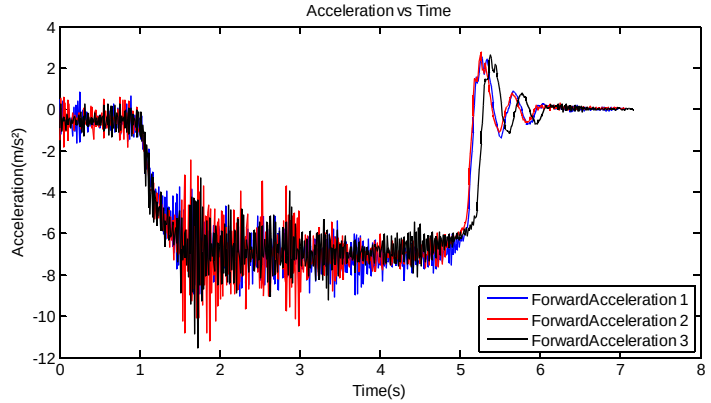
Acceleration vs Time
Acceleration(m/s²)
Time(s)
ForwardAcceleration 1
ForwardAcceleration 2
ForwardAcceleration 3

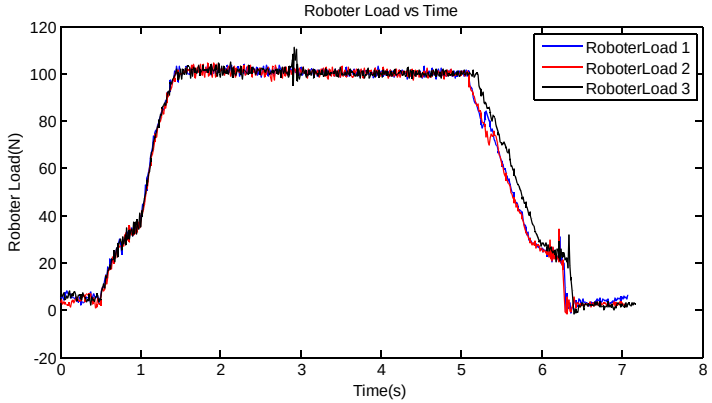
Roboter Load vs Time
Roboter Load(N)
Time(s)
RoboterLoad 1
RoboterLoad 2
RoboterLoad 3

1.6 bar

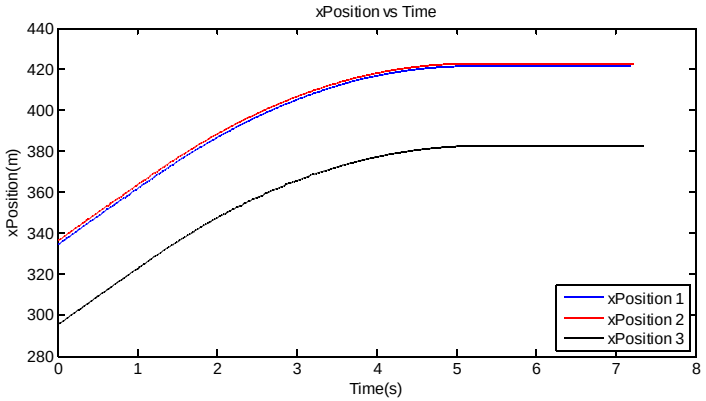
xPosition vs Time
xPosition(m)
Time(s)
xPosition 1
xPosition 2
xPosition 3

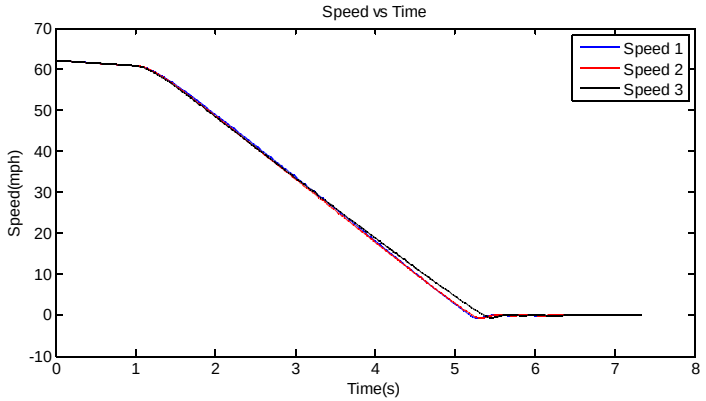
Speed vs Time
Speed(mph)
Time(s)
Speed 1
Speed 2
Speed 3

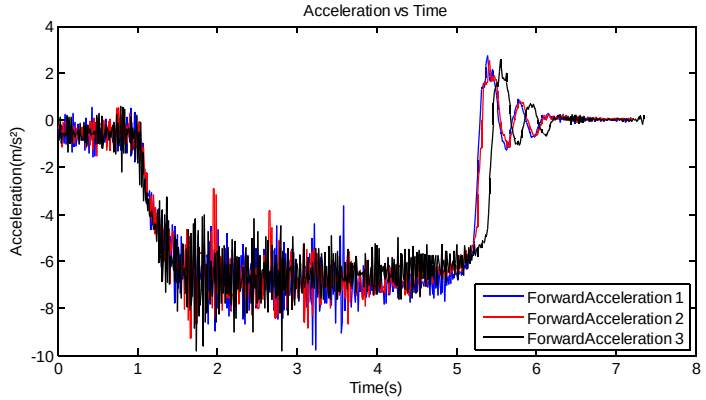
Acceleration vs Time
Acceleration(m/s²)
Time(s)
ForwardAcceleration 1
ForwardAcceleration 2
ForwardAcceleration 3

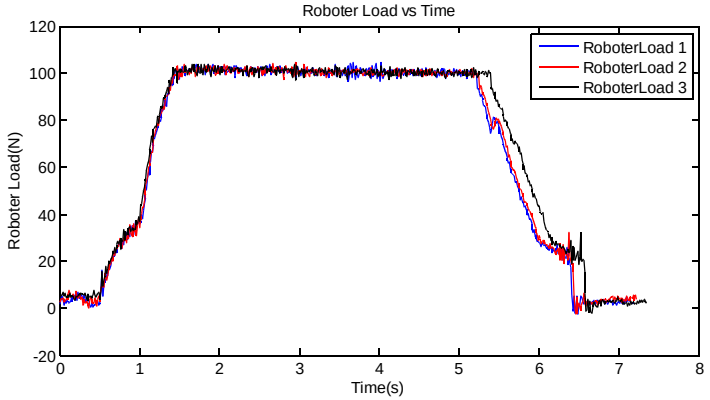
Roboter Load vs Time
Roboter Load(N)
Time(s)
RoboterLoad 1
RoboterLoad 2
RoboterLoad 3

1.8 bar

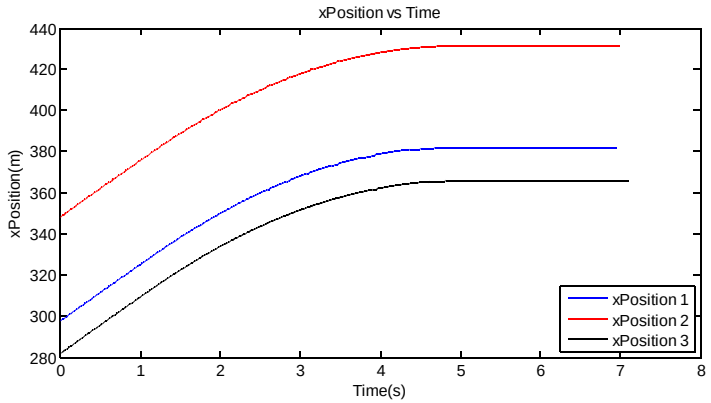
xPosition vs Time
xPosition(m)
Time(s)
xPosition 1
xPosition 2
xPosition 3

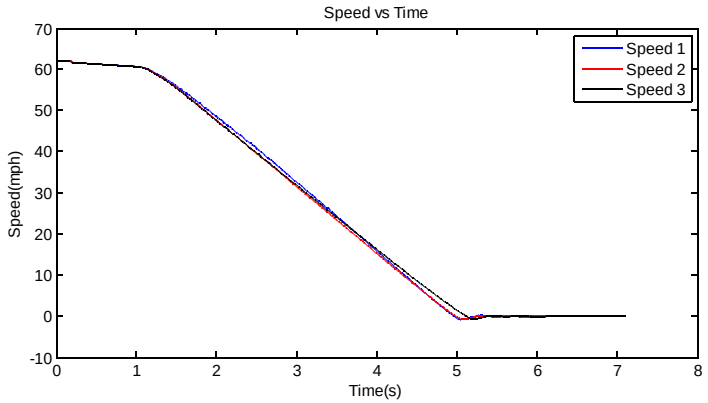
Speed vs Time
Speed(mph)
Time(s)
Speed 1
Speed 2
Speed 3

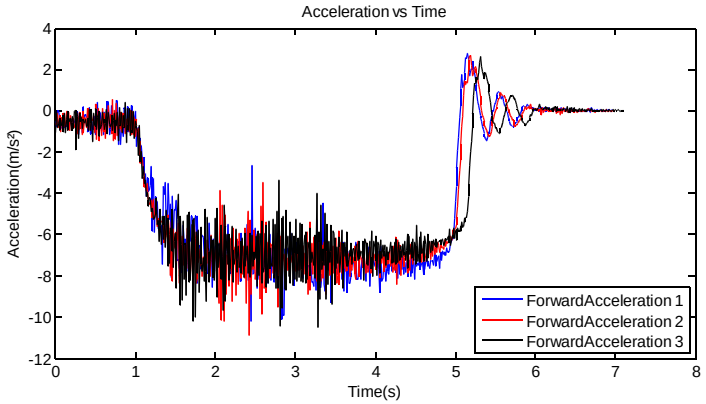
Acceleration vs Time
Acceleration(m/s²)
Time(s)
ForwardAcceleration 1
ForwardAcceleration 2
ForwardAcceleration 3

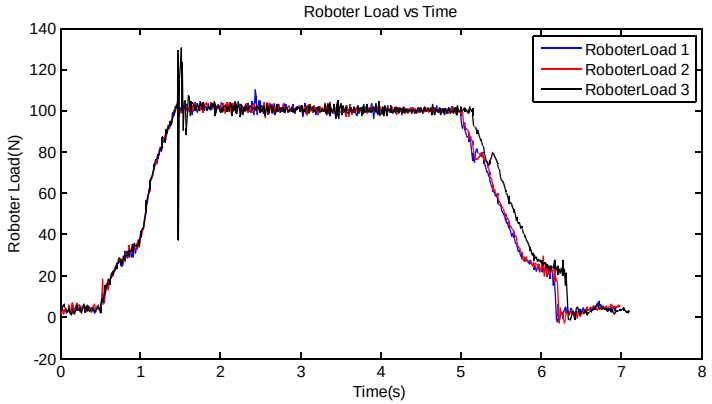
Roboter Load vs Time
Roboter Load(N)
Time(s)
RoboterLoad 1
RoboterLoad 2
RoboterLoad 3

2.0 bar

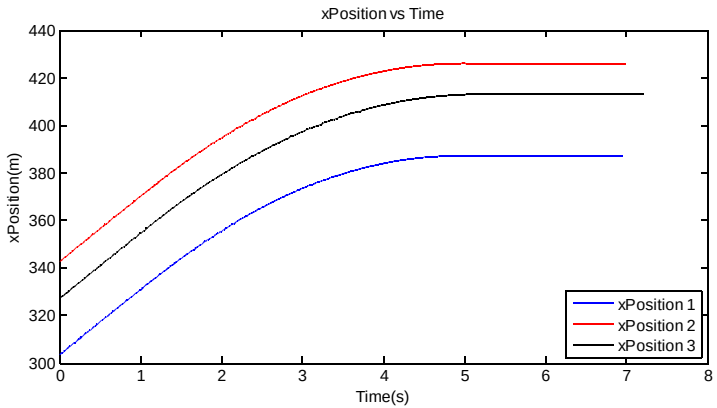
xPosition vs Time
xPosition(m)
Time(s)
xPosition 1
xPosition 2
xPosition 3

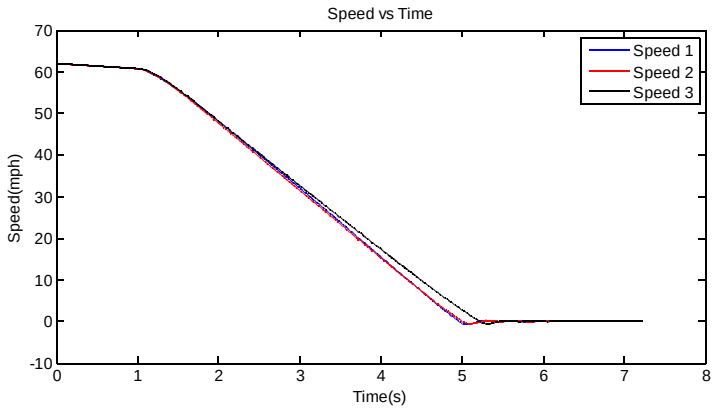
Speed vs Time
Speed(mph)
Time(s)
Speed 1
Speed 2
Speed 3

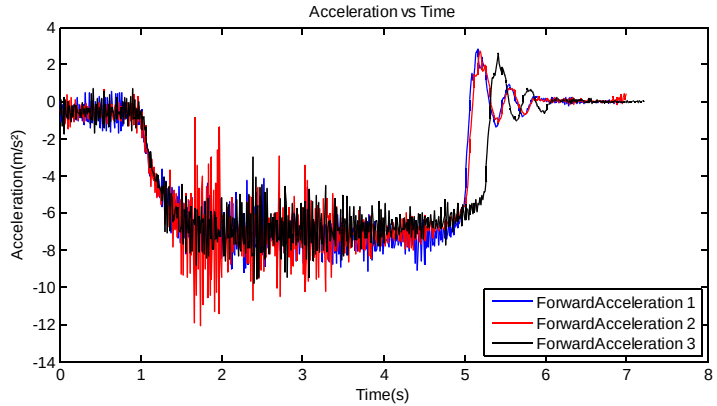
Acceleration vs Time
Acceleration(m/s²)
Time(s)
ForwardAcceleration 1
ForwardAcceleration 2
ForwardAcceleration 3

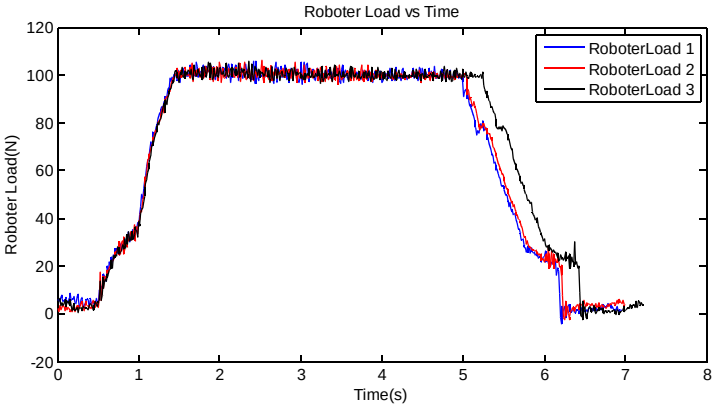
Roboter Load vs Time
Roboter Load(N)
Time(s)
RoboterLoad 1
RoboterLoad 2
RoboterLoad 3

2.2 bar

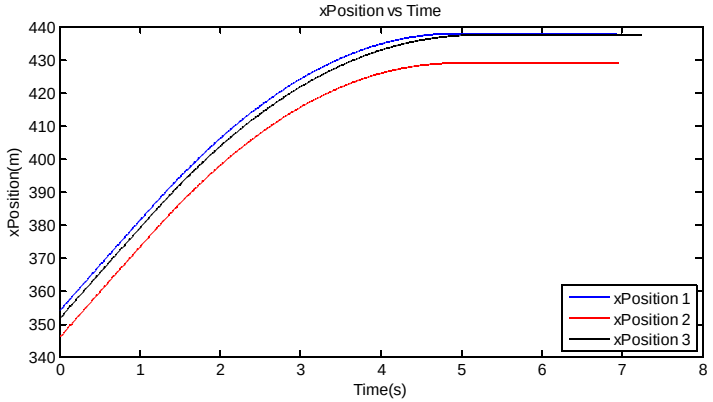
xPosition vs Time
xPosition(m)
Time(s)
xPosition 1
xPosition 2
xPosition 3

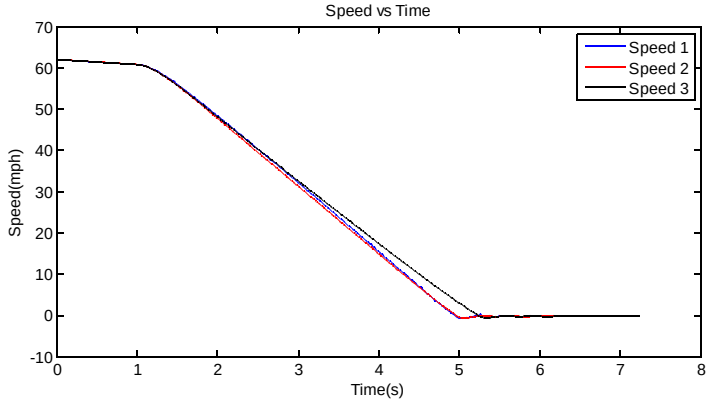
Speed vs Time
Speed(mph)
Time(s)
Speed 1
Speed 2
Speed 3

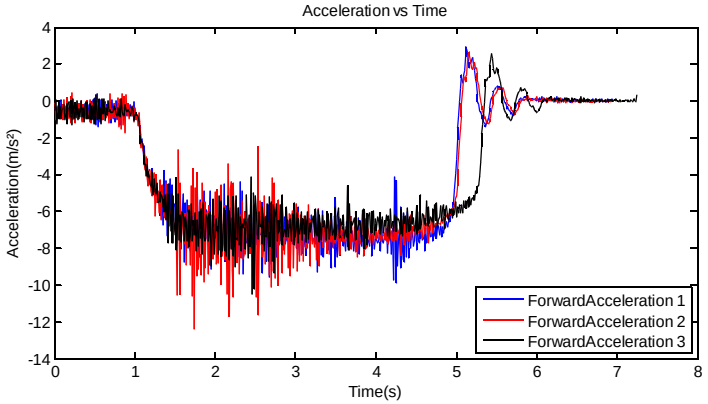
Acceleration vs Time
Acceleration(m/s²)
Time(s)
ForwardAcceleration 1
ForwardAcceleration 2
ForwardAcceleration 3

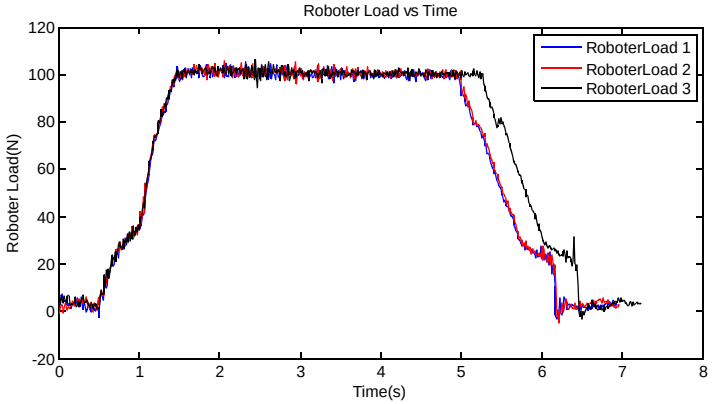
Roboter Load vs Time
Roboter Load(N)
Time(s)
RoboterLoad 1
RoboterLoad 2
RoboterLoad 3

2.4 bar

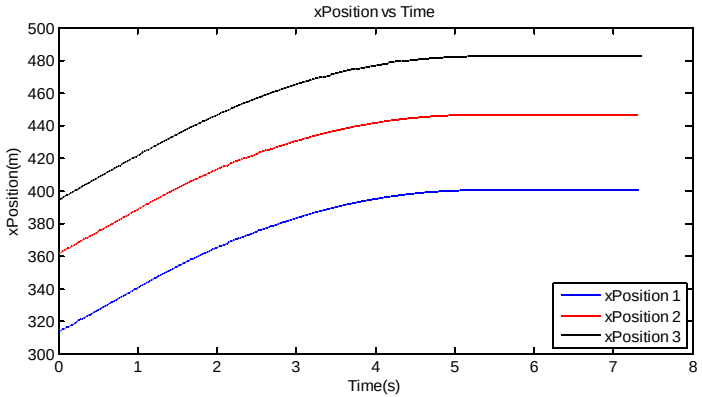
xPosition vs Time
xPosition(m)
Time(s)
xPosition 1
xPosition 2
xPosition 3

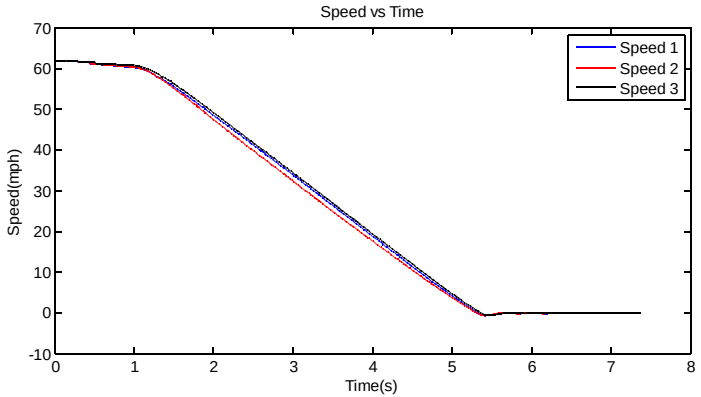
Speed vs Time
Speed(mph)
Time(s)
Speed 1
Speed 2
Speed 3

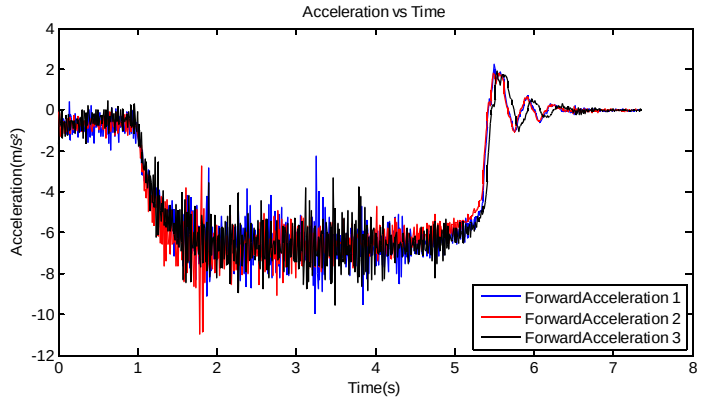
Acceleration vs Time
Acceleration(m/s²)
Time(s)
ForwardAcceleration 1
ForwardAcceleration 2
ForwardAcceleration 3

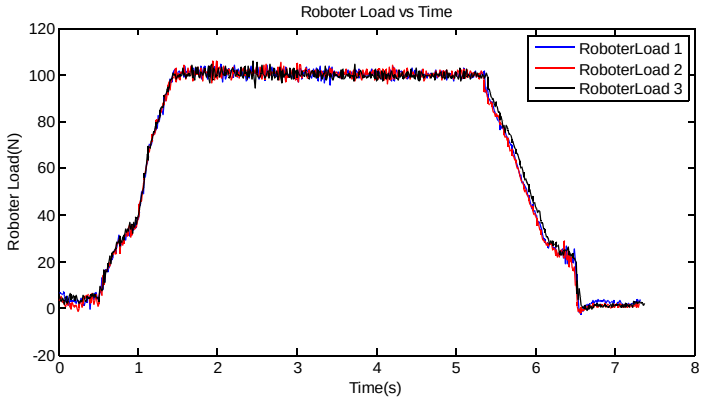
Roboter Load vs Time
Roboter Load(N)
Time(s)
RoboterLoad 1
RoboterLoad 2
RoboterLoad 3

ABS triggered 1.2 bar

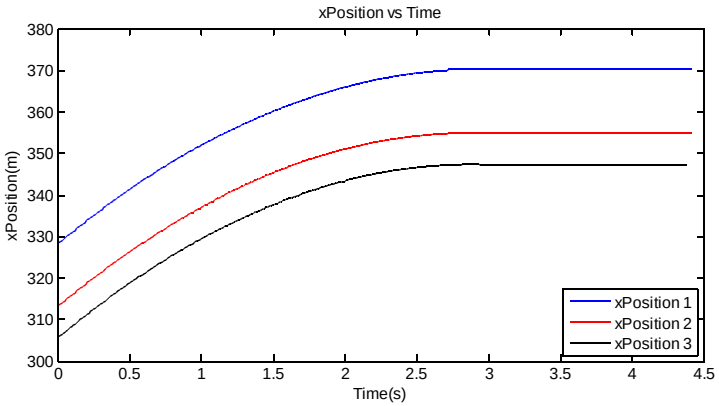

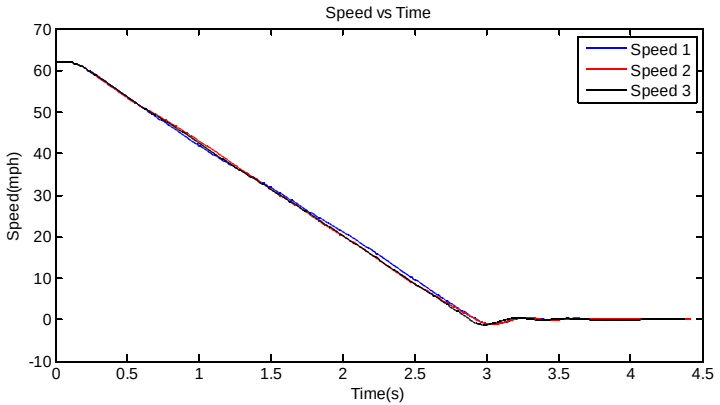

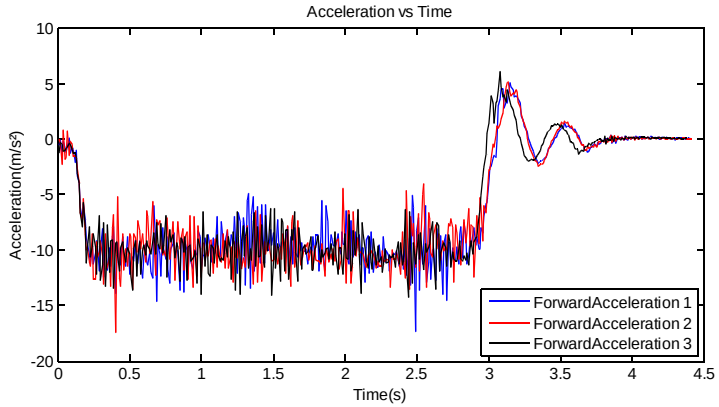

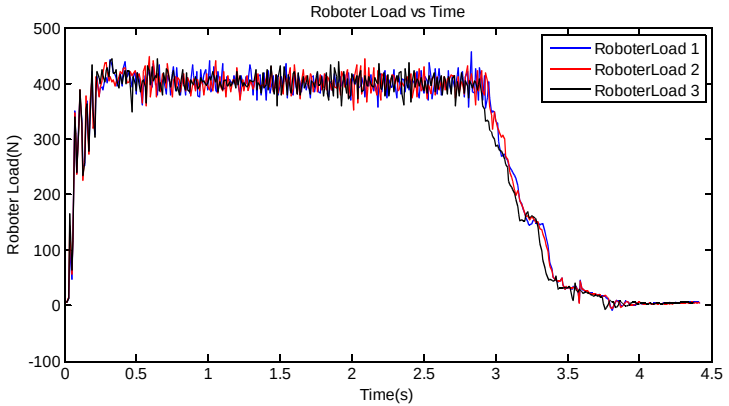

ABS triggered 1.6 bar

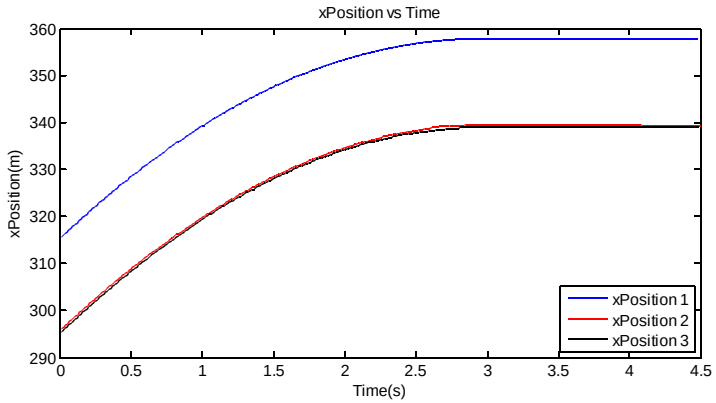

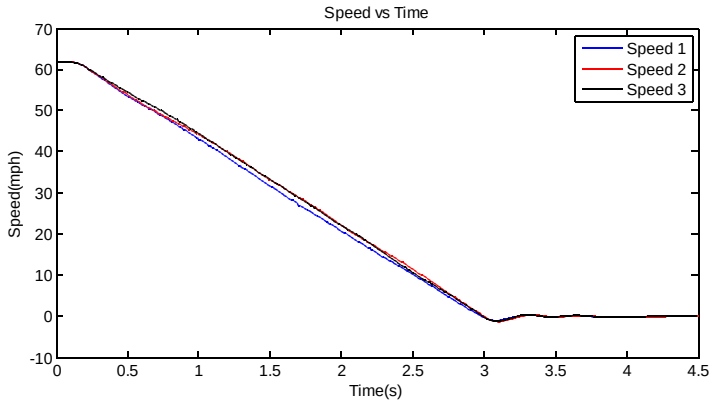

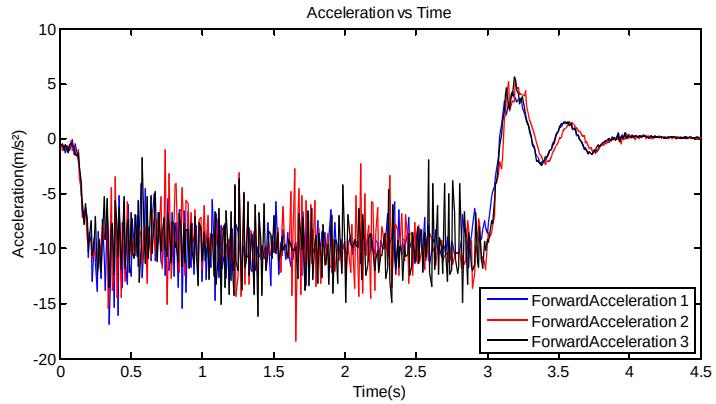

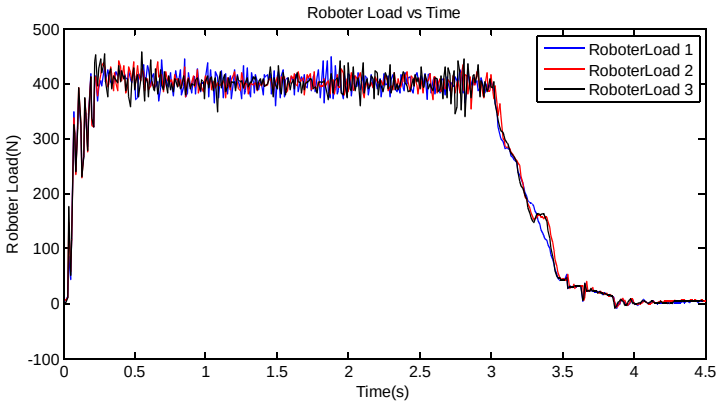

ABS triggered 2.4 bar

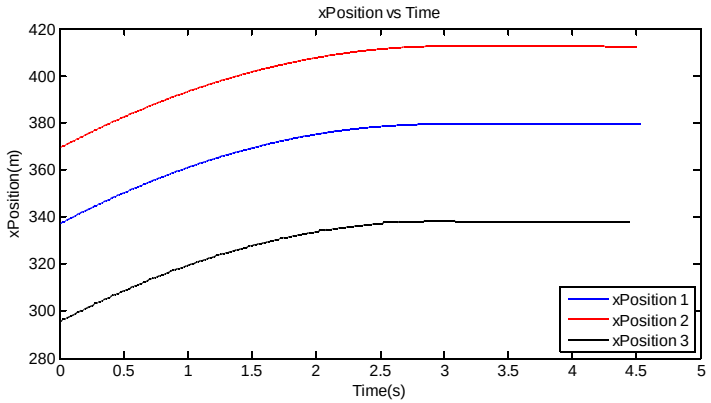

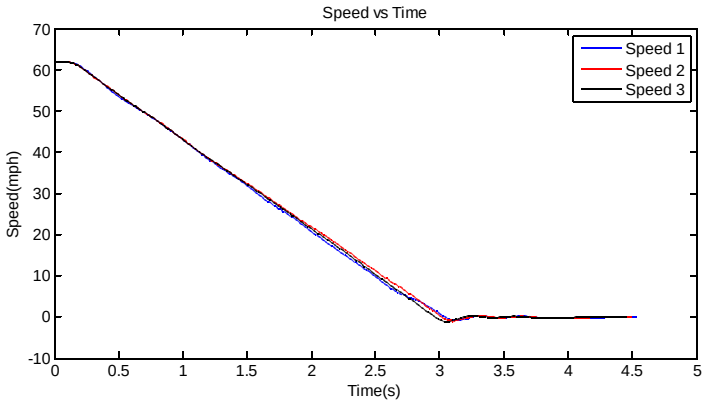

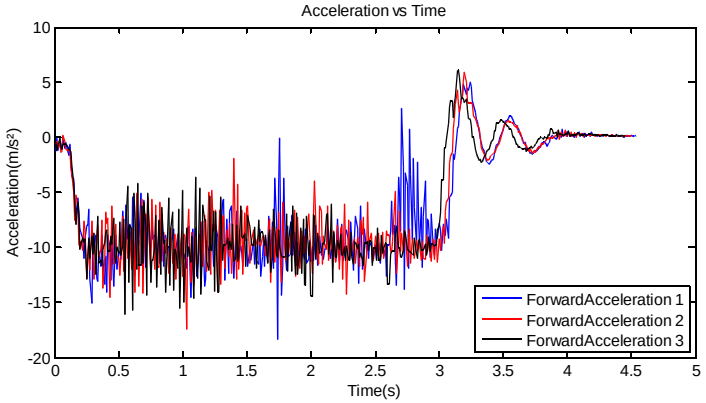

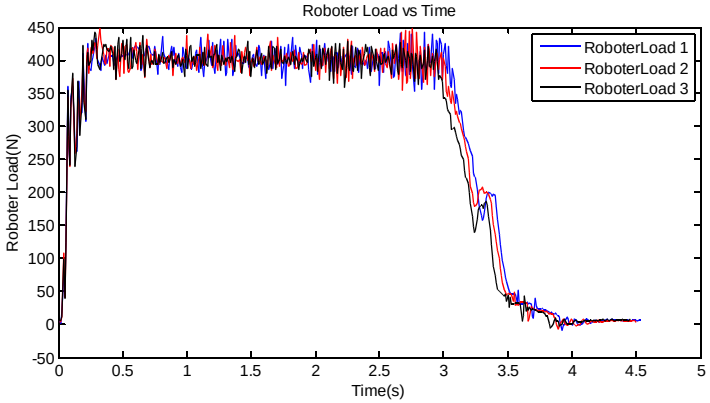

Appendix D: Pull experiment composition

Appendix E: Pull experiment results

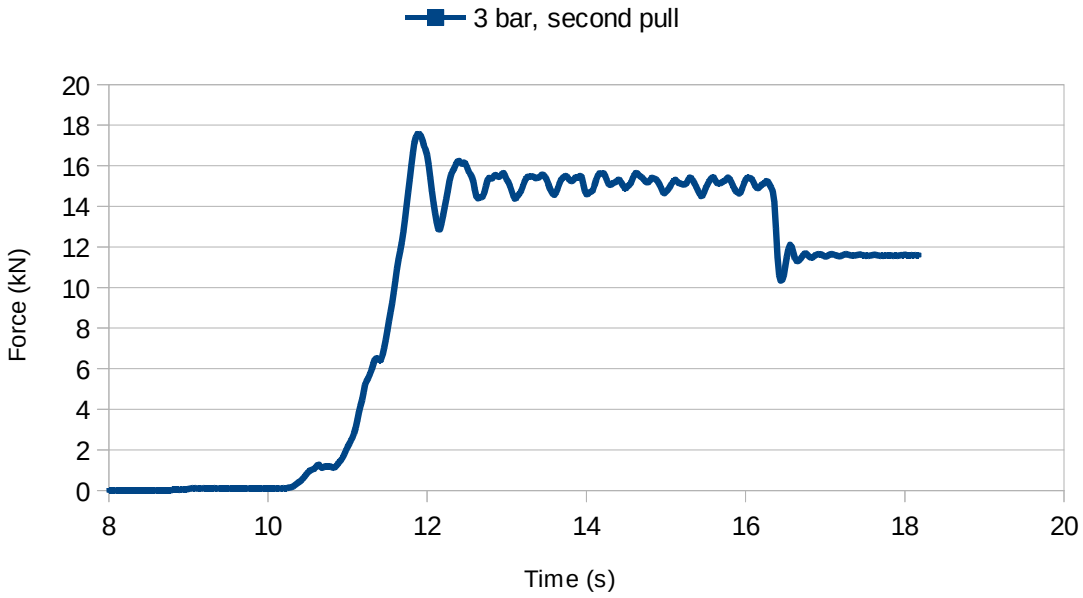

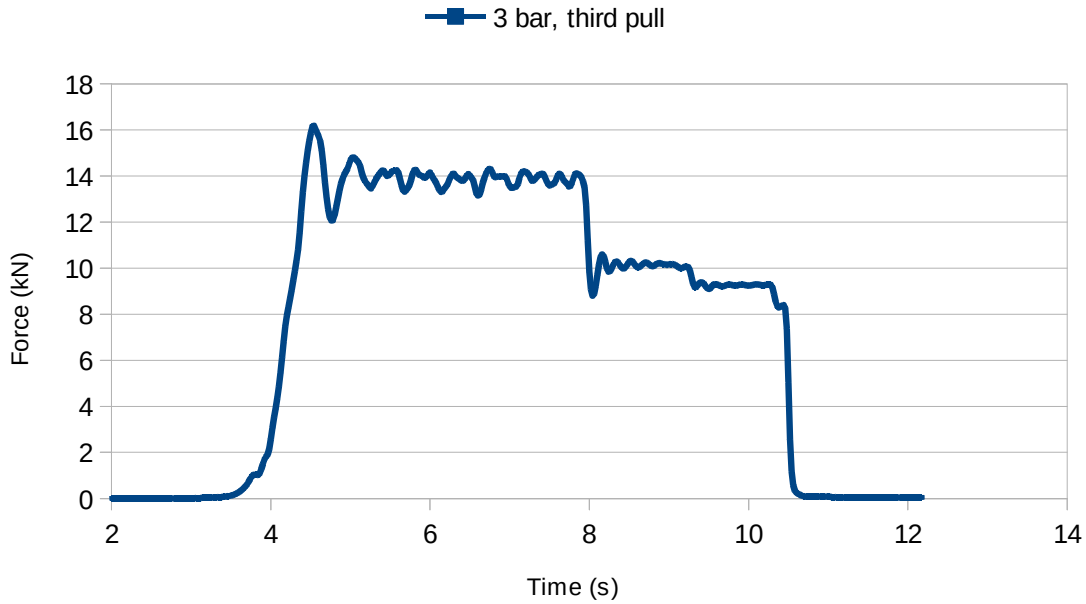

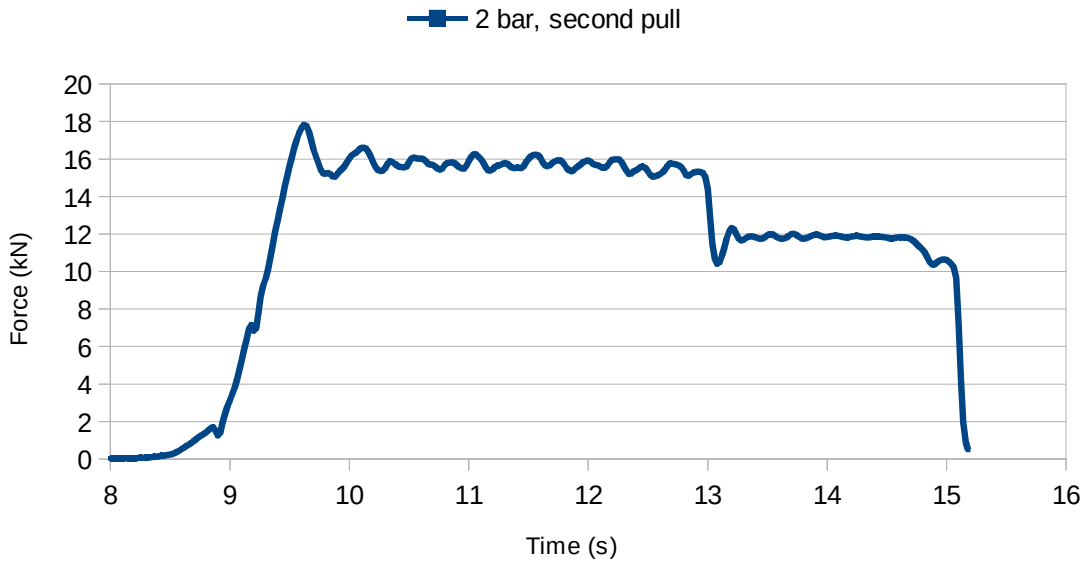
2 bar, second pull
Force (kN)
20
18
16
14
12
10
8
6
4
2
0
8
9
10
11
12
13
14
15
16
Time (s)

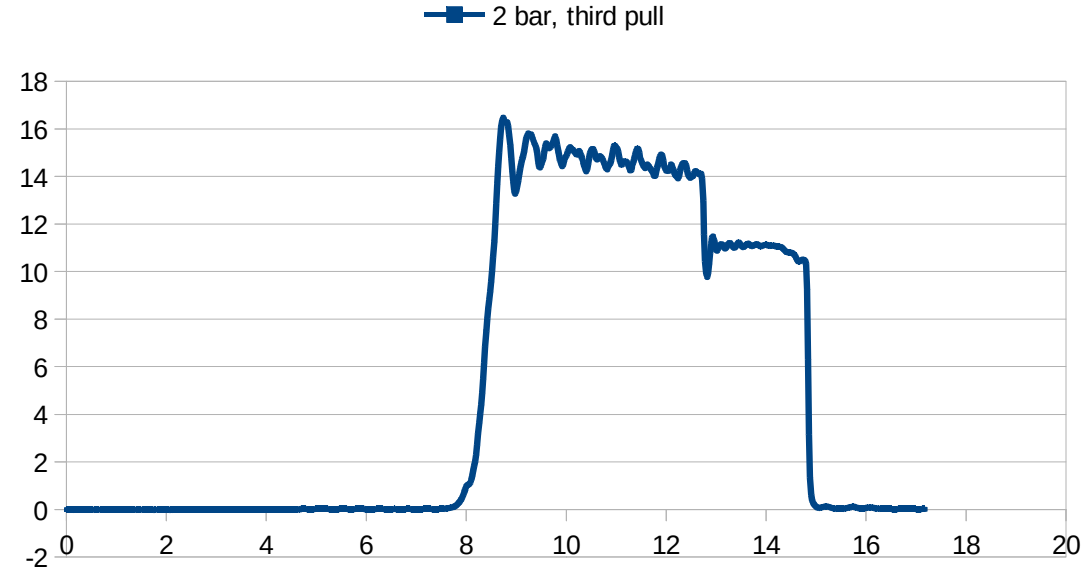
2 bar, third pull
18
16
14
12
10
8
6
4
2
0
-2
0
2
4
6
8
10
12
14
16
18
20

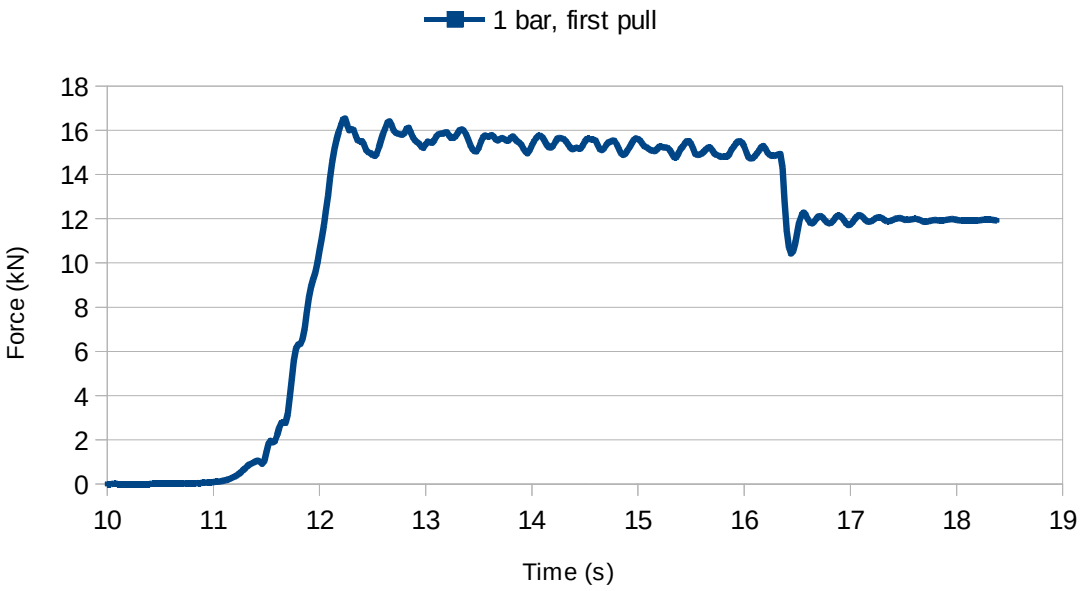
1 bar, first pull
Force (kN)
18
16
14
12
10
8
6
4
2
0
10
11
12
13
14
15
16
17
18
19
Time (s)

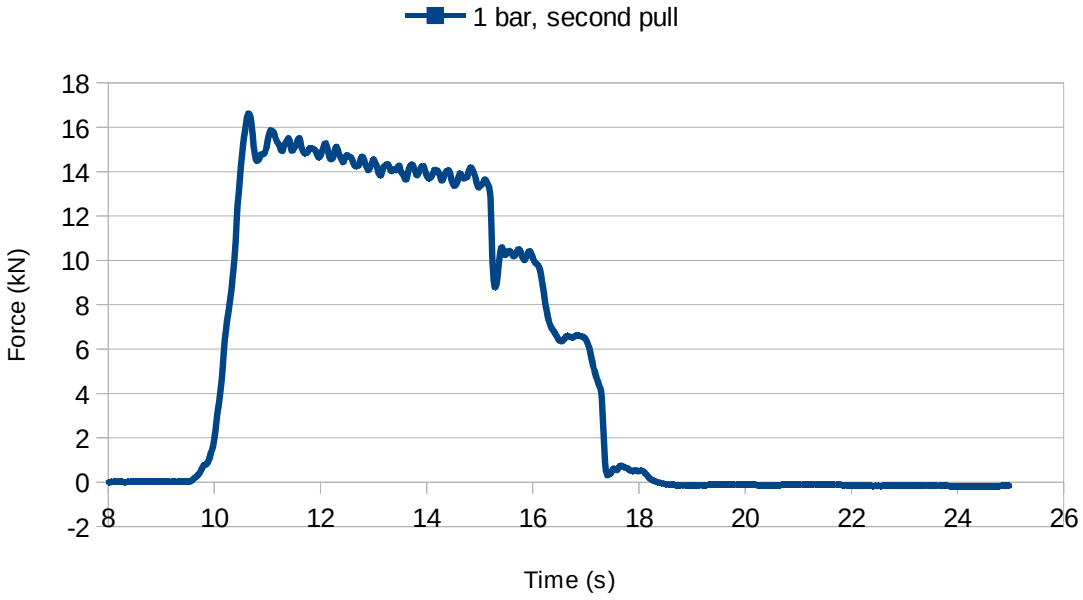
1 bar, second pull
Force (kN)
18
16
14
12
10
8
6
4
2
0
-2
8
10
12
14
16
18
20
22
24
26
Time (s)

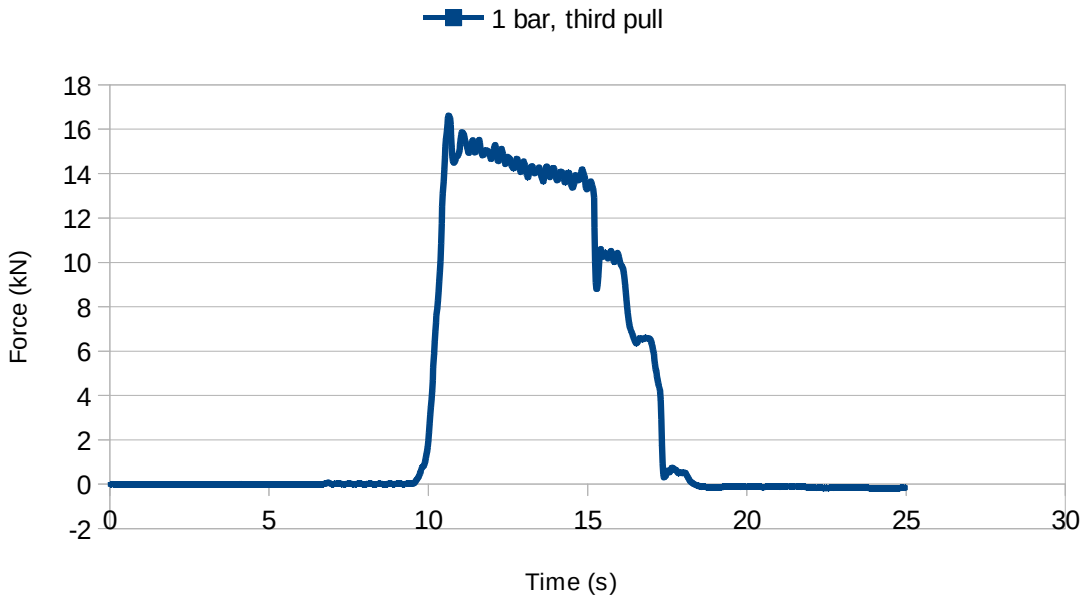
1 bar, third pull
Force (kN)
18
16
14
12
10
8
6
4
2
0
-2
0
5
10
15
20
25
30
Time (s)

Appendix F: Tyre footprint measurement

Appendix G: Q800 Dynamic mechanical analysis